University College London

Scanning Probe and Spectroscopy Studies of Rutile TiO_2(110)

Thesis submitted for the degree of Doctor of Philosophy by

Chi Ming Yim

Supervised by

Prof. Geoff Thornton

University College London

Department of Chemistry

February 2012

Declaration

I, Chi-Ming Yim, confirm that the work presented in this thesis is my own. Where information has been derived from other sources, I confirm that this has been indicated in the thesis.

Chi Ming Yim

February 2012

To my family, for everything...

"Politics is for the present, but an equation is for eternity."

— Albert Einstein

Abstract

In this thesis, surface science techniques were employed to study the chemistry of rutile TiO_2(110).

Scanning tunnelling microscopy (STM) and ultraviolet photoemission spectroscopy (UPS) have been used to determine the origin of the band-gap state in rutile TiO_2(110). By employing electron bombardment to vary the O_b-vac density while monitoring the band-gap state with UPS, we demonstrate that O_b-vac make dominant contribution to the photoemission peak and that is magnitude is directly proportional to the O_b-vac density.

CO adsorption on the Pd/TiO_2(110) surface was investigated with synchrotron radiation spectroscopies and STM. The Pd islands, which were grown by physical vapour deposition (PVD) of Pd onto the TiO_2(110) substrate at ∼800 K, had a pseudo-hexagonal shape and were not encapsulated with Ti^{n+} (n<4) species from the substrate. In addition, it was found that CO molecules bond vertically and form various ordered overlayers on the Pd(111) islands.

O_2 adsorption on the cross-linked TiO_2(110)-(1×2) surface was investigated with XPS, UPS and STM. The introduction of a small amount of O_2 leads to a drastic reduction in the number of the Ti^{3+} species at the topmost surface layers and the band-gap state intensity, as well as a noticeable rise in the surface workfunction. In STM, O_2 and its related molecules were found to preferably adsorb at the centre of the (1×2) strands.

Current imaging tunnelling spectroscopy (CITS) was also performed on the same surface at 78 K. It was found that the densities of the two occupied states, one at -0.7 V and and another at -1.3 V, vary between different features on the surface. Moreover, whilst having less-populated occupied states, the cross-links possess an empty state at 1.2 V which cannot be detected anywhere else. This work will be compared with theoretical calculations to elucidate the geometric structure of the cross-link TiO_2(110)-(1×2) surface.

Acknowledgements

Firstly, I would like to thank my supervisor Prof. Geoff Thornton and my second supervisor, Dr. Wendy Brown. I was very fortunate to have such wise and enthusiastic supervisors without whom my PhD study could never have been accomplished.

Secondly, I would like to thank Dr. Chi L. Pang and Dr. Greg Cabailh, for their instruction on the use of the UHV equipment. Special credit is given to Dr. Chi L Pang for his inspiring guidance on experimental design and academic writing.

I also want to thank Dr. Qiao Chen and Dr. Christopher Muryn for their invaluable advice on the technical problems that I have encountered during my PhD study.

I would also like to thank Mr. David S Humphrey, Mr. Jai Matharu and Mr. David Grinter in my group for their peer-support whenever I was frustrated with my work.

Special thanks are given to Miss Sayaka Takeuchi for her wholehearted, day and night support for my life over the last few years. Last but not least, I want to thank my family for their care.

List of Publications

- C. M. Yim, C. L. Pang and G. Thornton

  'Comment on "Oxygen Vacancy Origin of the Surface Band-Gap State of TiO_2(110)" Reply'

  Phys. Rev. Lett. **104** 259704 (2010).

- C. M. Yim, C. L. Pang and G. Thornton

  'Oxygen Vacancy Origin of the Surface Band-Gap State of TiO_2(110)'

  Phys. Rev. Lett. **104** 036806 (2010).

Contents

List of Figures

Chapter 1

Introduction

Surface science is the study of solid surfaces under well-controlled conditions. Such studies are usually performed on single crystal surfaces under the ultrahigh vacuum (UHV) conditions, i.e. in a background pressure in the range of 10^{-10} mbar. After UHV conditions became routinely achievable, surface scientists have developed experimental techniques enabling measurements of the properties of surfaces. Notably, the invention of scanning probe microscopes (SPMs) has revolutionised research into surfaces by allowing real space imaging with atomic resolution [1, 2]. These techniques have also been used as tools for the manipulation of atoms [3] and molecules [4] thus providing a novel approach for building nano-scale structures on surfaces. Additionally, further development has transformed SPMs into a technique which provides not only imaging, but also chemical specificity at the atomic level [5].

The fact that almost every metal oxidises in the ambient suggests that rather than those of the metal itself, the surface of their oxide deserves more interest. This helps to explain the growing amount of work on such oxide surfaces over the last twenty years. The range of physical and chemical properties of bulk oxide materials is very great. Among them, some are superconductors [6] and some are insulators. While some are inert enough to act as corrosion protection layers, others are chemically active as catalysts [7]. Also, some of the most intriguing magnetic, optical and electronic properties can only be found in this

class of materials [8]. On the practical side, metal oxides are very important for many established and emerging technologies. As a result, understanding the surface properties of oxides−their geometric and electronic structure, their interactions with gas molecules and nanoparticles, as well as the formation of interfaces−is of key interest in many technological areas.

The fact that most metal oxides are insulators makes them unsuitable for the majority of surface science techniques [8]. Several methods have been developed to overcome this problem. The first and simplest way is reduction by vacuum annealing, upon which some metal oxides such as TiO_2 [9] and ZnO [10] can be made semiconducting. Doping has also been employed to boost the conductivity of metal oxides [9]. As for the large band-gap metal oxides (MgO and Al_2O_3) where none of the aforementioned methods is applicable, the only way to study these materials is to grow the corresponding metal oxide thin-films on metal substrates [11, 12]. By doing so, one can study the properties of the metal oxide thin-films, which, when grown above certain thickness thresholds, are believed to exhibit very similar properties to that of their bulk.

TiO_2 is used as a substrate in this thesis. As a versatile material, TiO_2 has been widely used in various technological areas [9]. One notable example is its use in solar cells for the production of hydrogen and electric energy, which relies on its photo-catalytic properties [13]. TiO_2 is also used as supports for metal nanoparticles in heterogeneous catalysts, as gas sensor, as white pigment, as corrosion-protective, to name a few [9]. Recently, it has also been demonstrated that TiO_2 converts formamide into nucleoside bases upon UV irradiation, leading to a speculation that TiO_2 may even play a role in the origin of life [14].

Rutile Titania

Titanium dioxide (TiO_2) naturally exists in three different structures: rutile, anatase and brookite, of which rutile and anatase have been shown to be more active in the applications of TiO_2 and hence dominate the surface science literature. As displayed in Figure 1.1(a), rutile, the only structure of TiO_2 employed in this thesis, has a tetragonal unit cell with dimensions of $a = b = 4.584$ Å, $c = 2.953$ Å. In rutile, the basic building block comprises a titanium atom surrounded by six oxygen atoms in a more or less octahedral configuration. In this structure, the two bonds between the titanium and the oxygen atoms at the apices of the octahedron are slightly longer. The stacking of the octahedra is shown in figure 1.1(b). This results in threefold coordinated oxygen atoms.

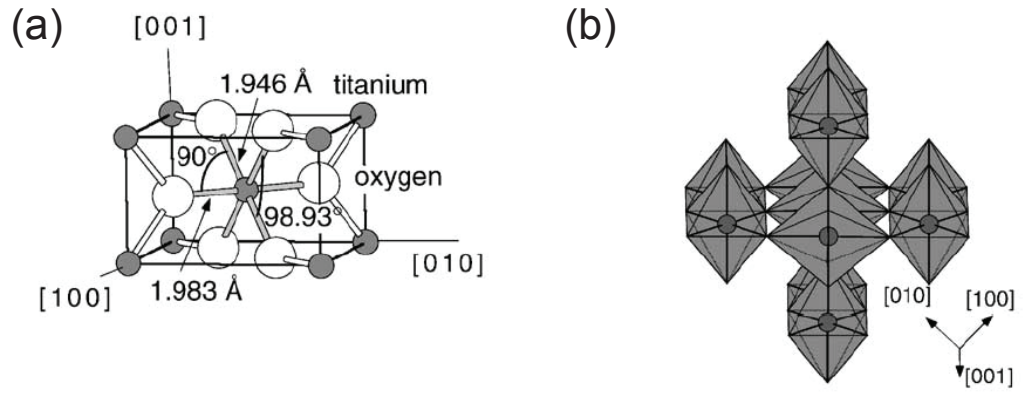

Figure 1.1: (a) The tetragonal bulk unit cell of rutile shown on the left has the dimensions, $a = b = 4.587$ Å, $c = 2.953$ Å. The slight distorted octahedra form the basic building units. The bond lengths and angles of the octahedrally coordinated Ti atoms are indicated. (b) The stacking of the octahedra in rutile, which leads to threefold coordinated oxygen atoms, is displayed on the right [9].

Self-consistent *ab initio* calculations by Ramamoorthy and Vanderbilt [15] show that the (110) surface of rutile TiO_2 has the lowest surface energy while the (001) face the highest. This is also expected from considerations of surface stability, based on electrostatic [16] and dangling bonds arguments [17]. The thermodynamic stability of the (100) and (011) faces were also considered. While the (100) face was found to be stable with respect to forming (110) facets, the (001) face is rather unstable with respect to forming macroscopic (1×1)(011) facets. Perron *et al.* [18] also calculated the stability of difference faces of

rutile TiO_2. They found the (110) face most stable, followed by the (100) and (101) ones. The (001) face was also studied and its calculated surface energy is much higher than the other three faces. The experimental findings on the low-index surfaces agree quite well with the calculations. For rutile, the (110), (100), (011) and (001) surfaces have been studied, with the (110) face being most stable.

As shown in Figure 1.2, the unreconstructed rutile (110)-(1×1) surface contains of two titanium atoms in two environments. Along the [001] direction, rows of sixfold coordinated Ti atoms (as in the bulk) alternate with rows of fivefold coordinated Ti atoms, the latter have dangling bond perpendicular to the surface. Oxygen atoms are present in two different environments as well. Within the main surface plane, they are threefold coordinated as in the bulk. Compared to the bulk, the so-called bridging oxygen atoms are missing one bond to Ti vertically above and are therefore twofold coordinated. The stoichiometric TiO_2 surface is a wide bandgap insulator. However, it can be made semiconducting by reduction upon sputtering and vacuum annealing, leading to the creation of oxygen vacancies, interstitial Ti, and bridging oxygen vacancies on the surface. These bridging oxygen vacancies (O_b vac) have been shown to influence the overall chemistry of the surface [9].

Chapter 2 of this thesis details the principles behind the surface science techniques employed. These include scanning tunnelling microscopy and spectroscopy (STM/STS), low energy electron diffraction (LEED), X-ray photoemission spectroscopy (XPS) and near edge X-ray absorption fine structure (NEXAFS).

Chapter 3 describes the instrumentation that was required to perform the experiments described in chapters 4 to 6. The low-temperature STM UHV system and its adjoining facilities for sample preparation and characterisation are discussed first, followed by a short section concerning the use of synchrotron radiation light at Beamline I311, Max-Lab, the University of Lund, Sweden.

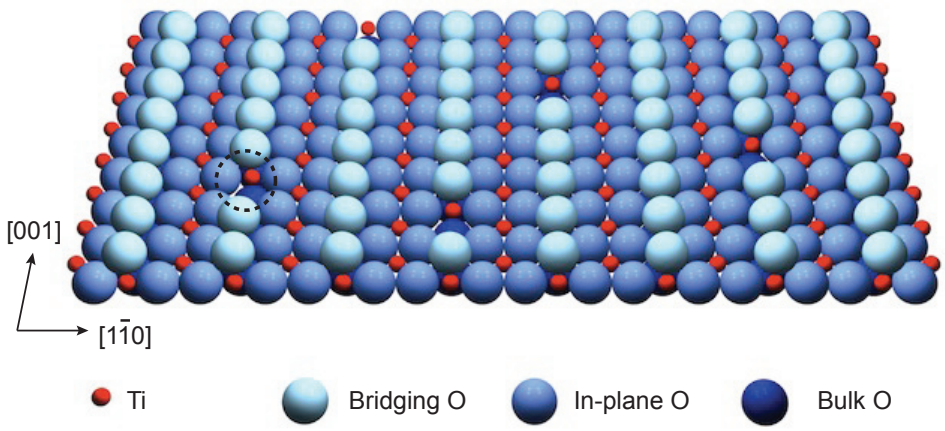

Figure 1.2: Ball model of the rutile TiO_2(110)-(1×1) surface. The surface consists of alternating rows of fivefold-coordinated Ti atoms (red) and twofold coordinated bridging O atoms (light blue) running along the [001] crystallographic direction. A bridging oxygen vacancy is highlighted with a dashed circle.

In chapter 4, there is a detailed description of how the origin of the surface band-gap state in rutile TiO_2(110) was determined using STM and UPS. By employing electron bombardment to vary the density of bridging oxygen vacancies (O_b vac) while monitoring the band-gap state in UPS, we demonstrated that O_b vac makes a major contribution to the surface band-gap state.

Chapter 5 reports a study of CO adsorption on the Pd islands grown on the TiO_2(110) surface. The Pd islands grown on the TiO_2 substrate have a pseudo-hexagonal shape and (111) top facets. In addition, CO molecules are found to bond vertically and form ordered overlayers on the Pd(111) islands.

Chapter 6 describes a study of O_2 adsorption on the cross-link reconstructed TiO_2(110)-(1×2) surface, which is followed by current-imaging tunnelling spectroscopy (CITS) measurements performed on the same substrate at 78 K. By comparing this with DFT calculations by the Shluger group, we hope to determine the geometrical structure of the cross-linked (1×2) reconstruction on rutile TiO_2(110).

The final chapter of this thesis, 7, summarises the results and makes a number of suggestions for future research to build upon this work.

References

[1] G. Binnig and H. Rohrer, *IBM Journal of Research and Development*, 1986, **30**, 355–369.

[2] F. Giessibl, *Phys Rev B*, 1997, **56**, 16010–16015.

[3] D. Eigler and E. Schweizer, *Nature*, 1990, **344**, 524–526.

[4] A. Heinrich, C. Lutz, J. Gupta and D. Eigler, *Science*, 2002, **298**, 1381–1387.

[5] B. Stipe, M. Rezaei and W. Ho, *Science*, 1998, **280**, 1732–1735.

[6] J. Bendorz and K. Muller, *Z Phys B Con Mat*, 1986, **64**, 189–193.

[7] H. Kamata, H. Ohara, K. Takahashi, A. Yukimura and Y. Seo, *Catal Lett*, 2001, **73**, 79–83.

[8] V. E. Henrich and P. A. Cox, *The Surface Science of Metal Oxides*, Cambridge University Press, Cambridge, UK, 1st edn., 1994.

[9] U. Diebold, *Surf Sci Rep*, 2003, **48**, 53–229.

[10] T. Parker, N. Condon, R. Lindsay, F. Leibsle and G. Thornton, *Surf Sci*, 1998, **415**, L1046–L1050.

[11] S. Schintke, S. Messerli, M. Pivetta, F. Patthey, L. Libioulle, M. Stengel, A. D. Vita and W. Schneider, *Phys Rev Lett*, 2001, **87**, 276801.

[12] T. Worren, K. Hansen, E. Laegsgaard, F. Besenbacher and I. Stensgaard, *Surf Sci*, 2001, **477**, 8–16.

[13] A. Fujishima and K. Honda, *Nature*, 1972, **238**, 37–38.

[14] S. Senanayake and H. Idriss, *P Natl Acad Sci Usa*, 2006, **103**, 1194–1198.

[15] M. Ramamoorthy, D. Vanderbilt and R. Kingsmith, *Phys Rev B*, 1994, **49**, 16721–16727.

[16] P. W. Tasker, *J Phys C Solid State*, 1979, **12**, 4977–4984.

[17] J. P. Lafemina, *Crit Rev Surf Chem*, 1994, **3**, 297.

[18] H. Perron, C. Domain, J. Roques, R. Drot, E. Simoni and H. Catalette, *Theor Chem Acc*, 2007, **117**, 565–574.

Chapter 2

Theoretical Aspects of Instrumentation

Abstract

This chapter details the principles behind the surface science techniques employed in this thesis. They are: scanning tunnelling microscopy (STM), low energy electron diffraction (LEED), X-ray/ultraviolet photoemission spectroscopy (XPS/UPS) and near-edge X-ray absorption fine structure (NEXAFS).

2.1 Scanning Tunnelling Microscopy

Invented by Binnig and Rohrer in the early 1980s [1], scanning tunnelling microscopy (STM) has revolutionised the field of surface science. Since then, it has become routine to image surfaces at the atomic level, manipulate individual atoms/molecules [2, 3], and even chemically identify atoms/molecules on surfaces [4].

The working principle of STM is based on the idea of quantum tunnelling, which can be understood by considering a 1-D problem of an electron encountering a rectangular potential barrier $V(x)$ (where $V(x) = V_0$ inside the barrier ($0 < x < a$) and $V(x) = 0$ otherwise). Here, we are only interested in how the electron tunnels through. By solving the corresponding Schrödinger equation, the wavefunction of the electron inside the barrier has the form

$$\psi(x) \propto e^{-\kappa x} \tag{2.1}$$

where $\kappa = [2m(V_0 - E)/\hbar^2]^{\frac{1}{2}}$ is the decay constant and is a function of the energy of the state, E, the barrier height, V_0, and the mass of the electron, m. The transmission probability T, to which the tunnelling current is proportional, has the form

$$T = \left[1 + \frac{V_0^2 \sinh^2 \kappa a}{4E(V_0 - E)}\right]^{-1} \tag{2.2}$$

In the weak transmission regime, $\kappa a >> 1$, T becomes

$$T \propto e^{-2\kappa a} \tag{2.3}$$

In the simplest case, V_0 is the vacuum level. For the electrons at the Fermi level E_{F}, $V_0 - E$ is just the workfunction ϕ. By considering a typical workfunction of a few eV, 2κ is approximately 2 Å^{-1}. This means that increasing (decreasing) the separation of the tip and sample by 2 Å will lead to a drop (rise) in the tunnelling current by an order of magnitude. This exponential current-distance relationship leads to the huge sensitivity of the STM and also means that in most cases the tunnelling can be considered to occur

mainly through a single atom at the tip apex.

Equation 2.3 accounts for the current-separation relationship in STM, but does not explain how tunnelling takes place. As illustrated schematically in Figure 2.1, when a sample and a tip are brought to their thermal equilibrium, the Fermi levels of both sides align with each other, and hence no electrons can tunnel between the two, under Pauli's exclusion principle. For tunnelling to occur, a positively (negatively) biased voltage V is applied to the sample with respect to the tip, leading to a downward (upward) shift of the Fermi level of the sample with respect to that of the tip. In this case, electrons from the filled states of the tip (sample) will tunnel to the empty states of the sample (tip) [5]. In reality, the tunnelling current I not only depends on the transmission probability T but also the applied voltage V as well as the band structures of the surface and the tip. To have a better understanding of the processes involved in STM, it is necessary to examine more complex formalisms, such as those proposed by Tersoff and Hamann [6], Chen [7], Lang [8] and Wentzel-Kramers-Brillouin (WKB) [5].

2.1.1 Tersoff and Hamann

Using first-order perturbation theory [9], Tersoff and Hamann [6] postulated that the tunnelling current I has the form

$$I = \frac{2\pi e}{\hbar} \sum_{\mu,\nu} f(E_\mu)[1 - f(E_\nu) + eV]|M_{\mu,\nu}|^2 \delta(E_\mu - E_\nu) \tag{2.4}$$

where $f(E)$ is the Fermi function, V is the applied voltage, $M_{\mu,\nu}$ is the tunnelling matrix element between states ψ_μ of the tip and ψ_ν of the surface, and E_μ is the energy of the state ψ_μ in absence of tunnelling. In the limits of small voltage and temperature, equation 2.4 reduces to

$$I = \frac{2\pi}{\hbar} e^2 V \sum_{\mu,\nu} |M_{\mu,\nu}|^2 \delta(E_\nu - E_F)\delta(E_\mu - E_F) \tag{2.5}$$

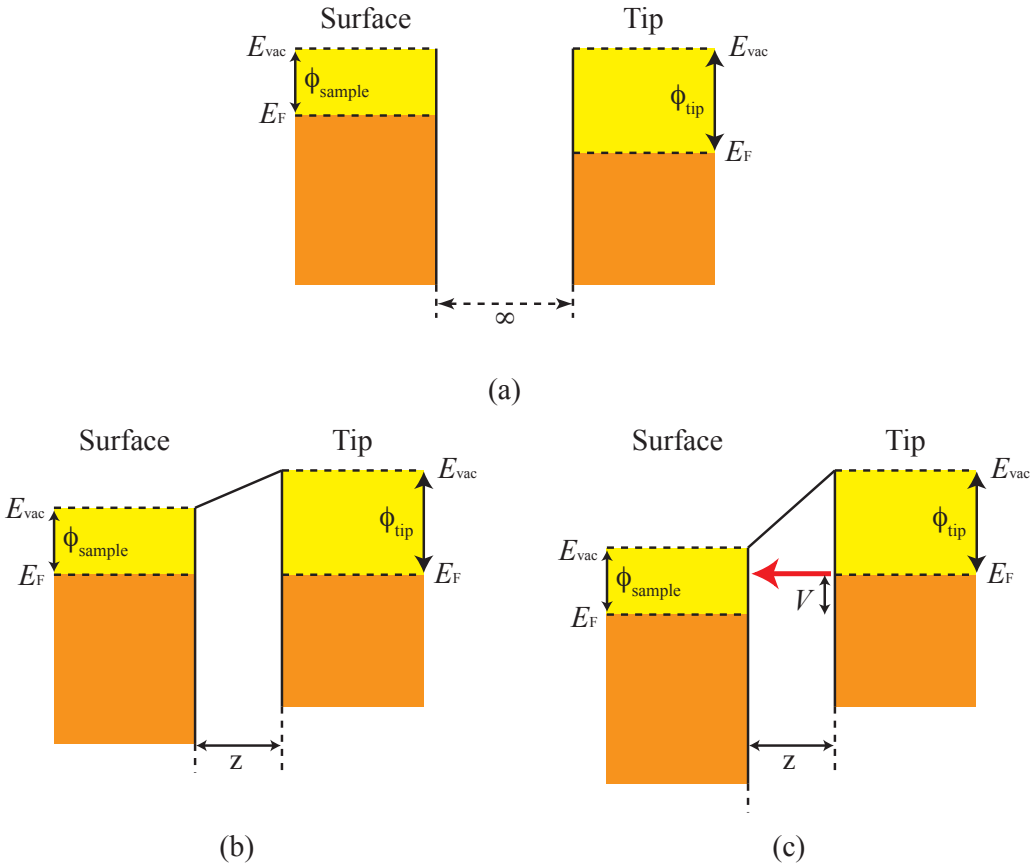

Figure 2.1: Diagrams describing the band structures of surface and tip and the potential barrier in between in three different cases: (a) when the surface and the tip are separated infinitely, (b) when they are brought very close to each other at zero bias and (c) as (b) but with sample bias V ($V > 0$). z is tip-sample separation, E_F the Fermi level, E_{vac} the vacuum level, And ϕ_{sample} and ϕ_{tip} the workfunctions of the sample and the tip, respectively.

To solve Equation 2.5 in general, one needs to calculate $M_{\mu,\nu}$. Bardeen demonstrated that the matrix elements $M_{\mu,\nu}$ can be expressed as equation 2.6: [9]

$$M_{\mu,\nu} = \frac{\hbar^2}{2m} \int d\vec{S} \cdot (\psi_\mu^* \vec{\nabla} \psi_\nu - \psi_\nu^* \vec{\nabla} \psi_\mu^*) \tag{2.6}$$

where the surface integral $\int d\vec{S}$ in the matrix element is integrated over any surface lying entirely within the (vacuum) barrier region separating the two sides. Rather than evaluating the matrix elements $M_{\mu,\nu}$, Tersoff and Hamann first considered the simplest case of a point probe, which is representative of an ideal measurement with the maximum possible resolution. Based on this assumption, the matrix element is proportional to the amplitude of ψ_ν at the position $\vec{r_0}$ of the probe, and equation 2.5 reduces to

$$I \propto \sum_{\nu} |\psi_{\nu}(\overrightarrow{r_0})|^2 \delta(E_{\nu} - E_{\mathrm{F}}) \tag{2.7}$$

This shows that the tunnelling current I is proportional to the surface local density of states (LDOS) at E_{F}, and hence the surface charge density at E_{F}. As a result of this it can be considered that the STM image represents a contour map of constant surface LDOS. Although this model is simplistic in its treatment of the tip as a point probe, its prediction is quite close to those anticipated in Tersoff and Hamann's more realistic models that assume an s-wave tip [6].

2.1.2 Chen

Tersoff and Hamann [6] predicted a lateral resolution of 6 Å which clearly disagrees with the experimental observations which resolved features with spacings as low as 2 Å [10]. An explanation to this was provided by Chen [7], who discarded the s-wave approximation and predicted atomic resolution on metal surfaces. In fact, the s-wave approximation is very likely to be invalid for most tip materials such as tungsten (W), platinum (Pt) and iridium (Ir), which are d-band metals and have a Fermi level DOS mainly contributed from d states. In addition to this, it is often considered that the d-states of W have a strong tendency to form highly localised d_{z^2} dangling bonds, which play a major role in tunnelling.

Chen also explained the effect of a d_{z^2} tip using the reciprocity principle in STM (see figure 2.2). According to the principle, for an s-wave tip, the STM image of a metal surface is the charge-density contour. On the other hand, for a d-wave tip, the tip traces the charge-density contour of a *fictitious surface* with a d_{z^2} state on each atom, and exhibits much stronger atomic corrugation than that of the charge density.

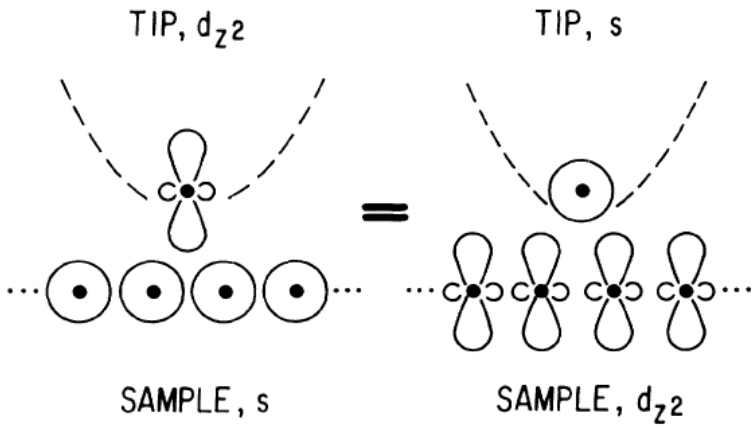

Figure 2.2: Illustration of reciprocity principle showing that scanning an *s*-wave sample with a d_{z^2}-wave tip is equivalent to scanning a d_{z^2}-wave sample with an *s*-wave tip in STM. Taken from ref. [7]

2.1.3 Lang

To investigate the effect of adsorbates on STM imaging, Lang [8] performed some calculations on imaging different atoms using Bardeen's tunnelling formalism and considering two flat electrodes, one with an Na atom on it as a tip, and the other as a surface with different adsorbate atoms (He, Na and S) on it. His calculations showed that the Na *3s* and S *2p* resonances lead to an increase in the LDOS at the Fermi level, while the presence of He results in a reduction in the LDOS by polarising the metal states away from the Fermi level. This change in the LDOS leads to the adsorbates appearing as protrusions (Na, S) or depressions (He) in the constant current mode STM images. This finding suggests that the analysis of STM images is by no means trivial, and in order to have an accurate interpretation, comparing the STM images with calculations is often necessary.

2.1.4 WKB Approximation

The applied voltages used in most STM measurements (especially on metal oxide surfaces) are from 1 to 3 eV or even higher. Under such conditions the Tersoff and Hamann theory [6] is very likely to fail in that electronic states below the Fermi level also start to contribute to tunnelling. In this case, it becomes more sensible to consider the semi-classical Wentzel-

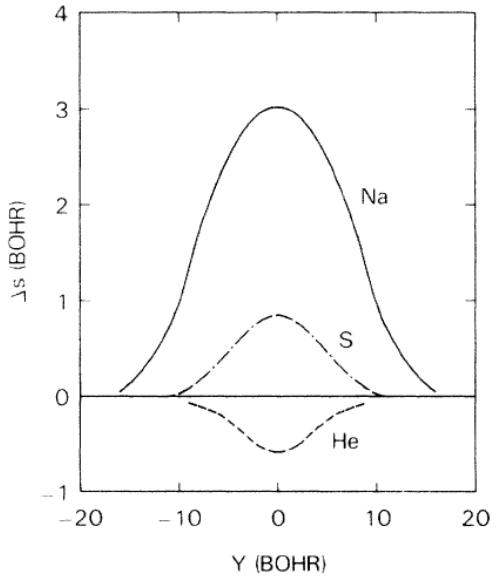

Figure 2.3: Calculated change is tip distance δs versus lateral displacement Y for an STM scan of adsorbate atoms (Na, S, He) on a jellium surface at small voltage bias. 1 bohr = 0.529 Å [8]

Kramers-Brillouin (WKB) approximation, in which the tunnelling probability is calculated between two planar electrodes at zero temperature and the tunnelling current I is an integral over the energy range where both filled-initial and empty-final states are available for tunnelling [5]. In their formalism, the tunnelling current I has the form

$$I = \int_0^{eV} \rho_s(r, E)\rho_t(r, -eV + E)T(E, eV, r)dE \tag{2.8}$$

where $\rho_s(r, E)$ and $\rho_t(r, E)$ are the density of states of sample and tip at location r and energy E, measured with respect to their individual Fermi levels. For negative (positive) sample bias, $eV < 0$ (> 0). The transmission probability T, which is a function of energy E and biased voltage V, is given by

$$T(E, eV) = exp\left[-\frac{2z\sqrt{2m}}{\hbar}\sqrt{\frac{\Phi_s + \Phi_t}{2} + \frac{eV}{2} - E}\right] \tag{2.9}$$

where z is the tip-sample distance. Equation 2.9 shows that the tunnelling current is a function of the density of states of sample ρ_s and tip ρ_t as well as transmission probability T. By careful examination, we found that if $eV < 0$, the transmission probability T is largest for $E = 0$. Similarly, if $eV > 0$, T is largest for $E = eV$. This means that the electronic states close to the Fermi level contribute most to the tunnelling current.

2.1.5 Scanning Tunnelling Spectroscopy (STS)

Apart from imaging, STM can also be used for probing local density of states (LDOS) on surfaces at the atomic level. This is usually performed by taking an I-V curve at every point on the surface while imaging. This technique can also be used to study the LDOS of atomistic features on thin-films as well as variation in LDOS induced by adsorbates. To understand how tunnelling spectroscopy and LDOS are related, we start from differentiating equation 2.8, which gives

$$\frac{dI}{dV} = \rho_s(r, eV)\rho_t(r, 0)T(eV, eV, r) + \int_0^{eV} \rho_s(r, E)\rho_t(r, E - eV)\frac{dT(E, eV, r)}{dV}dE \quad (2.10)$$

The first term in equation 2.10 is the product of the density of states of sample and tip, and tunnelling probability T. The second term contains the voltage dependence of the tunnelling probability.

The tunnelling probability T is a smooth, monotonically increasing function of the applied voltage V, and hence contributes a smooth background on which the spectroscopic information is superimposed. For a metallic tip, the DOS is generally considered to be a constant and hence it can be considered that dI/dV is proportional to the LDOS of the surface.

There are two ways to perform STS measurement. The first one is called point-$I - V$ spectroscopy, in which scanning is interrupted at a point of interest on the surface, with the feedback loop switched off (to keep the tip-sample separation constant), and the voltage is ramped while monitoring the tunnelling current I. Usually, a number of $I - V$ spectra are obtained at various points on the surface and then averaged to improve the signal-to-noise ratio. The dI/dV spectra, which contain the information on the LDOS as described earlier, can be obtained either by differentiating the $I - V$ curves numerically following acquisition or obtained directly with the use of a lock-in amplifier during mea-

surement. Another way is called current imaging tunnelling spectroscopy (CITS). CITS combines the imaging and spectroscopic capability of STM to obtain atomically resolved spectroscopy of a desired surface. During CITS, at each pixel within a scan, the feedback loop is switched off and a point $I-V$ spectrum obtained before switching on the feedback loop again and moving to the next pixel. By doing this, a current image is built up at all bias voltages in the range of the $I-V$ curve and by differentiating the individual spectra, a 2-D map which is representative of the LDOS can be obtained. However, obtaining good data using CITS is not trivial and requires an extremely stable tip, a thermally stable environment and very low noise levels within the STM. This explains why it is always preferable to perform CITS at cryogenic temperatures.

2.2 Low Energy Electron Diffraction (LEED)

In 1927, Davisson and Germer demonstrated that when a beam of monoenergetic electrons is directed to a single crystal, the elastically back-scattered electrons emerge in preferential directions, which is governed by the periodic nature of the crystal lattice. This phenomenon forms the basis of LEED. Since then, LEED has proved to be a very useful tool for the investigation of structure on surfaces, and Davisson and Germer were honoured for their discovery by being awarded the Nobel Prize in 1937.

Figure 2.4 illustrates how a parallel electron beam is diffracted from a 1-D array of metal ion cores separated by a distance of d. By considering two parallel incoming beams, it is seen that the path difference Δs between the two is given by Equation 2.11:

$$\Delta s = d \cdot (\sin\theta - \sin\alpha) \tag{2.11}$$

Constructive interference between the diffracted beams occurs only when the path difference, Δs, is equal to an integer number of wavelengths

$$d \cdot (\sin\theta - \sin\alpha) = n \cdot \lambda \tag{2.12}$$

In the simplest case where $n = 1$, if α and θ are known, the atomic separation d can be determined using Equation 2.12. This simple 1-D example can easily be extended to 2-D. Hence, by measurement of diffraction pattern, the structure of a crystal surface can be determined. In addition, LEED can also be used for LEED I-V measurements, where both the position and intensity of the diffraction peaks are probed at different energies. By comparing the results with the simulated LEED patterns from first principle calculation, the arrangement of atoms in the first few atomic layers of a surface can be determined.

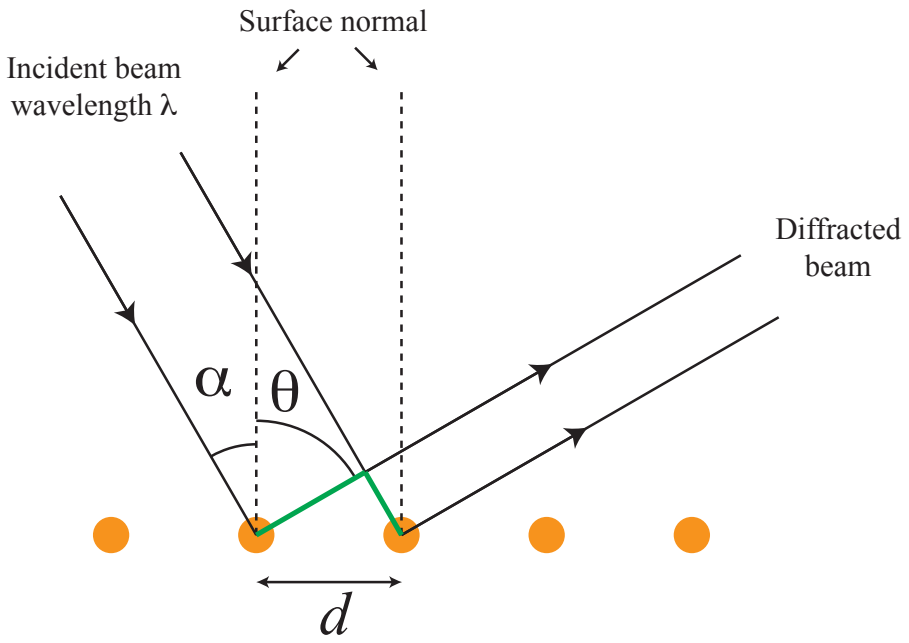

Figure 2.4: Diffraction from a 1-D array of metal ion cores with the incident electron beam away from the surface normal. d is the separation between adjacent metal ion cores. α and θ are the angles of the incoming and outgoing beams respectively. Green lines denotes the path difference between the parallel beams.

In LEED, the electron energies used range between 50-200 eV, at which the escape depth of electrons is approximately 5 Å (see Figure 2.5). This means that LEED is a rather surface-sensitive tool for determining structure on surfaces.

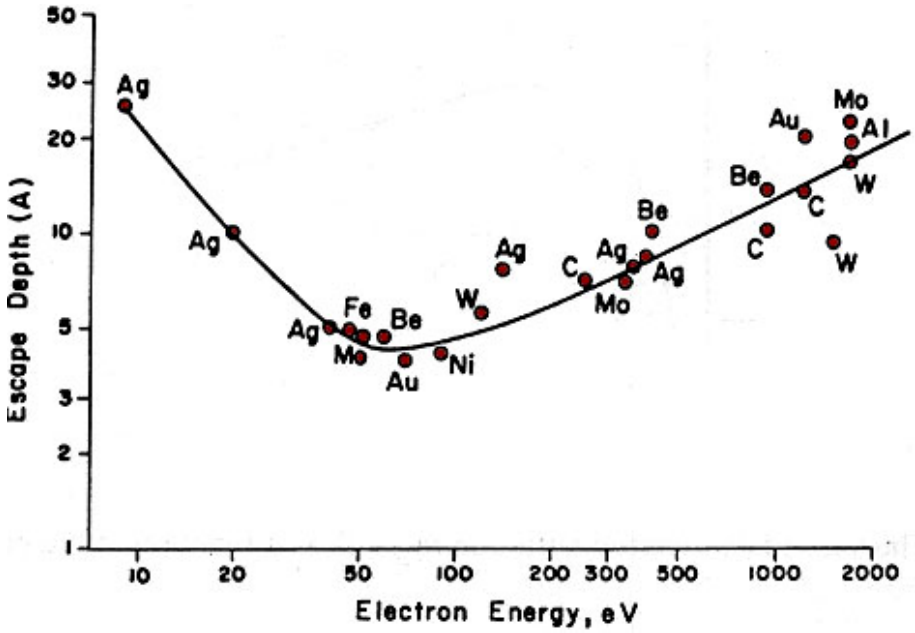

Figure 2.5: Experimentally determined escape depth of electrons as a function of initial kinetic energy for a range of materials. [11]

2.3 Photoemission and Auger Processes

As shown in figure 2.6(a), when a crystal is irradiated with a beam of monochromatic light with photon energy $h\nu > E_B$, the core-level electron will be photo- excited and overcome its binding force towards its nucleus to reach the vacuum level. By measuring the kinetic energies of those photoelectrons, their core-level binding energies can be determined according to the following relation [12]:

$$h\nu = E_B + E_{K,XPS} + \phi_s - \phi_a \tag{2.13}$$

where $h\nu$ is the photon energy, and ϕ_s and ϕ_a are the work functions of the sample and energy analyser, respectively. The binding energies E_B of the core-level electrons are characteristic of the examined atomic species and their chemical states.

In XPS, the shape of a core-level peak is a convolution of a Lorentzian and a Gaussian lineshape, with the former accounting for the inherent peak width and the latter for experimental factors including finite width of the photon source, energy resolution of the analyser, and thermal broadening. The inherent width of a core level, Γ, is directly related

to the core-hole lifetime, τ, according to Heisenberg's uncertainty principle [13]:

$$\Gamma \approx \frac{\hbar}{\tau} \tag{2.14}$$

When the material being examined is metal, the Lorentzian shape is substituted by a Doniach-Sunjic shape, consisting of a Lorentzian function and an asymmetric tail lying on the higher E_B side of the core-level peak. This tail accounts for shake-up type events arising from unfilled one-electron levels above the Fermi level [12].

Due to the limited escape-depth of electrons in solids (Figure 2.5), the electrons reaching the analyser are sampled from the top 10-20 Å from the surface. Alternatively, if the attenuation length of electrons in a given material is known, the thickness of that material deposited on a substrate can be determined by means of depth-profiling.

Similarly to XPS, UPS employs UV light to probe the valence band of surfaces. The shorter E_k range of the emitted photoelectrons ($\sim$50 eV) makes UPS a better tool to study the binding and orientation of adsorbates on surfaces. UPS can also be used to measure the surface work function [14]. Moreover, by incorporating rotational degrees of freedom to either the sample or the analyser, UPS can be employed to investigate angular dependence of the band structures of surfaces [15].

Any core-hole created will be refilled by means of either Auger decay or fluorescence, and it was found that for light elements Auger decay dominates. As shown in Figure 2.6(b), in Auger decay, the core-hole is filled by the electron at the shallower level E_{s1}, with all the remaining energy transferred to the electron at level E_{s2}, which then becomes energetic enough to overcome its binding force towards the nucleus and reach the vacuum level. The kinetic energy of the Auger electron $\mathrm{E}_{K,Auger}$ can be calculated according to the following relation

$$E_{K,Auger} = E_B - E_{s1} - E_{s2} \tag{2.15}$$

where E_B is the energy level of the core-hole, E_{1s} is the initial energy of the decaying electron and E_{2s} is the initial energy of the emitted electron. The value of $E_{K,Auger}$ depends on the interplay between energy levels, making Auger transition suitable for elemental charaterization.

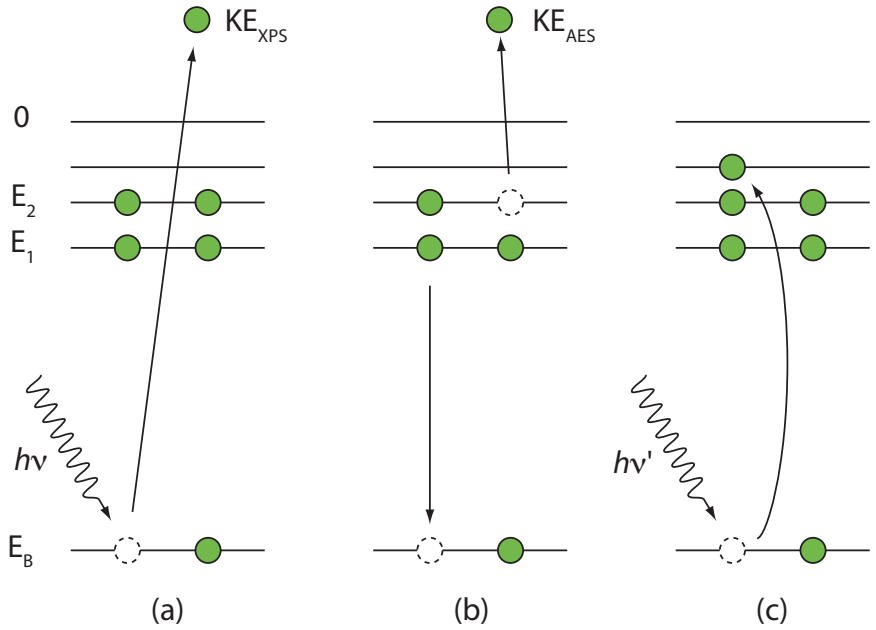

Figure 2.6: Simplified illustrations of different processes. (a) In XPS, an core-level electron, which is excited by an incident photon, is energetic enough to overcome its binding energy (E_B) and reach the vacuum. (b) In Auger decay, the core-hole is filled by the electron from the shallower level E_{s1} with the remaining energy transferred to the electron at level E_{s2}, which then overcomes its binding energy and reaches the vacuum with $K_{E,Auger}$. (c) X-ray adsorption: the adsorption of a photon to excite a core level electron to an unoccupied state in the valence band.

2.4 Near-Edge X-Ray Absorption Fine Structure (NEXAFS)

X-ray absorption spectroscopy (XAS) is a spectroscopic method to measure the X-ray absorption coefficient of a material as a function of photon energy. In the case of measuring the absorption coefficient (μ) on a thin sample, a monochromatic X-ray beam is shone onto the sample and the incident and transmitted light intensities are recorded as the incident X-ray energy is increased. The incident (I_0) and transmitted light intensities (I_t), and the absorption coefficient, μ, are related to each other according to the following

equation

$$I_t = I_0 e^{-\mu x} \tag{2.16}$$

where x is the thickness of the sample.

When the incident photon energy matches the binding energy of an electron of an atom within the sample, the intensity of X-rays absorbed by the sample increases dramatically, causing a significant drop in the transmitted X-rays intensity. This leads to an absorption edge. In fact, each element has a set of unique absorption edges that correspond to different binding energies of its electrons. This gives XAS element specificity. XAS is usually performed at synchrotron facilities due to its requirement of tuneable photon energy. Also, due to the highly penetrating power of X-rays, XAS samples can be solids, liquids or gases. In addition, the brilliance of synchrotron X-ray sources enables XAS to detect elements with concentration as low as a few ppm.

XAS is also employed to study the interaction of molecules with surfaces. When a photon of sufficient energy excites a core hole, the resultant photoelectron will either promote to unoccupied states or leave from its parent atom. The resulting core hole is then relaxed via Auger transition or fluorescence, with the former dominant for low Z elements. As a result, the X-ray absorption spectra can be collected by probing the electron yield from the sample as a function of photon energy. This also gives XAS surface sensitivity thanks to the finite escape depth of electrons in solids.

A typical X-ray absorption spectrum consists of two regions: the near-edge region (up to 40 eV above the absorption edge) and the region where the extended X-rays absorption fine structure (EXAFS) oscillation begins. The near-edge region, which contains information regarding photo-excitation of core-level electrons to unoccupied states, is explored by near-edge X-rays absorption fine structure (NEXAFS), while the latter region explored by surface extended X-rays absorption fine structure (SEXAFS). Their key difference is that while NEXAFS is sensitive to bond-angles, EXAFS is sensitive to the interatomic

distances. As only NEXAFS is employed in this thesis, the following discussion focuses on NEXAFS only.

NEXAFS is mainly employed to elucidate the structures of molecules bonded to surfaces by gauging their near-edge absorption behaviour. Usually, in NEXAFS one selects a specific atomic species through its particular absorption edge and probes its bonds to intramolecular and, to a lesser extent, extra-molecular neighbours, i.e. surfaces. Unlike other XAS, NEXAFS is dominated by electronic excitations into the bound and quasi-bound states of the molecules, not by those into the more delocalised states of the substrate. This makes analysis of NEXAFS spectra a lot easier than expected; it is generally accepted that most of the features found in the NEXAFS spectrum of a simple molecule adsorbate can be analysed in a relatively straightforward manner without relying on demanding multi-scattering calculations. Other advantages of NEXAFS include its capability of detecting the presence of specific bonds in molecules, determining their bond lengths, and deriving the orientation of molecules and functional groups on surfaces. In this work, NEXAFS was only used to study the orientation of molecules bonded to surfaces. As such, the theoretical discussion that follows focuses on this aspect only.

2.4.1 Angular Dependence of π^* and σ^* Resonances

The π^* and σ^* resonances typically observed in K-edge NEXAFS spectra can be described in molecular-orbital (MO) principles as dipole transitions from s initial states to p-component of the π^* and σ^* final states. The intensity of the transitions can be derived from Fermi's Golden rule, which links the resonance intensity to the transition matrix element

$$I \propto |< f \mid \mathbf{E} \cdot \mathbf{p} \mid i >|^2 \tag{2.17}$$

where $\mathbf{E}$ is the electric field, $\mathbf{p}$ is the momentum operator and $\mid i >$ is the $1s$ initial state and $\mid f >$ is the molecular orbital final state of the transition. Equation 2.17 can be

re-written in the form

$$I \propto | \mathbf{E} \cdot < f \mid \mathbf{p} \mid i > |^2 \tag{2.18}$$

For $1s$ initial state, the vector matrix element will be directed along the p-like final state orbital and equation 2.18 assumes the simple form

$$I = A \cos^2 \delta \tag{2.19}$$

where A describes the angle-integrated cross section and δ is the angle between the electric field vector $\mathbf{E}$ and the direction of the final orbital $\mathbf{O}$, i.e. the direction of the maximum orbital amplitude. Equation 2.19 represents the angular intensity dependence for molecules which can be described by π^* and σ^* vectors. For molecules with π^* and σ^* planes, the resonance intensity has the form

$$I_P = B \sin^2 \epsilon \tag{2.20}$$

where ϵ is the angle between $\mathbf{E}$ and the normal $\mathbf{N}$ of the molecular orbital plane. For chemisorbed molecules the transition intensities depend on the orientation of the electric field vector $\mathbf{E}$ relative to that of the molecule. The two cases where the π^* and σ^* orbitals are described by a vector or a plane are shown in Figure 2.7 and 2.8, in which the coordinate system which defines the geometry of the molecular orbitals is indicated. For the vector case shown in Figure 2.7 the angle δ between the $\mathbf{E}^{\parallel}$ and the vector $\mathbf{O}$ along the π^* or σ^* orbital can be expressed as a function of the angle θ between $\mathbf{E}^{\parallel}$ and the surface normal $\mathbf{n}$, the polar angle α and azimuthal angle ϕ of the vector $\mathbf{O}$. From Equation 2.19, we obtain the angular dependence of the resonance intensity associated with the $\mathbf{E}^{\parallel}$ component as

$$I_v^{\parallel} = A(\cos^2\theta \cos^2\alpha + \sin^2\theta \sin^2\alpha \cos^2\phi + 2 \sin\alpha \cos\alpha \sin\theta \cos\theta \cos\phi) \tag{2.21a}$$

Similarly, we obtain the angular dependence of the resonance intensity assiociated with the $\mathbf{E}^{\perp}$ component as

$$I_v^{\perp} = A \sin^2\alpha \sin^2\phi \tag{2.21b}$$

For the case of π^* or σ^* orbitals in a plane, shown in Figure 2.8, by using a similar

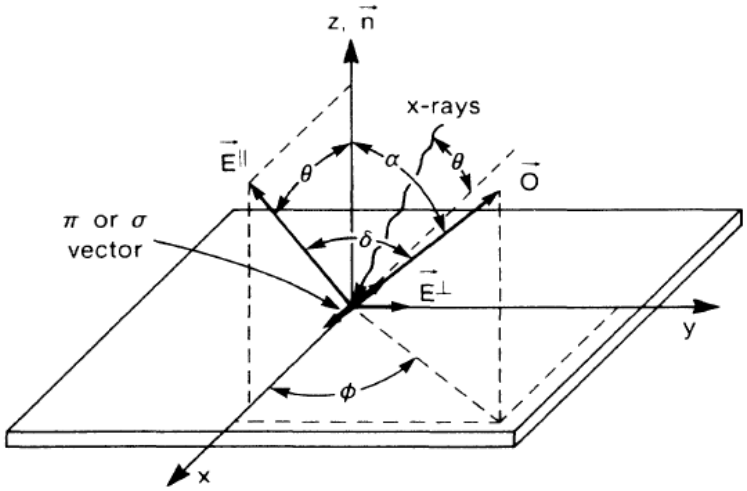

Figure 2.7: Coordinate system defining the geometry of a σ^* or π^* vector orbital on the surface. The orientation of the orbital, that is, of vector **O**, is characterised by a polar angle α and an azimuthal angle ϕ. The x rays are incident in the (x, z) orbit plane of the storage ring which contains the major electric-field vector component $\mathbf{E}^{\parallel}$. The x-ray incidence angle θ, which is also the polar angle of $\mathbf{E}^{\parallel}$ is changed by rotating the crystal about the y-axis. The weaker component $\mathbf{E}^{\perp}$ lies in the surface plane, along the y-axis. The z-axis is the surface normal and the azimuthal rotation axis of the crystal. Taken from ref. [16]

notation, we obtain

$$I_p^{\parallel} = B(1 - \cos^2\theta\cos^2\gamma - \sin^2\theta\sin^2\gamma\cos^2\phi - 2\sin\gamma\cos\gamma\sin\theta\cos\theta\cos\phi) \tag{2.22a}$$

and

$$I_p^{\perp} = B(1 - \sin^2\gamma\sin^2\phi) \tag{2.22b}$$

where γ is the angle between the surface normal **n** and the normal **N** of the π^* or σ^* plane.

2.4.2 Determination of Molecular Orientation

The elliptically polarized nature of synchrotron radiation makes the angular dependence of π^* or σ^* resonances less pronounced than for fully linearly polarized light with $\mathbf{E} = \mathbf{E}^{\parallel}$.

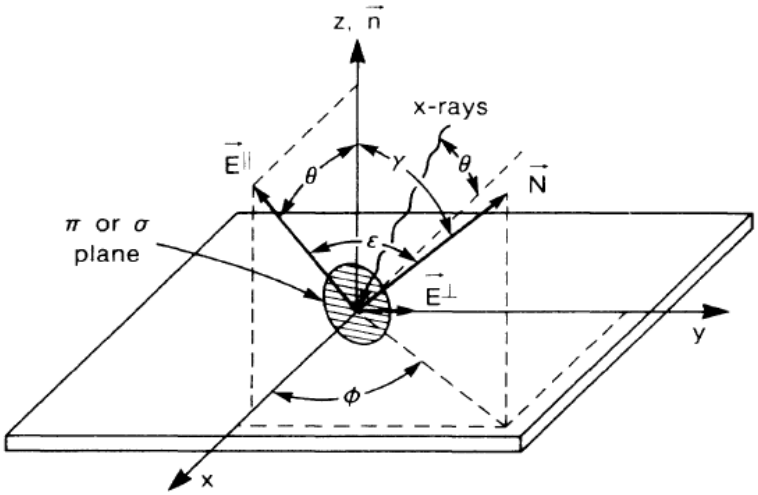

Figure 2.8: Same as 2.7 for a π^* or σ^* orbital plane. The plane is characterised by the polar (γ) and azimuthal (ϕ) orientation of its normal **N**. The plane is tilted from the surface by γ. Taken from ref. [16]

The degree of linear polarisation (or polarization factor) P in the plane of the electron beam orbit,

$$P = \mid \mathbf{E}^{\parallel} \mid^2 / (\mid \mathbf{E}^{\parallel} \mid^2 + \mid \mathbf{E}^{\perp} \mid^2) \tag{2.23}$$

Using P in equation 2.23, the measured resonance intensity is given by

$$I = C[PI^{\parallel} + (1 - P)I^{\perp}] \tag{2.24}$$

where C is a constant.

2.4.2.1 Effect of substrate symmetry

Stöhr and Outka [16] have shown that the azimuthal dependence of the resonant intensities can be eliminated in many cases by taking substrate symmetry into account. Here we discuss its effect on Equations 2.21 and 2.22. For twofold symmetry, the resonant intensities for the "vector" case are

$$I_v^{\parallel} = A(\cos^2\theta\cos^2\alpha + \sin^2\theta\sin^2\alpha\cos^2\phi) \tag{2.25a}$$

and

$$I_v^{\perp} = A \sin^2\alpha \sin^2\phi \tag{2.25b}$$

And for the "plane" case, we have

$$I_p^{\parallel} = B(1 - \cos^2\theta \cos^2\gamma - \sin^2\theta \sin^2\gamma \cos^2\gamma) \tag{2.26a}$$

and

$$I_p^{\perp} = B(1 - \sin^2\gamma \sin^2\phi) \tag{2.26b}$$

For threefold and higher symmetry, the resonant intensities for the "vector" case are

$$I_v^{\parallel} = \frac{A}{3}[1 + \frac{1}{2}(3\cos^2\theta - 1)(3\cos^2\alpha - 1)] \tag{2.27a}$$

and

$$I_v^{\perp} = \frac{A}{2}\sin^2\alpha \tag{2.27b}$$

And for the "plane" case, we have

$$I_p^{\parallel} = \frac{2B}{3}[1 - \frac{1}{4}(3\cos^2\theta - 1)(3\cos^2\gamma - 1)] \tag{2.28a}$$

and

$$I_p^{\perp} = \frac{B}{2}(1 + \cos^2\gamma) \tag{2.28b}$$

Thus for threefold or higher symmetry the azimuthal angular dependence vanishes and the expressions are equivalent to those for cylindrical symmetry about the surface normal.

References

[1] G. Binnig and H. Rohrer, *IBM Journal of Research and Development*, 1986, **30**, 355–369.

[2] F. Chiaravalloti, D. Riedel, G. Dujardin, H. P. Pinto and A. S. Foster, *Phys Rev B*, 2009, **79**, 245431.

[3] G. Dujardin, A. Mayne, O. Robert, F. Rose, C. Joachim and H. Tang, *Phys Rev Lett*, 1998, **80**, 3085–3088.

[4] W. Ho, *J Chem Phys*, 2002, **117**, 11033–11061.

[5] *Scanning Tunneling Microscopy and Spectroscopy: Thoery, Techniques, and Applications*, ed. D. A. Bonnell, VCH Publishers, Inc., New York, 1993.

[6] J. Tersoff and D. Hamann, *Phys Rev B*, 1985, **31**, 805–813.

[7] C. J. Chen, *Phys Rev Lett*, 1990, **65**, 448–451.

[8] N. D. Lang, *Phys Rev Lett*, 1986, **56**, 1164–1167.

[9] J. Bardeen, *Phys Rev Lett*, 1961, **6**, 57–59.

[10] J. Wintterlin, J. Wiechers, H. Brune, T. Gritsch, H. Höfer and R. J. Behm, *Phys. Rev. Lett.*, 1989, **62**, 59–62.

[11] J. Hudson, *Surface Science: An Introduction*, John Wiley, 1998.

[12] *Practical Surface Analysis*, ed. D. Briggs and M. P. Seah, John Wiley and Sons Ltd, England, 2nd edn., 1990, vol. 1.

[13] L. Schiff, *Quantum Mechanics*, McGraw-Hill, 1968.

[14] Y. Park, V. Choong, Y. Gao, B. Hsieh and C. Tang, *Appl Phys Lett*, 1996, **68**, 2699–2701.

[15] P. Wincott, J. Irwin, G. Jones, P. Hardman, G. Thornton, S. Weichel, P. Moller and V. Dhanak, *Surface Science*, 1997, **377**, 242–246.

[16] J. Stohr and D. Outka, *Phys Rev B*, 1987, **36**, 7891–7905.

Chapter 3

Instrumentation

Abstract

This chapter aims to describe the instrumentation employed. The STM experiments were carried out using the low-temperature scanning tunnelling microscope (LT-STM) set-up in the London Centre for Nanotechnology at UCL. The synchrotron radiation studies were performed at Beamline I311 at Max-Lab, University of Lund, Sweden.

3.1 Ultra High Vacuum (UHV)

All experiments described in this thesis were carried out under UHV conditions in order to minimize the interaction of the surface with gas molecules in the environment. Assuming that every single gas molecule collides with the surface with unity sticking probability, we can estimate that the surface will be fully covered with a monolayer of gas molecules after a few hours at a pressure of 1×10^{-10} mbar. In addition, due to the limited mean free path of electrons between collisions in gas phase, a number of surface science techniques such as electron spectroscopy can only be operated under UHV conditions.

3.2 The Low Temperature STM UHV System

As shown in 3.1, the UHV LT-STM system comprises separate analysis and preparation chambers, separated with a gate-valve. The analysis chamber houses a bath-cryostat Omicron *GmbH* LT-STM, which can operate at temperatures between 5 K and 300 K. The preparation chamber is equipped with standard sample preparation facilities (ion sputtering gun), a high-purity gas-line system, and other analytical facilities such as low energy electron diffraction (LEED), ultra-violet/X-ray photoelectron spectroscopy (UPS/XPS), and quadrupole mass-spectrometry. To maintain UHV conditions, both chambers are supported by ion-getter and titanium sublimation pumps, with the preparation chamber also connected to a turbo-molecular pump. The two chambers are accessible via a long-travel high-precision manipulator, on which an electron-bombardment heater for sample annealing is equipped. The set-up of analytic tools will be addressed shortly.

In the atmosphere, apart from the major components like N_2 and O_2, there are water and other light hydrocarbons (CH_4, for example) that have much lower out-gassing rate and thus much harder to be evacuated from a UHV chamber at room temperature. To create UHV conditions, they have to be removed from the chamber, and a bake-out process is required to achieve this goal. First, the LT-STM chamber is pumped down to $\sim10^{-7}$ mbar

with a turbo-molecular pump. After that, and before the bake-out starts, some preparation work is required. This includes removing all non bakeable items from the system, wrapping all the UHV windows with aluminium foil (to avoid cracking arising from uneven thermal distribution), and grounding all the electrical feedthroughs (to avoid charge build-up during bake-out). Then and following a primary leak-test showing no air-leaks, the LT-STM chamber is fully covered with thermal-insulation panels, and ready for the bake-out using heating elements contained within the UHV system table. In contrast to other UHV systems, due to the design of its cryostat-bathed STM stage the LT-STM system requires a much longer bake-out duration (∼48 hours). Following a ∼48 hours bake at 140 °C, nearly all the gaseous components are evacuated from the chamber, leaving only small amount of H_2, H_2O and CO behind. Then, the STM chamber is cooled down to room temperature, during which the ion-getter pumps are switched on, and the titanium sublimation pumps are fired at regular intervals to maintain a pressure inside the chambers of $\sim 10^{-11}$ mbar.

3.3 Facilities for Sample Preparation

3.3.1 Manipulation and Heating of Samples in UHV

Samples were mounted with tantalum clips spot-welded onto Ta sample plates. Transfer of samples within the LT-STM UHV system is achieved by using a magnetic transfer arm between the fast-entry lock and the preparation chamber and a high-precision manipulator between the preparation and analysis chambers. The manipulator offers x-, y-, z-translational and 360-degree rotational motions, and a heating unit.

The heating unit comprises a heater plate, on which the sample (together with its sample holder) sits during manipulation, and a filament box. Heating is achieved by electron bombardment. Electrons emitted from hot tungsten filaments are accelerated towards the heater plate held at high positive bias, resulting in heating. Heating power is controlled by adjusting the filament current and the bias of the heater plate and therefore the electron flux reaching the heater plate. The sample temperature is measured using a K-type

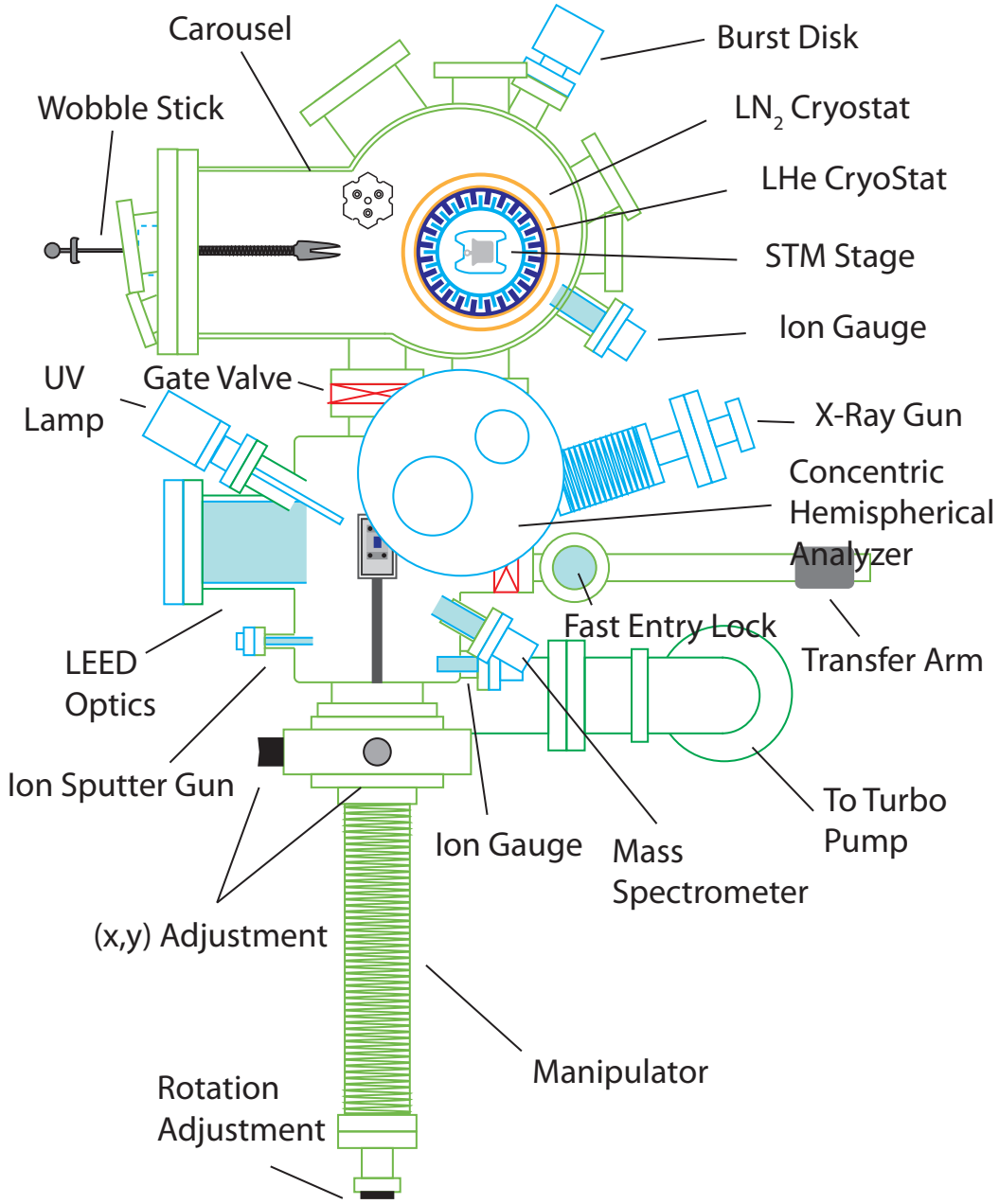

Figure 3.1: A Schematic Diagram of the LT-STM UHV system.

thermocouple spot-welded onto the heater plate or an infra-red pryometer. The maximum annealing temperature is also dependent on the sample dimensions and the design of the sample holder.

3.3.2 Ion Gun

An ion gun is employed for sputtering. It consists of a tungsten filament, a high-voltage (HV) grid and a set of focussing components. A back-filling leak valve, which is attached nearby the ion gun, is employed to inject argon gas into the chamber. During sputtering, electrons from the hot filament are accelerated towards the HV grid (which is biased at 1 kV), around which the electrons bombard the argon atoms, ionising them. The argon ions are accelerated under the electric field between the grid and the grounded sample, pass through the focussing elements, and reach the surface, where they remove surface atoms by means of momentum-transfer. The bias voltage at the HV grid determines the kinetic energy of the argon ions, and the rate of sputtering can be controlled by adjusting the emission current, and monitored by measuring the drain current on the sample, which is in the order of a few μA.

3.4 Low Temperature Scanning Tunnelling Microscope

3.4.1 Scanning Tunnelling Microscope (STM)

The STM used for this work was a commercial unit manufactured by *Omicron GmbH*. The STM is specially designed for low temperature experiments and was therefore calibrated at 5 K, 78 K, and 300 K using Au(111) and Si(111)-7×7 samples [1, 2]. Cooling is achieved by a bath cryostat (liquid nitrogen or helium) attached to it. The STM is also equipped with a direct-current heater, which makes measurements at temperatures between 5 K and 300 K possible.

3.4.2 Noise Reduction

Vibration damping for the STM is achieved by an eddy current damping system. As shown in Figure 3.2, during operation the STM is suspended by three vertical springs so that the copper fins on the periphery of the STM stage are between the fixed magnets. In addition, the whole UHV chamber is supported by rubber feet, which further minimizes noise pick-up from the environment. This, together with the damping system mentioned, provides the STM with very low noise level during operation.

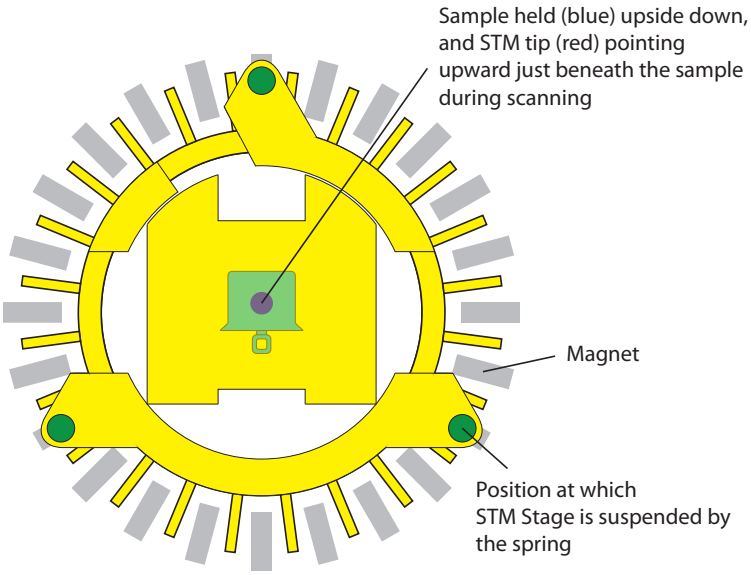

Figure 3.2: A schematic diagram of the STM Stage. Adapted from [3]

3.4.3 Internal Adjustment of the STM Stage

The success of high-resolution STM measurements relies upon the alignment of the STM stage inside the UHV chamber. The STM stage is suspended with three suspension springs. After frequent and prolonged baking and cooling cycles, the length and lateral position of the suspension springs is liable to change, resulting in unsatisfactory alignment of the STM stage. In order to have its best performance, the alignment of the STM stage needs inspection every one or two years.

The adjustment procedure of the STM stage in the LT-STM, which is detailed elsewhere [3], will be briefly described. The lateral adjustment of the STM stage is achieved by turning the inserts (which support the suspension springs) located on top of the LHe cryostat (Figure 3.3). By turning the inserts clockwise/anticlockwise, the suspension springs twist by a very slight amount, which altogether results in lateral movement of the STM stage. Moreover, on the rim of every insert there is a key screw for height adjustment of the suspension springs. Turning the key screw clockwise (anticlockwise) leads to upward (downward) movement of the suspension spring.

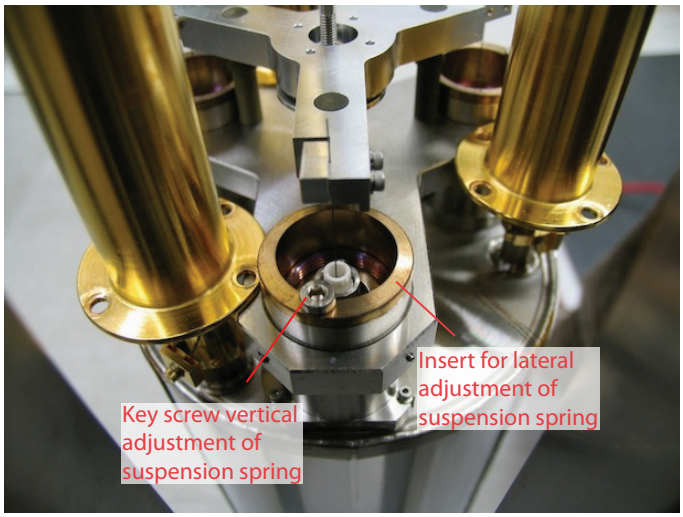

Figure 3.3: A picture of the inserts on top of the LHe cryostat. The inserts, which support the suspension springs, are responsible for the lateral and vertical adjustment of the STM stage.

There are several requirements for the adjustment of the STM stage. Firstly, the vertical positions of the suspension springs need to be adjusted in a way that when suspended, the STM stage is separated evenly from the bottom of the LHe cryostat. Secondly, that the suspension springs do not touch anything around them, and thirdly that the plates from the eddy current system should be centred between the magnets.

For a brand-new instrument, the separation between the bottom of the LHe cryostat and the STM stage should be ∼5 mm, and this should remain the same at different temperatures. However, after prolonged baking procedures, the suspension springs in the LT-STM employed here were discovered to contract by ∼3 mm between 300 K and 78 K. As a re-

sult, the separation distance was adjusted at ∼9 mm at 300 K, and hence contracted ∼5 mm when the STM was cooled to ∼78 K. This adjustment makes the LT-STM working at low noise level in imaging and spectroscopy mode in a temperature range between 300 K and 78 K. The noise level is monitored by fast Fourier Transform (FFT) analysis of the tunnelling current during operation.

3.4.4 Role of Piezoelectric Scanner in STM

During scanning, a tip is scanned across the surface or vice versa. The precise movement of the tip is achieved by piezoelectric tube, tripod, or bimorph scanners [4]. The STM discussed in this thesis employs a single tube three-dimensional scanner designed by Binnig *et al.* [5]. The tube scanner consists of a single tube of piezo-electric material, an outside and an inside electrode. The outside electrode is split into four electrodes of equal area. Movement along the x- and y- direction is achieved by applying a voltage across the outside electrode pairs along the corresponding direction, which leads to bending of the tube towards that direction. Movement along the z-direction is controlled by applying a voltage to the inside electrode, causing an uniform expansion/contraction of the tube.

3.4.5 Scanning Modes of STM

STM can operate in two modes: constant current and constant height mode, with the former one being most widely used. As shown in Figure 3.4, in constant current mode, the tip is positioned at a height above the surface so that the tunnelling current is constant. As the tip is scanned across the surface, it moves up and down in order to maintain the tunnelling current. This height adjustment is controlled by a negative feedback loop mechanism, as shown in Figure 3.5. The vertical movement of the tip with respect to the sample corresponds to either a change in physical distance between them or that in the local-density of states (LDOS) across the surface. By recording the z- movement of the tip at every (x,y) position, a topographical image of the surface can be obtained.

In constant height mode, the tunnelling current is no longer held fixed during scanning. Hence, other than the variation in the tip height, the STM image obtained in this case corresponds to variation in the local-density of state (LDOS) across the surface. However, in constant height mode, a very smooth surface is required in order not to have the tip crash into the surface during scanning.

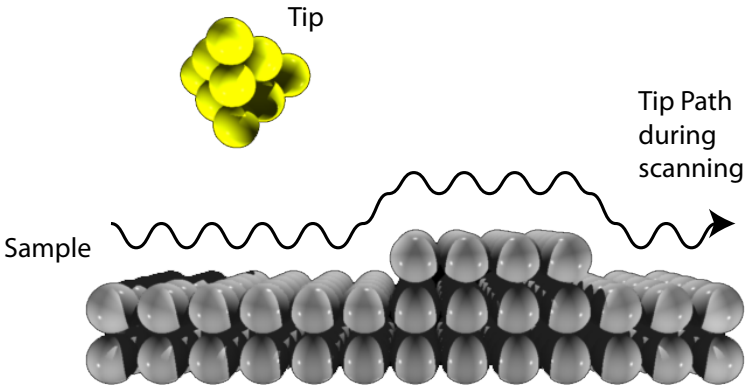

Figure 3.4: An illustration of constant current mode.

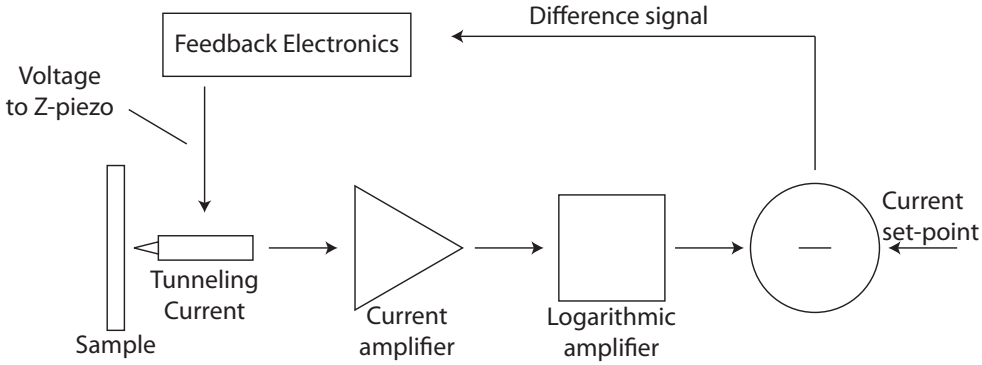

Figure 3.5: Schematic diagram of the feedback mechanism for constant current scanning.

STM tips are the key factor for high-resolution STM scanning. Bad tips like tips without a sharp apex or with multiple apexes result in poor contrast, shadowing, and instability in STM imaging. To achieve atomic resolution in STM, a reliable tip-fabrication method is highly desirable. In ideal cases, a STM tip is terminated with a single, known atom. Up to present, however, no technique can manufacture a STM tip like this. Empirically, macro-

scopically sharp, symmetric tips (as observed from an optical microscope) have proved suitable for STM imaging. Tungsten, due to its hardness, is widely used for tip fabrication.

An electrochemical etching method (Figure 3.6) was employed to prepared STM tips. By means of surface tension, a film of 2 M sodium hydroxide (NaOH) aqueous solution is held within a stainless steel circular ring that acts as the cathode. A tungsten wire, (GoodFellow 99.9%, 0.40 mm *dia*) which is spot-welded onto a tip holder, is held at the centre of the ring and acts as the anode. A bias voltage of 2 V DC is applied between the two electrodes resulting in etching of the wire [6]. Once the tungsten anode is etched to a threshold thickness, the gravitational force elongates the neck leading to fracture and resulting in a sharp tip. The tip is thoroughly rinsed with distilled water, and then introduced into the UHV chamber and degassed at ∼400 K before use.

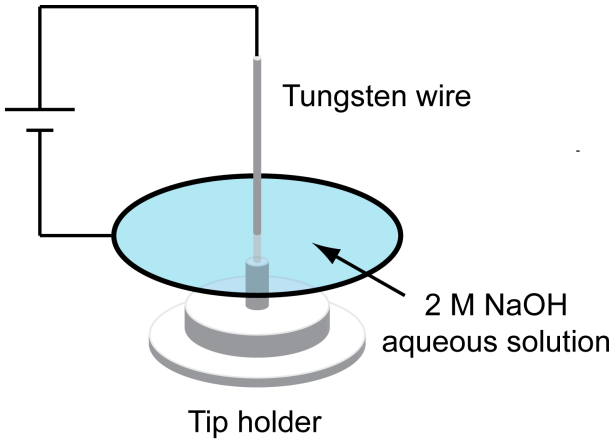

Figure 3.6: A schematic illustration of electrochemical etching.

3.5 LEED Optics

Omicron *GmbH* SPECTALEED optics were employed for low energy electron diffraction (LEED). As shown in Figure 3.7, they comprise an electron gun, and a system suitable for retarding field analysis (RFA), and a fluorescent screen. The electron gun fires a focussed electron beam at energies of 20-200 eV onto the sample surface, with electrons elastically back-scattered from the surface being filtered in the RFA and then directed onto the phosphorescent screen, on which LEED patterns are formed. Provided that the incident electron beam is collimated, the finite size of the LEED spots is governed by the quality of the sample, such as its roughness. The RFA consists of four concentric grids. The first and the last grids are earthed, and the remaining grids are biased at particular potentials at which only elastically back-scattered electrons can travel through the analyzer. This results in the formation of well-defined LEED patterns on the fluorescent screen.

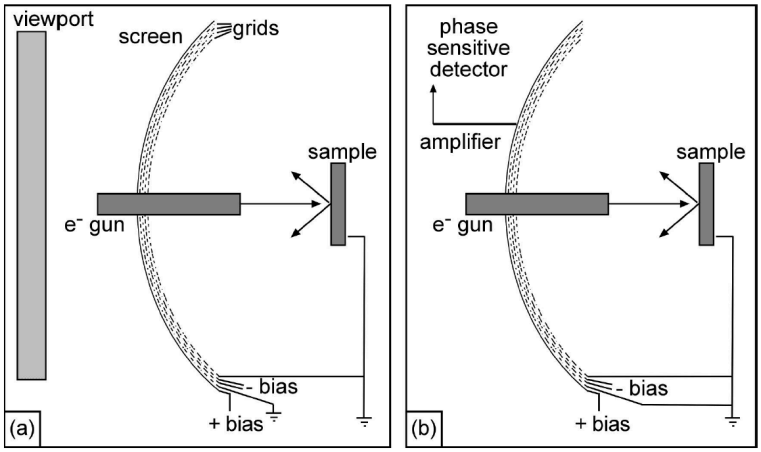

Figure 3.7: (a) Schematic representation of LEED optics. (b) Schematic diagram showing that the LEED optics can also operate in retarding field analyzer Auger mode.

3.6 X-Ray Source

XPS measurements employed a dual-mode X-ray source manufactured by VSW Atomtech Ltd (Figure 3.8). In the X-ray source, a tapered anode has two faces, on which films of Al and Mg are coated respectively. Each anode face comes with its own filament. To generate characteristic X-ray lines, a current is applied across the earthed filament with the anode face biased at high voltage (typically 10 kV). This leads to electrons coming out from the filament bombarding the anode face, on which soft X-rays are produced. The X-rays then pass through an aperture in the surrounding cylindrical shield, covered with a thin sheet of Al foil, which is used to screen the sample from stray electrons, heating effects, and any contaminants originating from the source. Running with the anode face coated with Al (Mg), the X-rays source generates the Al Kα (Mg Kα) line at 1486.6 eV (1253.6 eV). Due to its compact design, efficient water-cooling is required for operating the X-ray source; otherwise, overheating might occur, leading to intermixing of atoms between the anodes, and resulting in features in spectra arising from dual excitation.

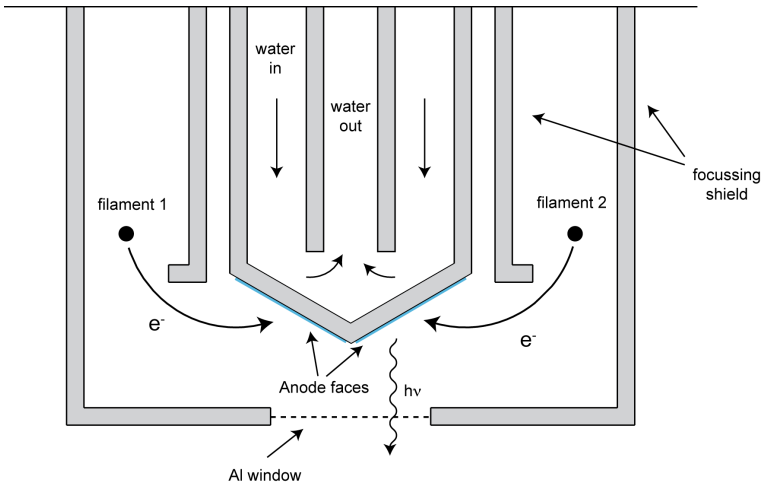

Figure 3.8: Schematic diagram of a dual-mode X-ray source [7].

3.7 UV Source

A VG Microtech UV lamp was employed for ultraviolet photoemission spectroscopy measurements (UPS). The UV lamp (Figure 3.9) comprises a gas discharge region, and a long capillary. To generate UV light, high-purity noble gas like He, Ne, Ar is leaked into the discharge region, across which a high voltage bias is applied. The gaseous atoms are ionized in the electric field, and the ionized gas emits photons of characteristic energies, depending on the type gas used. With the use of He, the UV lamp generates a He I line at 21.2 eV and a He II line at 40.8 eV. The light produced in the discharge region is then guided through a bore (diameter ∼1 mm) along the capillary tube onto the sample. To maintain UHV conditions inside the experiment chamber, the gas discharge region in the UV lamp is differentially pumped by a turbo-molecular pump and a rotary pump during operation.

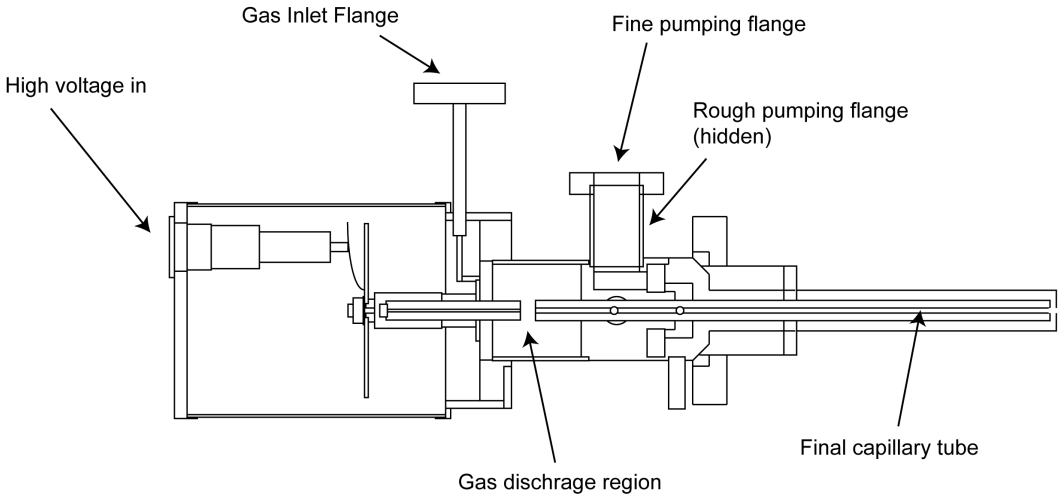

Figure 3.9: Schematic diagram of the VG Microtech UV lamp. Adapted from [8]

3.8 Synchrotron Radiation using Beam-line I311 at Max-Lab

Synchrotron radiation has a number of advantages over conventional X-ray sources, such as high incident flux, high energy resolution, well-defined polarisation, and tuneable photon energy. The high-resolution photoemission and photo-absorption experiments reported in Chapter 5 employed beamline I311 at Max-Lab II [9] in the University of Lund, Sweden. This beamline uses undulator-generated radiation in the energy range of 30-1500 eV. As shown in its schematic layout in figure 3.10, this beamline consists of a pre-focusing mirror, a monochromator, a re-focusing mirror and an end station. The 900 mm long pre-focusing mirror intercepts the horizontally diverging (3 mrad) radiation from the undulator and focuses it in the horizontal direction. The monochromator is a modified SX-700 with a 1200 $\text{l}\cdot\text{mm}^{-1}$ grating, a spherical focusing mirror and a moveable exit slit. The resolving power of the monochromator $E/\Delta E$ is $5 \times 10^3 - 2 \times 10^4$. The area of the focused photon beam is 0.3(vertical) $\times$ 1.0(horizontal) mm^2, with a photon current of $(5 - 10) \times 10^{10}$ photons$\cdot\text{s}^{-1}$ [10]. The re-focusing mirror re-focuses the monochromatic beam onto the sample position located in the end station.

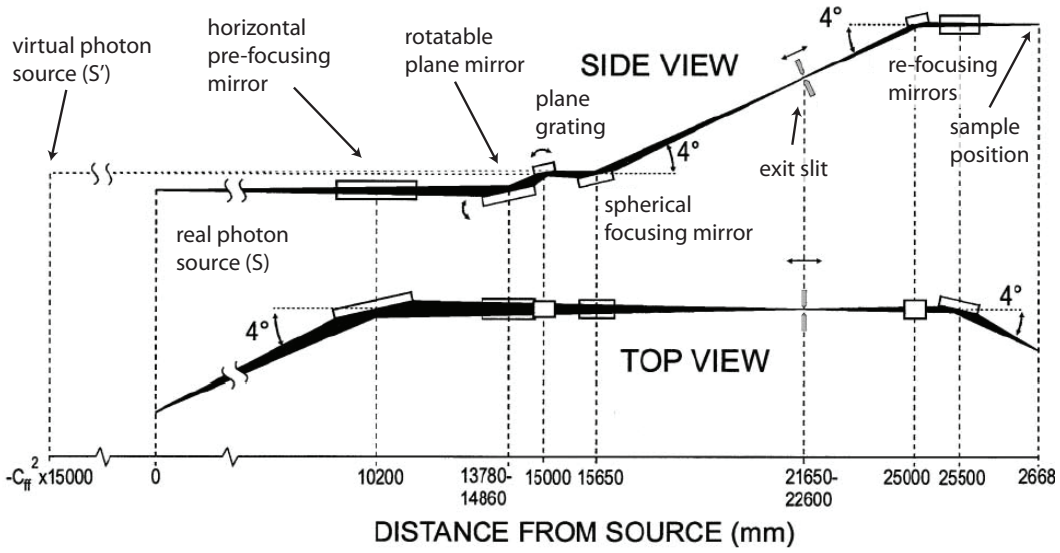

Figure 3.10: Schematic layout of the I311 beamline at Max-Lab II.

As shown in figure 3.11, the end station consists of separate analysis and preparation chambers mounted vertically, both of which are accessible via a long Onimax manipulator. The preparation chamber is equipped with standard sample preparation facilities, as well as LEED, and is connected to the inlet gas system which can provide up to four different gases. The analysis chamber is equipped with a hemispherical SCIENTA-SES200 electron energy analyzer, which is angled 55° away from the incoming photon beam. The photon beam on the sample is *p*-polarised.

The high-resolution XPS experiments reported in Chapter 5 were performed at normal emission. For the carbon K-edge Near-Edge X-ray Absorption Fine Structure (NEXAFS) measurements of CO on the $Pd/TiO_2(110)$ surface, the energy analyzer was run at constant final state (CFS) mode, in which its energy window was centred at the peak of the C KLL Auger transition yield (265 eV) while the photon energy was ramped between 280 eV and 320 eV. The NEXAFS measurement was carried out at different incident angles before and after CO adsorption. In this manner, the bonding angle of CO on the $Pd/TiO_2(110)$ surface can be determined.

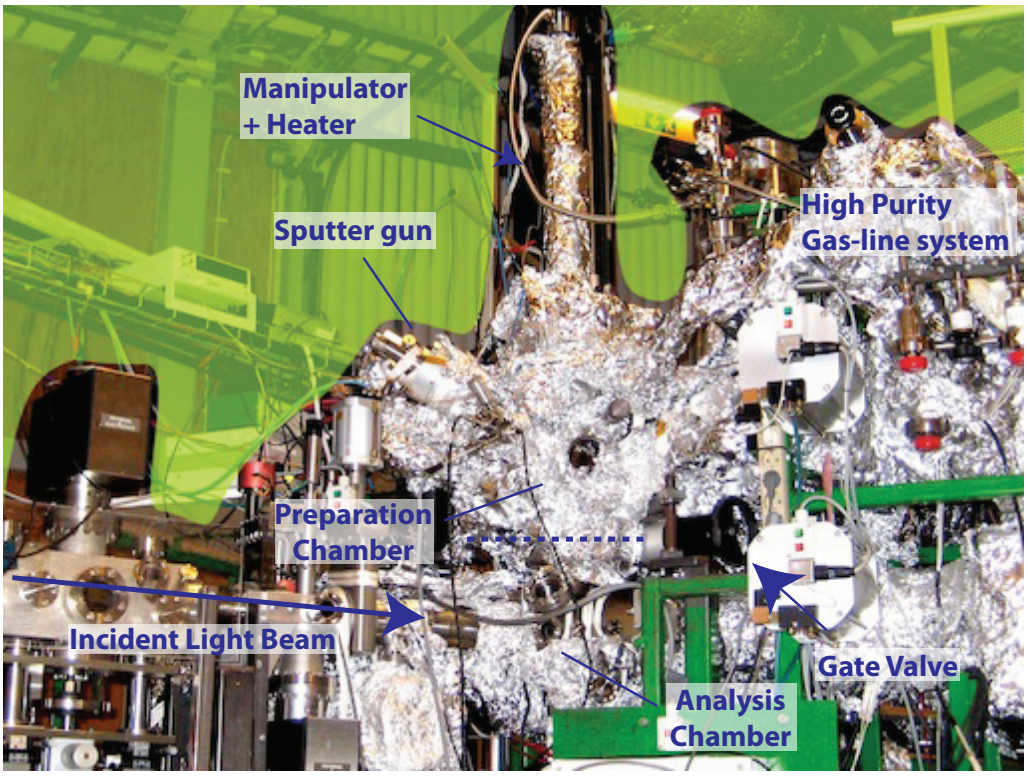

Figure 3.11: A picture of the end station of Beam-line I311.

References

[1] V. M. Hallmark, S. Chiang, J. F. Rabolt, J. D. Swalen and R. J. Wilson, *Phys Rev Lett*, 1987, **59**, 2879–2882.

[2] R. S. Becker, J. A. Golovchenko, E. G. Mcrae and B. S. Swartzentruber, *Phys Rev Lett*, 1985, **55**, 2028–2031.

[3] O. GmbH, *The Low Temperature STM User's Guide*, Limburger Strasse 75, 65232 Taunusstein, Germany, 1st edn., 2002.

[4] R. Wiesendanger, *Scanning Probe Microscopy and Spectroscopy*, Cambridge University Press, Cambridge, UK, 1994.

[5] G. Binnig and D. P. E. Smith, *Review of Scientific Instruments*, 1986, **57**, 1688 –1689.

[6] I. Ekvall, E. Wahlstrom, D. Claesson, H. Olin and E. Olsson, *Meas Sci Technol*, 1999, **10**, 11–18.

[7] *Practical Surface Analysis*, ed. D. Briggs and M. P. Seah, John Wiley and Sons Ltd, England, 2nd edn., 1990, vol. 1.

[8] V. Microtech, *Ultraviolet Sources Operating Manual*, West Sussex, UK, 4th edn., 1999.

[9] R. Nyholm, J. N. Andersen, U. Johansson, B. N. Jensen and I. Lindau, *Nucl Instrum Meth A*, 2001, **467**, 520–524.

[10] J. Weissenrieder, A. Mikkelsen, J. N. Andersen, P. J. Feibelman and G. Held, *Phys. Rev. Lett.*, 2004, **93**, 196102.

Chapter 4

Oxygen Vacancy Origin of the Surface Band Gap State of Rutile TiO_2(110)

Abstract

Scanning tunneling microscopy and photoemission spectroscopy have been used to determine the origin of the band-gap state in rutile TiO_2(110). This state has long been attributed to oxygen vacancies (O_b vac). However, recently an alternative origin has been suggested, namely, subsurface interstitial Ti species. Here, we use electron bombardment to vary the O_b vac density while monitoring the band-gap state with photoemission spectroscopy. Our results show that O_b vac make the dominant contribution to the photoemission peak and that its magnitude is directly proportional to the O_b vac density.

4.1 Motivations

Metal oxides play an important role in a number of technologies such as catalysis, light harvesting, and gas sensing [1]. Surface oxygen vacancies have long been thought to dominate the reactivity of oxide surfaces and therefore much research is directed towards understanding such defects. Rutile titania, particularly its most stable (110) face, has been used extensively as a model substrate to explore the surface physics and chemistry of metal oxides in general [2, 3].

The TiO_2(110) surface is composed of alternating [001]-direction rows of fivefold coordinated Ti^{4+} ions (Ti_{5c}) and twofold coordinated bridging O^{2-} ions (O_b). Rutile TiO_2 is a wide band-gap insulator ($\sim$3 eV) which can be made semiconducting upon reduction by ion sputtering and annealing. This sample preparation results in the creation of oxygen vacancies, including bridging O vacancies (O_b vac) at the surface (Figure 4.1), and interstitial Ti species [2, 4, 5]. For such surfaces, a band-gap state is found about 1 eV below the Fermi level (E_F) in ultraviolet photoemission spectroscopy (UPS) [6, 7] and as a $\sim$1 eV loss in electron energy loss spectroscopy (EELS) [8]. This state has been determined to have Ti *3d* character by resonant photoemission studies [7, 9].

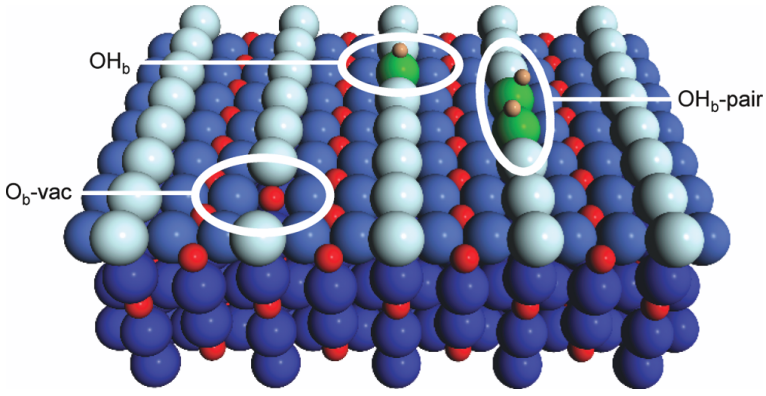

Figure 4.1: A ball model of TiO_2. Small, red spheres denote fivefold coordinated Ti (Ti_{5c}) ions. Large, blue spheres represent O ions with twofold coordinated bridging O atoms shaded lighter. An oxygen vacancy (O_b vac), an individual hydroxyl (OH_b), and a pair of hydroxyl species (OH_b pair) are shown.

Exposing the surface to O_2 eliminates the band-gap state so it was concluded that the

state originates from O_b vac that are themselves filled by oxygen atoms upon exposure to O_2 [7]. Thus, when O_b vac are formed on the TiO_2 surface, two excess electrons associated with each O_b vac are thought to transfer to the empty *3d* orbitals of the neighbouring Ti_{5c} ions, forming two Ti^{3+} sites [6]. This picture, proposed by Henrich and co-workers based on the creation of band-gap states by argon ion bombardment [6], is known as the O-vacancy model.

Water is also known to fill the O_b vac on TiO_2 from a temperature above 187 K, in this case replacing them with two hydroxyl species (OH_b) [10–12]. The process of water splitting on a O_b vac site is illustrated in figure 4.2. However, exposing the surface to water does not have a substantial effect on the magnitude of the band-gap state [7, 13]. Hence, under the O-vacancy model, the band-gap state should be present when either O_b vac or OH_b are present at the surface.

While this O-vacancy model has been widely accepted, Wendt *et al.* [14] recently proposed an intriguing alternative origin of the band-gap state. They found that when dosing O_2 onto a hydroxylated TiO_2 surface, the OH_b were apparently eliminated but the band-gap state still persisted. From this, it was concluded that O_b vac cannot be the main origin of the band-gap state. Instead, it was suggested that interstitial Ti atoms make the dominant contribution to the band-gap state. Accompanying density functional theory (DFT) calculations indicate that interstitial Ti can indeed lead to band-gap states and that O_b vac do not lead to such states.

Overall, however, the theoretical picture regarding the origin on the band-gap state is not clear. A number of calculations do predict that O_b vac should lead to the formation of the band-gap state observed in photoemission [15–18] such as the recent spin-polarized hybrid DFT calculation by Di Valentin *et al.* [15]. Here, they also demonstrated that the BGS are not removed upon dissociation of a water molecule and formation of a pair of OH groups. In other words, both the vacancy and OHb_b give rise to localized Ti^{3+} $3d^1$ states about 1 eV below the conduction band (CB). Papageorgiou *et al.* [18] modelled

the electronic structure of O_b vac and OH_b in the presence of different amounts of extra electronic charge. They found that changing the number of extra electrons occupying the BGS only affects the spatial distribution of the associated 3d electronic density, with the energy of the BGS still remaining close to 1 eV below the CB onset. However, a recent spin-polarized hybrid DFT calculation also suggests that Ti^{3+} interstitials can contribute to the band-gap state [19].

It seems reasonable that both O_b vac and Ti interstitials can give rise to the BGS as they both donate electronic charges into Ti 3d states. When the O_b vac reacts with molecular oxygen, the vacancy is filled and because of its electronegativity, the oxygen extracts the excess charge from the vacancy. However, when the O_b vac is filled with water, the resulting OH_b species are not electronegative enough to remove this charge. As such, the electronic charge can still be detected as the BGS.

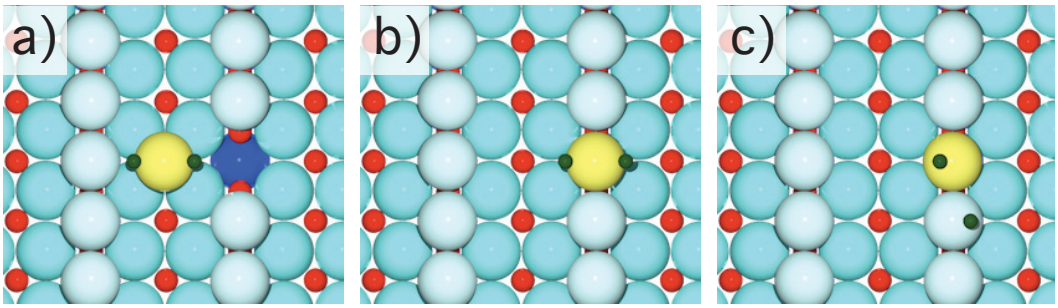

Figure 4.2: A sequence of ball-model pictures showing dissociative adsorption of a H_2O molecule on a O_b vac site. (a) The H_2O molecule physisorbs on the Ti_{5c} atom next to the O_b vac. (b). The H_2O molecule hops onto the O_b vac. (c) One of the H atom on the H_2O molecule is transferred to the neighbouring O_b, leading to the formation of a hydroxyl (OH_b)pair.

We resolve this issue experimentally by monitoring the band-gap state as a function of the O_b vac density. The O_b vac concentration was varied by bombarding the TiO_2 surface with low energy electrons [20]. By preparing the surface in this way rather than by thermal annealing, the number of interstitial Ti in the near-surface region is kept constant [21]. The O_b vac concentration is determined from STM analysis of the surface before and after the UPS measurement, which is carried out in the same instrument. Our results show that there is a direct correlation between the concentration of O_b vac and the intensity of the photoemission band-gap state, thus providing direct evidence for the oxygen vacancy

model.

4.2 Experimental Section

The STM measurements were performed at ∼78 K in a bath cryostat Omicron STM housed in an ultrahigh vacuum chamber with a base pressure of 2×10^{-11} mbar. The He I ($h\nu$ = 21.2 eV) UPS data were measured in an adjoining preparation chamber (base pressure of 1×10^{-10} mbar) with a VSW HA125 hemispherical energy analyser and a five-channel electron multiplier array. Normal emission UPS spectra were recorded at an incidence angle of 45° with respect to the surface normal. E_F was determined from the tantalum sample holder which was in electrical contact with the sample. The preparation chamber was also equipped with facilities for x-ray photoemission spectroscopy (XPS) and low energy electron diffraction (LEED), which were used to confirm the sample cleanliness and long-range order.

Samples were prepared initially by cycles of argon ion sputtering and annealing to ∼1000 K. Electron bombardment experiments employed a negatively biased filament (75 eV) with the sample grounded [20]. To minimise water contamination from the residual vacuum during the UPS measurement, the sample was held at ∼500 K which prevents water adsorption [4]. We checked that holding the substrate at this temperature does not affect the O_b vac density, as measured by STM, or change the magnitude of the UPS band-gap state peak. Static secondary ion mass spectroscopy shows that the Ti:O ratio in the selvedge is essentially invariant between 400 and 700 K [5]. Hence, the concentration of interstitial Ti will not change over the course of the UPS measurements.

4.3 Results and Discussions

Figure 4.3(a) shows the STM image of an as-prepared TiO_2 surface (r-TiO_2) collected using a light blue TiO_2 crystal (the colour indicating a lightly reduced crystal [22]). The bright rows in the STM image arise from Ti5c rows whereas the dark rows correspond to O_b rows [2]. Point defects such as O_b vac and single and paired surface hydroxyls (OH_b) appear as bright spots between the bright rows, O_b vac being slightly darker than OH_b, which are themselves darker than the OH_b pairs. TiO_2 almost always contains surface hydroxyls formed by water dissociation at O_b vac sites. Hence, when counting the number of O_b vac present at the surface, we also count every two isolating OH_b as a single O_b vac and every OH_b-pair as a single O_b vac. In this way, we have calculated the initial density of O_b vac on the as-prepared surface to be 4.3 ± 0.6 % ML, where 1 ML (monolayer) is defined as the density of (1×1) unit cells, 5.2×10^{14} cm^{-2}. The coverage here, and throughout this study, was determined from five separate 250×250 $Å^2$ STM images collected from macroscopically different parts of the surface.

Figure 4.3(b)-(d) show the STM images of the r-TiO_2 surface after it was bombarded with 75 eV electrons for different durations. The current density at the surface was estimated to be ∼0.2 mA/cm^2. After electron bombardment, the O_b vac density increases. The densities of O_b vac on the TiO_2 surfaces after electron bombardment are 8.0 ± 0.2% ML for 5 s, 9.6 ± 0.5% ML for 10 s, 9.2 ± 0.2% ML for 20 s. It should be noted that the surfaces following electron bombardment for 10 and 20 s have similar O_b vac densities. However, the surface that has been exposed for 20 s is also decorated with pitlike features [19]. These features have a density of 0.15 ± 0.06% ML, about 100 times lower than the O_b vac density and we assume they do not have a substantial effect on the band-gap state.

UPS was employed to monitor the band-gap state during the experiment. Figure 4.3(e) shows spectra corresponding to r-TiO_2 before and after electron bombardment. The spectrum of r-TiO_2 (red) is similar to that reported previously [22]. The main peak at ∼5.5 eV and the shoulder at ∼7.0 eV below E_{textF} are mainly O *2p* derived [23]. Electron bombardment causes the O *2p* band to shift away from E_{textF} due to band-bending, with

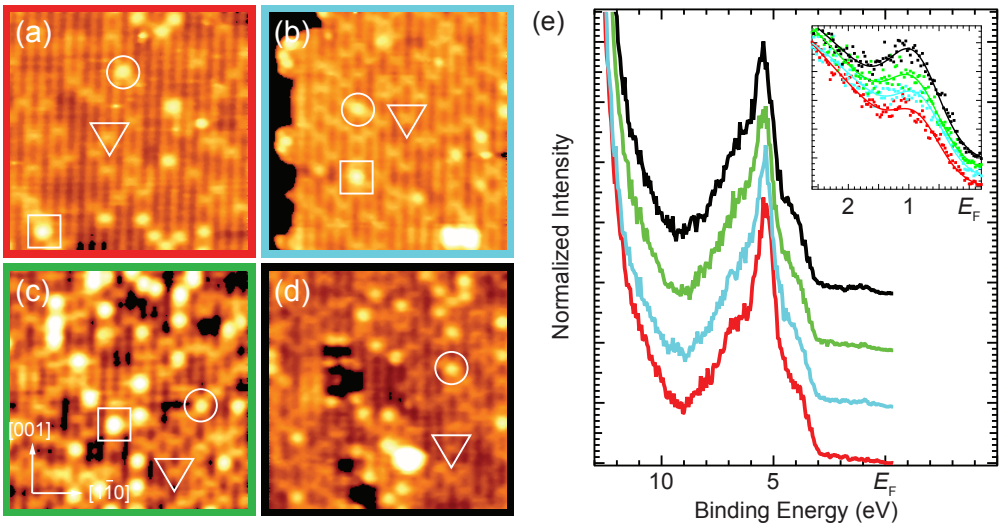

Figure 4.3: STM images (125×125 Å^2) of (a) the as-prepared TiO_2(110) surface (r-TiO_2) and its appearance following electron bombardment (kinetic energy ∼75 eV, ∼1 mA) for (b) 5, (c) 10, (d) 20 s. Symbols indicate O vacancies (triangle), bridging hydroxyls (circles), and hydroxyl pairs (square). STM images were collected with a tunnelling current ≤ 0.2 nA and a sample bias voltage of 1.3 V. (e) Corresponding UPS He I spectra of as-prepared r-TiO_2 (red) and after electron bombardment for 5 (light blue), 10 (green), and 20 s (black), all recorded under identical conditions. The inset in (e) shows the band-gap state region in more detail. The data points are shown as squares and the curves are best fit to a Gaussian and polynomial background. The spectra are vertically offset for clarity. The spectra in (e) corresponding to each surface are color-coded with the color borders in (a)-(d). STM images and UPS spectra were collected at ∼78 K and ∼500 K, respectively.

the extent of the shift increasing with the duration of electron bombardment. The inset of 4.3(e) shows the UPS spectra measured across the band-gap state region (from 2.5 eV to E_F). The Ti *3d* derived band-gap state (located 0.9 eV below E_F) is clearly present in the spectrum of r-TiO_2. The intensity of this peak also clearly increases following electron bombardment.

We also collected data on an as-prepared surface of a dark blue TiO_2 crystal, the dark blue colour indicating a more reduced crystal [22]. The STM image in Figure 4.4(b) shows that the surface from the dark blue crystal contains a greater density of O_b vac than the light blue sample, as one would expect. The O_b vac density on the dark blue crystal is $6.7 \pm 0.8\%$ ML compared to $4.3 \pm 0.6\%$ ML for the light blue sample. As for UPS, the spectrum recorded from the dark blue crystal has a more intense band-gap state peak than in the case of the light blue sample. The area of the band-gap state peak for both

samples, including the electron-bombarded surfaces, is plotted against the O_b vac density in Figure 4.5(a). The graph fits easily to a straight line, clearly indicating that the peak area is in direct proportion to the O_b vac density. Thus, it is clear that the population of the band-gap state depends directly on the concentration of O_b vac.

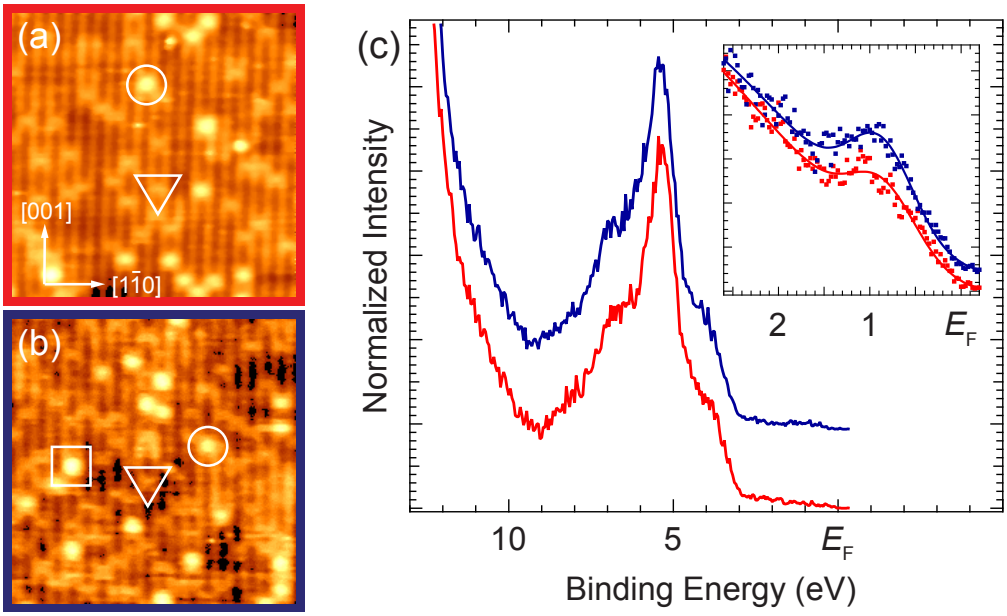

Figure 4.4: STM images (125×125 Å^2) of the as-prepared TiO_2(110) surface (r-TiO_2) of (a) a less-reduced (light blue) and (b) a more-reduced (dark blue) sample, collected with a tunnelling current $\leq$ 0.2 nA and a sample bias voltage of 1.3 V. Symbols indicate O_b vac (triangle), OH_b (circles), and a OH_b pair (square). (c) Corresponding UPS He I UPS spectra taken on the less-reduced (red spectrum) and more-reduced (blue spectrum) TiO_2(110) surface. The inset shows the band-gap state region in more detail, with the more reduced surface exhibiting a larger band-gap state peak in the spectra. The data points are shown as squares and the curves are best fit to a Gaussian and polynomial background. The spectra are vertically offset for clarity. The spectra in (c) corresponding to each surface are color-coded with the color borders in (a)-(b).

As we have already discussed above, O_b vac on r-TiO_2 react with water molecules above 187 K [3], forming two OH_b for each O_b vac site. The OH_b density is therefore highly correlated with the underlying O_b vac density but does not have any direct relationship with the interstitial Ti density. Thus, if the band-gap state originates from O_b vac, then the intensity of the peak in UPS should scale with the OH_b density as well as the O_b vac density.

We exposed a hydroxylated dark-blue TiO_2(110) surface (h-TiO_2) to 10 Langmuirs (L)

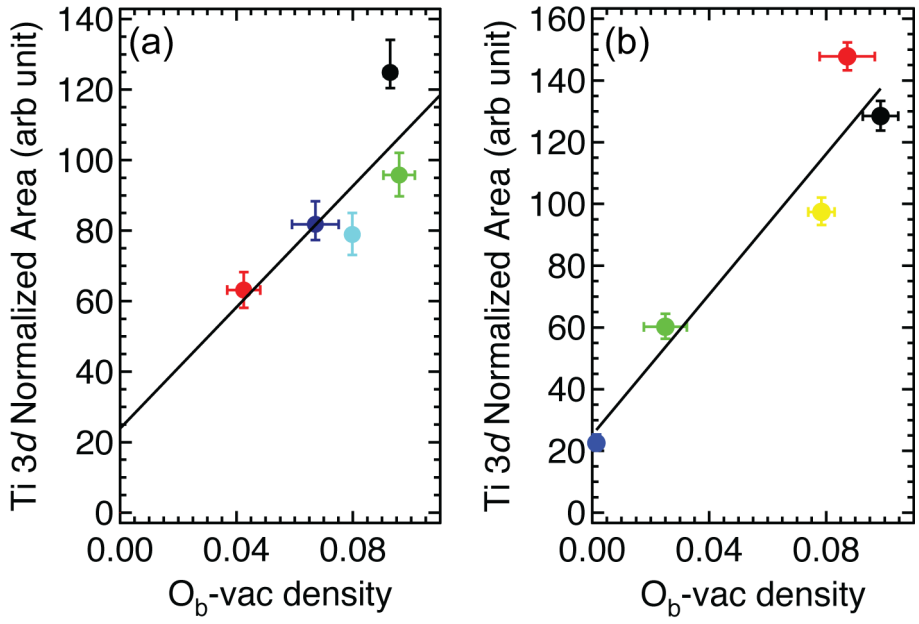

Figure 4.5: Normalized integrated intensities of the band-gap state UPS peaks as a function of O_b vac on the TiO_2 surface determined from STM. To determine the area of the band-gap state peak in each spectrum, the secondary electron background was fitted with a fourth-order polynomial while the band-gap state peak (located at ~0.9 eV) below E_F) was fitted with a Gaussian function from which the normalized integrated intensity of the peak was extracted. (a) Data taken from experiments on as-prepared TiO_2. The data points are color-coded with the color borders in Figure 4.3 and Figure 4.4. (b) Data taken from experiments on hydroxylated TiO_2 (h-TiO_2) (in the case, the O_b vac intensity plotted is that before hydroxylation). The data points are color-coded with the color borders in Figure 4.6.

of O_2 at ~300 K, where 1 L corresponds to an exposure of 1.33×10^{-6} mbar.s. The STM image in Figure 4.6(b) shows that the STM features corresponding to OH_b are eliminated upon oxidation and replaced with features that appear on top of the bright Ti_{5c} rows in the STM images. These features have previously been assigned to a mixture of oxygen adatoms, surface hydroxyls, and O_2H species (i.e. O_xH_y where x = 1, 2 and y = 0, 1) [12, 24]. The important point here is that our UPS measurements indicate that the band-gap state is largely quenched during this oxidation process, the corresponding peak having only 15% of its original intensity, as shown in Figure 4.6(f). It is noted that the UPS measurements are in this case performed at ~300 K instead of ~500 K to avoid the formation of TiO_x species on the oxygen-rich TiO_2 surface [14].

This oxidized surface (o-TiO_2) was subjected to electron bombardment for durations of 2 s, 5 s, and 10 s. The O_xH_y species are nearly all removed after electron bombardment

for 2 s and are entirely removed after 5 s. More importantly, the STM images in Figure 4.6(c)-(e) show that the OH_b that were eliminated upon oxidation are replenished after electron bombardment (to be precise, electron bombardment leads to the formation of O_b vac, each of which is converted to two OH_b by exposure to water in the residual vacuum [10–12]). The density of OH_b created in this way increases with the duration of electron bombardment, as one would expect.

The corresponding UPS spectra show that the band-gap state, which is quenched significantly by exposure to O_2, reappears after electron bombardment. Furthermore, the magnitude of the band-gap state peak very clearly increases with the duration of electron bombardment. Figure 4.5(b) shows a plot of the intensity of the band-gap state peak in UPS against the initial O_b vac concentration (which is calculated by considering that every two OH_b species originates from one initial O_b vac). Again, the peak area is directly proportional to the initial O_b vac density. This, together with the graph in Figure 4.5(a), shows in a very clear way that the population of the band-gap state depends directly on the concentration of O_b vac.

Examination of the graphs in Figure 4.5, however, reveals that the population of the band-gap state does not depend only on the O_b vac density. The best-fit lines in both of the graphs in Figure 4.5 do not pass through the origin. This indicates a small, but finite, band-gap state peak in UPS even when no O_b-vac or OH_b are present. The residual intensity of the band-gap state peak is also apparent in Fig. 4.6: exposure of *h*-TiO_2 to 10 L O_2 at room temperature removes virtually all OH_b (only $\sim$0.14% of the OH_b present prior to O_2 exposure remain). However, after this O_2 exposure, the band-gap state peak in UPS still retains $\sim$15% of its intensity prior to this O_2 exposure. This indicates that although the major component to the band-gap state originates from O_b vac, there is a minority contribution that comes from some other defect, unconnected to O_b vac, such as interstitial Ti or sub-surface oxygen vacancies.

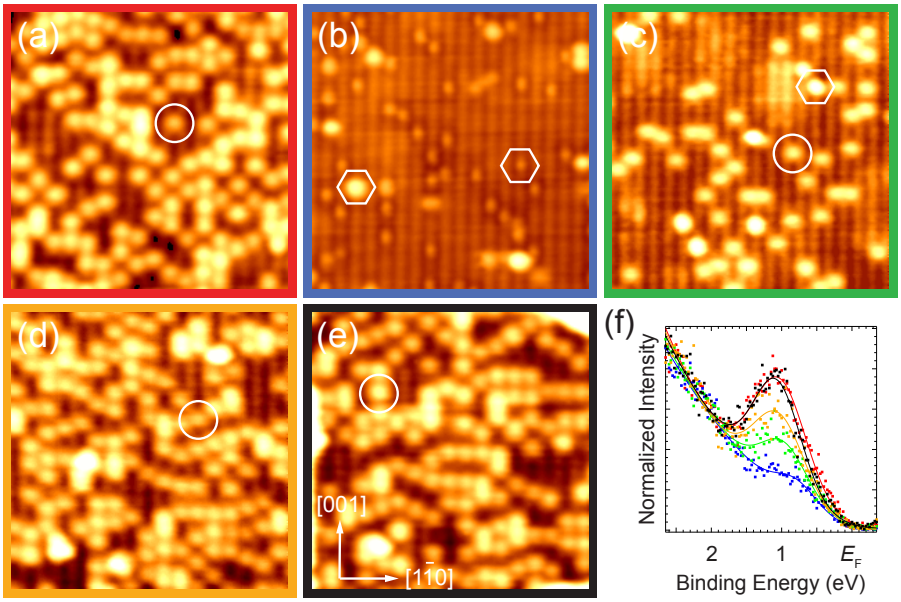

Figure 4.6: STM images (125×125 Å^2) of (a) the hydroxylated TiO_2(110) (h-TiO_2), (b) the oxidized TiO_2 (o-TiO_2) surface and (c)-(e) the surface in (b) following electron bombardment (75 eV) for 2, 5 and 10 s, respectively. Symbols indicate OH_b (circles) and O_xH_y (hexagons). (f) Corresponding UPS He I spectra recorded at 300 K of h-TiO_2 (red), o-TiO_2 (blue), and o-TiO_2 following electron bombardment for 2 (green), 5 (orange) and 10 s (black), all recorded under identical conditions. Only the region near the band-gap state (0.9 eV below E_F) is shown in the spectra.

4.4 Summary

In summary, we have used ultraviolet photoemission spectroscopy in combination with scanning tunnelling microscopy to establish that the band-gap state in TiO_2 originates mainly from bridging oxygen vacancies. Our results also show that the population of the band-gap state increases in direct proportion with the density of O_b vac. This is indirect contrast to a recent study which proposed that interstitial Ti make the dominant contribution to the band-gap state [14].

References

[1] S. D. Jackson and J. S. J. Hargreaves, *Metal Oxide Catalysis*, Wiley-VCH, Weinheim, 2008.

[2] U. Diebold, *Surf Sci Rep*, 2003, **48**, 53–229.

[3] C. L. Pang, R. Lindsay and G. Thornton, *Chem Soc Rev*, 2008, **37**, 2328–2353.

[4] M. A. Henderson, *Langmuir*, 1996, **12**, 5093–5098.

[5] M. A. Henderson, *Surf Sci*, 1999, **419**, 174–187.

[6] V. E. Henrich, G. Dresselhaus and H. J. Zeiger, *Phys Rev Lett*, 1976, **36**, 1335–1339.

[7] R. L. Kurtz, R. Stockbauer, T. E. Madey, E. Roman and J. L. deSegovia, *Surf Sci*, 1989, **218**, 178–200.

[8] W. S. Epling, C. H. F. Peden, M. A. Henderson and U. Diebold, *Surf Sci*, 1998, **412-13**, 333–343.

[9] Z. M. Zhang, S. P. Jeng and V. E. Henrich, *Phys Rev B*, 1991, **43**, 12004–12011.

[10] Z. Zhang, O. Bondarchuk, B. D. Kay, J. M. White and Z. Dohnalek, *J Phys Chem B*, 2006, **110**, 21840–21845.

[11] O. Bikondoa, C. L. Pang, R. Ithnin, C. A. Muryn, H. Onishi and G. Thornton, *Nat Mater*, 2006, **5**, 189–192.

[12] S. Wendt, R. Schaub, J. Matthiesen, E. K. Vestergaard, E. Wahlstrom, M. D. Rasmussen, P. Thostrup, L. M. Molina, E. Laegsgaard, I. Stensgaard, B. Hammer and F. Besenbacher, *Surf Sci*, 2005, **598**, 226–245.

[13] M. A. Henderson, W. S. Epling, C. H. F. Peden and C. L. Perkins, *J Phys Chem B*, 2003, **107**, 534–545.

[14] S. Wendt, P. T. Sprunger, E. Lira, G. K. H. Madsen, Z. Li, J. O. Hansen, J. Matthiesen, A. Blekinge-Rasmussen, E. Laegsgaard, B. Hammer and F. Besenbacher, *Science*, 2008, **320**, 1755–1759.

[15] C. D. Valentin, G. Pacchioni and A. Selloni, *Phys Rev Lett*, 2006, **97**, 166803.

[16] C. J. Calzado, N. C. Hernandez and J. F. Sanz, *Phys Rev B*, 2008, **77**, 045118.

[17] B. J. Morgan and G. W. Watson, *Surf Sci*, 2007, **601**, 5034–5041.

[18] A. C. Papageorgiou, N. S. Beglitis, C. L. Pang, G. Teobaldi, G. Cabailh, Q. Chen, A. J. Fisher, W. A. Hofer and G. Thornton, *P Natl Acad Sci Usa*, 2010, **107**, 2391–2396.

[19] E. Finazzi, C. D. Valentin and G. Pacchioni, *J Phys Chem C*, 2009, **113**, 3382–3385.

[20] C. L. Pang, O. Bikondoa, D. S. Humphrey, A. C. Papageorgopoulos, G. Cabailh, R. Ithnin, Q. Chen, C. A. Muryn, H. Onishi and G. Thornton, *Nanotechnology*, 2006, **17**, 5397–5405.

[21] N. G. Petrik, Z. Zhang, Y. Du, Z. Dohnalek, I. Lyubinetsky and G. A. Kimmel, *J Phys Chem C*, 2009, **113**, 12407–12411.

[22] M. Li, W. Hebenstreit, U. Diebold, A. M. Tyryshkin, M. K. Bowman, G. G. Dunham and M. A. Henderson, *J Phys Chem B*, 2000, **104**, 4944–4950.

[23] T. Minato, T. Susaki, S. Shiraki, H. S. Kato, M. Kawai and K.-I. Aika, *Surf Sci*, 2004, **566**, 1012–1017.

[24] Y. Du, N. A. Deskins, Z. Zhang, Z. Dohnalek, M. Dupuis and I. Lyubinetsky, *J Phys Chem C*, 2009, **113**, 666–671.

Chapter 5

Synchrotron Radiation and STM Studies of CO Adsorption on the $Pd/TiO_2(110)$ Surface

Abstract

The growth of Pd islands on rutile $TiO_2(110)$-(1×1) and CO adsorption on top of those islands were investigated using synchrotron light spectroscopies and scanning tunnelling microscopy. The Pd islands, which were grown by physical vapour deposition (PVD) of Pd onto the $TiO_2(110)$ surface at ∼800 K, had a pseudo-hexagonal shape, with an average diameter of 30 nm and height of 5 nm, and were not encapsulated with Ti^{n+}(n<4) species from the substrate. After saturation of the Pd/TiO_2 surface with CO, we found that CO molecules bond vertically and form various ordered overlayers on top of the Pd(111) islands, suggesting that the Pd islands possess similar physical properties to Pd(111) single crystals.

5.1 Motivation

The study of metal nanoparticles on oxide supports has received considerable attention, for reasons both practical and fundamental. On the practical side, the heterogenous catalysts used in industrial applications usually consist of nanometre-sized metal particles distributed on an oxide support. In order to improve their performance, a better understanding of their properties are necessary, one method of achieving this is by investigating appropriate model catalysts. On the fundamental side, nanometre-sized metal particles have been shown to exhibit properties deviating from their corresponding single crystal surfaces. These differences have been shown to relate to the unique phenomena occurring in those systems such as kinetic interplay between facets [1], spillover of adsorbates between metal particles and supports [2], and the strong-metal-support-interaction (SMSI) [3].

Among different metal/oxide systems, the motivations for studying Pd/TiO_2 are twofold. Firstly, such Pd/TiO_2 systems have been shown to be active for a wide range of reactions including nitrite reduction in drinking water [4], acetylene hydrogenation [5] and NO_x reduction [6]. Secondly, similar to other group VIII metals (Pt and Rh), Pd exhibits a strong metal-support interaction (SMSI) with TiO_2 surfaces that cannot be found in the systems of noble metals (Cu, Ag and Au) on TiO_2 [7–9]. The SMSI effect was first described by Tauster *et al.* in 1978 [3], and has been shown to negatively influence the reaction rate for chemical reactions such as alkane hydrogenolysis [10]. In order to explain the SMSI-induced effects, several models have been proposed, the most widely accepted being charge-transfer and encapsulation [11, 12].

Preparing chemically-active, well-defined Pd nanoparticles on rutile $TiO_2(110)$ is by no means trivial, and this is often hindered by encapsulation. Encapsulation of Pd nanoparticles by the underlying $TiO_2(110)$ substrate starts to take place when the Pd/TiO_2 system is annealled to 800 K [13]. In addition to degrading the chemical reactivity (such as CO uptake) [13, 14], such encapsulation process was also discovered to drastically alter the structure of the Pd islands [15]. A similar encapsulation-induced structural change was

also discovered in the Pt/TiO_2(110) system by Dulub *et al.* [16].

In spite of this, several groups are still devoting themselves to growing chemically-active, well defined Pd nanoparticles on TiO_2. One notable work is by Humphrey *et al.* [17]. Using X-ray Photoemission electron microscopy (X-PEEM) and STM, and by depositing Pd onto the TiO_2(110) substrate at 900 K, they observed two types of Pd nanostructures which formed on the TiO_2(110) surface. These were elongated nano-wires (up to 1000 nm long) and pseudo-hexagonal islands (between 80-160 nm in diameter). Although the authors did not provide evidence showing for or against TiO_x encapsulation of the nano-particles, their work does make us realise that preparing Pd nanoparticles on TiO_2 suitable for the study of catalytic reactions becomes plausible.

A number of attempts have been made to elucidate the properties of well-defined Pd nanoparticles grown on Al_2O_3/NiAl(110) [18]. Those attempts include adsorption of CO [19], NO [20, 21], O_2 [21] and 1,3-Butadiene [22], interaction of H_2 with CO and C_2H_4 [23], as well as other reactions such as the decomposition of NO [24] and CH_3OH [25], and olefin hydrogenation [26]. Indeed, all but one [21] of the studies mentioned above were conducted by spectroscopic methods. Probing the properties of Pd nanoparticles at the atomic level is still lacking.

In this chapter, the growth of Pd nanoparticles on rutile TiO_2 and CO adsorption on the Pd islands have been investigated with synchrotron radiation spectroscopies and STM.

5.2 Experimental

5.2.1 Synchrotron Radiation Work in Max-Lab

The synchrotron radiation spectroscopy measurements were performed using Beamline I311 in Max-Lab II at the University of Lund, Sweden. Its optical set-up has been briefly discussed in Chapter 3 and detailed in Ref [27]. Its end station comprises separate ultra-

high vacuum (UHV) analysis and preparation chambers in a vertical arrangement and separated with a gate-valve. The preparation chamber is equipped with the standard facilities for sample preparation (ion sputter gun, heater) and characterisation of surfaces (LEED optics), and connected to a gas-inlet system which can store up to four types of gases. The analysis chamber is equipped with a SCIENTA-SES200 hemispherical analyser for photo-emission and absorption spectroscopy. The angle between the analyzer and the incoming photon beam is 55°.

The TiO_2(110) sample was prepared by cycles of Argon ion sputtering and annealing to ∼1000 K. The sample temperature was monitored using a K-type thermocouple spot-welded near the edge of the sample. The sample's cleanliness and long range order were verified with XPS and LEED respectively. Pd nano-structures were grown on the TiO_2(110) surface by metal vapour deposition (MVD) with the substrate held at ∼800 K, corresponding to a temperature between the onset of metal ad-atom and metal nano-particle mobility [28]. Pd atoms were evaporated from an Omicron GmbH EFM 3 electron-beam evaporator, which was equipped with a flux monitor to gauge the Pd deposition rate. Pd $3d$ and Ti $2p$ photoemission spectra were recorded to confirm the presence of Pd nanostructures and to check if any encapsulation was taking place on the Pd nanostructures. All XPS spectra were taken at normal emission with photon energy of 620 eV, and pass energy of 20 eV. The binding energies were measured with respect to the Fermi edge (E_F), whose position was determined from the tantalum sample plate in direct electric contact with the sample. LEED was employed to check any long-range order arising from Pd nano-structures. Research-grade CO was dosed by backfilling to the preparation chamber, with its purity verified using a quadruple mass-spectrometer (QMS).

Carbon K-edge NEXAFS (280-320 eV) measurements were carried out to examine the adsorption geometry of CO on the Pd/TiO_2(110) surface. The linear polarisation factor of the photon beam at the C K-edge was estimated to be 0.94. NEXAFS data were recorded with the angle of incidence ranging between $30° \leq \theta \leq 90°$ by monitoring the C KLL Auger transition yield with the SCIENTA-SES200 analyzer. Normalisation of the

NEXAFS spectra involved division of the spectra obtained from the Pd/TiO_2 surface before and after CO exposure

5.2.2 Scanning Tunnelling Microscopy in London

The STM experiments were carried out using an Omicron GmbH low temperature STM housed in a ultra-high vacuum (UHV) analysis chamber with a base pressure of $\sim 2\times10^{-11}$ mbar. Located in the LCN, University College London, its adjoining preparation chamber houses an ion sputter gun, LEED optics, QMS and is connected to a gas-inlet system. It was also equipped with a VG-Microtech UV source (He I), a dual-source X-ray gun, and a VSW HA 125 analyzer combined with a five-channel multiplier array for X-ray/ultraviolet photoelectron spectroscopy.

The $TiO_2(110)$ sample was prepared by cycles of Argon ion sputtering and annealing to ∼1000 K. The sample temperature was monitored with an infra-red pryometer. The sample's cleanliness and long-range order were verified with XPS, LEED and STM. Pd nano-structures were grown on the $TiO_2(110)$ substrate by MVD with the sample held at ∼800 K. The source of Pd was a W filament tightly wrapped with Pd wire, which was resistively heated. The evaporator was calibrated using Pt(111) as substrate before use. Pd $3d$ and Ti $2p$ photoemission spectra were recorded to check the presence of Pd and if encapsulation was taking place. All XPS spectra were recorded with Al Kα ($h\nu = 1486.6$ eV) at normal emission. The pass energy used was 10 eV. LEED was employed to check for the presence of Pd-related diffraction spots. All STM data was recorded at 78 K using electro-chemically etched tungsten tips.

5.3 Results and Discussions

5.3.1 Photoemission and NEXAFS Results in Max-Lab

Pd atoms were deposited onto the TiO_2(110) surface at a sample temperature of 800 K. During deposition, the flux of Pd atoms from the evaporator was kept at 4 nA for a duration for 60 minutes. Following the first dose, while a certain amount of Pd was detected in XPS, only a very faint Pd(111)-(1×1) pattern was observed in LEED. Therefore, a second Pd dose at the same nominal settings was carried out. After that, a larger amount of Pd was observed in XPS, and a much clearer Pd(111)-(1×1) pattern was detected in LEED (figure 5.1), indicating a larger coverage of Pd on the TiO_2(110) surface. Compared with the positions of the LEED spots of the TiO_2(110) substrate, figure 5.1 reveals an interatomic spacing of the Pd(111) facets of ∼2.86 Å, which is 4% larger than the value of 2.75 Å calculated from the lattice constant of bulk Pd. Note that the Pd(111) diffraction spots are very faint, which makes precisely locating the centre of the diffraction spots difficult, leading to a larger error when determining the interatomic distance of the Pd islands.

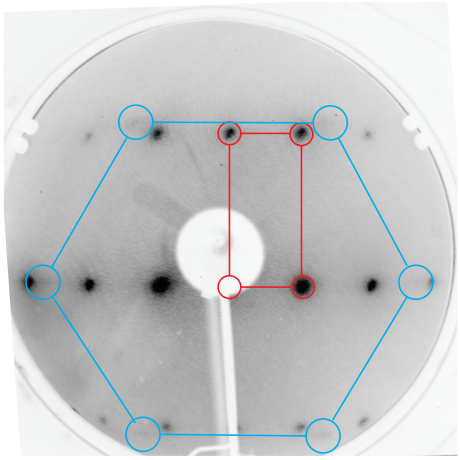

Figure 5.1: 139 eV LEED imaging displaying TiO_2(110)(1×1) and Pd(111)(1×1) diffraction patterns. By measuring the nearest-distance between (111) diffraction spots, the interatomic spacing on the Pd(111) islands was calculated to be ∼2.86 Å, deviating from the value of 2.75 Å calculated from the lattice constant of Pd single crystals.

It has been reported that encapsulation of Pd islands by Ti species coming from the TiO_2(110) substrate might occur above a sample temperature during deposition of ∼650 K [29]. Therefore the Ti 2*p* XPS peaks were monitored before and after the Pd dose

at elevated temperature. These spectra are displayed in figure 5.2. The binding energy position of the Ti $2p_{3/2}$ peak is at 458.5 eV for the as-prepared TiO_2(110) surface, which shifts to 458.75 after the first Pd dose, and back to 458.3 eV following the second Pd dose. This binding energy shift is caused by band-bending, resulting from changes in the population of the defect state located ∼0.9 eV below E_F in the band-gap. This effect will be discussed in more detail later.

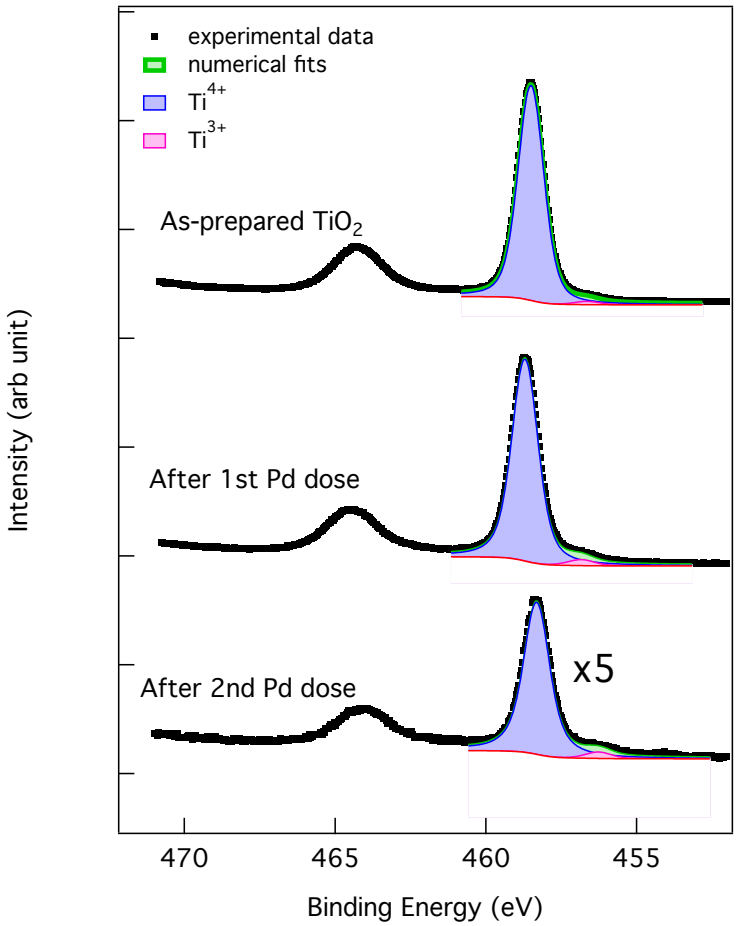

Figure 5.2: Ti 2p XPS spectra recorded at 300 K from (top) the as-prepared TiO_2(110) surface and the surface after (middle) the first and (bottom) second Pd dose with the substrate at ∼800 K. All spectra were recorded at normal emission with the photon energy at 620 eV. The spectra were normalised based on the analyser settings and their acquisition time. Black dots are the experiment data, and coloured lines the corresponding numerical fits to the Ti $2p_{3/2}$ peaks. The blue and pink lines represent the contributions from the Ti^{4+} and Ti^{3+} species.

To determine the extent of encapsulation the relative amounts of Ti^{4+} and Ti^{3+} species on the surface were calculated by performing numerical fits to the region around the Ti $2p_{3/2}$ peaks show in figure 5.2. The same procedure has been adopted in previous studies

[30]. On the as-prepared $TiO_2(110)$ surface, the percentage of the amount of Ti^{4+} and Ti^{3+} species is 98.5 ± 1.6 % and 1.5 ± 0.1 % respectively, which then changes to 97.1 ± 1.9 % and 2.9 ± 0.1 % after the first Pd dose, and then to 96.3 ± 7.5 % and 3.7 ± 0.4 % following the second dose. Bowker *et al.* reported the presence of Ti^{2+} at the Pd/TiO_2 surface due to encapsulation [15]. We do not observe any Ti^{2+}, and together with the very small increase in Ti^{3+} (2.2 %), this confirms the lack of encapsulation of Pd by Ti. We attribute the rise in Ti^{3+} to prolonged heating of the sample (2 hours) during Pd deposition.

We used the change in integrated intensity of Ti $2p_{3/2}$ peaks to determine the amount of Pd present following the first and second deposition. As the photon flux of the synchrotron light was not monitored properly during the experiment, we take the uncertainty in photon flux into account by assuming the uncertainty in the total area of the Ti $2p_{3/2}$ peak to be 33% of the value obtained from numerical fits. The calculated areas of the Ti $2p_{3/2}$ peaks are 3.0 ± 1.0 (in arb unit), 3.0 ± 1.0 and 0.48 ± 0.16 corresponding to the bare $TiO_2(110)$, and after the first and second Pd doses respectively. The effective thickness, d, of the Pd overlayer of can be calculated using the following equation: [31]

$$d = \lambda(E) \cos\theta \ln\left(\frac{I_0}{I}\right) \tag{5.1a}$$

with its uncertainty Δd equal to

$$\Delta d = \lambda(E) \cos\theta \left(\frac{\Delta I_0}{I_0} + \frac{\Delta I}{I}\right) \tag{5.1b}$$

where I_0 and I are the calculated areas of the Ti $2p_{3/2}$ peak of the as-prepared and Pd-covered $TiO_2(110)$, $\lambda(E)$ is the inelastic mean free path of electrons in palladium, which is estimated to be 5.67 Å at $E = 161.5$ eV [32], and θ is the angle of emission. All XPS were recorded at normal emission, $\theta = 0$, hence $\cos\theta = 1$. Using equation 5.1a, the thickness of the Pd overlayer is calculated to be 0.0 ± 3.7 Å after the first dose and 10.4 ± 3.7 Å after the second dose. This means that there was only a very small amount of Pd present on the substrate after the first dose, and its amount increased drastically after the second dose.

Photoemission spectra of the Pd $3d$ peaks were also recorded following each Pd dose. Numerical fits to the experimental data in figure 5.3 reveal a BE shift of the Pd $3d_{5/2}$ peak from 334.5 eV after the first dose to 333.9 eV after the second dose. The higher BE value of the Pd $3d$ peak following the first dose is probably due to a strong interaction between Pd atoms and the substrate when only a small amount of Pd is present. The decrease in BE following the second dose can be explained by the fact that when much larger amount of Pd is deposited onto the substrate, most of the Pd atoms have little or no interaction with the TiO_2 substrate, leading to a BE position close to that of bulk Pd.

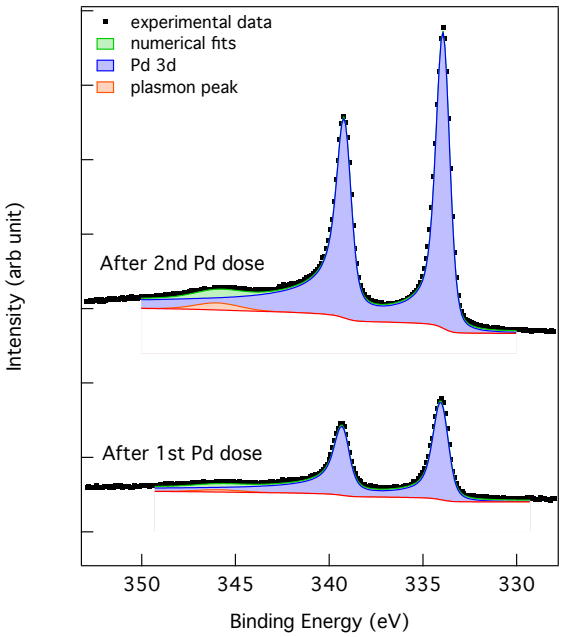

Figure 5.3: Pd *3d* XPS spectra recorded at 300 K from the TiO_2 surface after the first (top) and second Pd doses with the substrate at ∼800 K (bottom). The spectra were recorded at normal emission at a photon energy of 620 eV. The spectra are normalised by the analyser settings and the acquisition time. Black dots represent the experiment data and the coloured lines are the numerical fits. The blue and pink lines denote the Pd $3d$ doublets and the associated plasmon loss peak, respectively.

After the synchrotron experiments, STM data was recorded from the Pd/TiO_2 system in London and this is displayed in figure 5.4. This shows that following the second dose, the $TiO_2(110)$ substrate was fully covered with Pd islands with average diameter of ~ 10 nm and heights varying from 2 nm to 8 nm.

After growing Pd islands on the TiO_2 surface, C K-edge NEXAFS measurements were

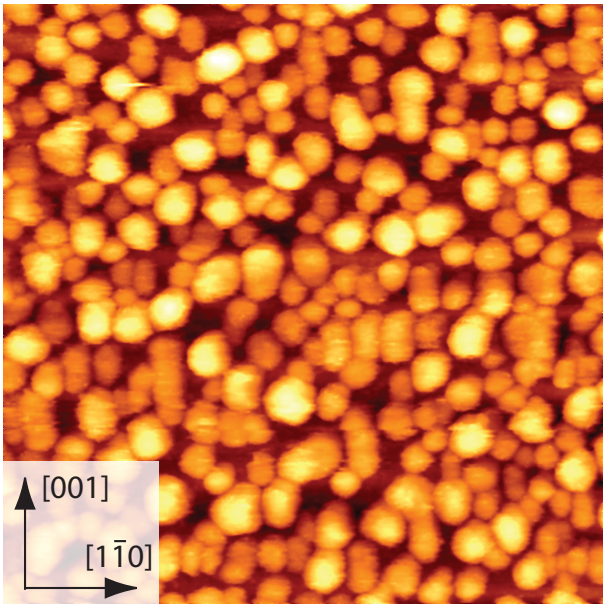

Figure 5.4: A STM picture recorded from the Pd-covered TiO_2 surface after the experiment in Max-Lab (200×200 nm^2, $V_s = 1.5$ V, $I_t = 1.0$ nA). The azimuth of the $TiO_2(110)$ substrate is marked at the bottom-left corner. This image shows that the substrate is covered with Pd islands with average diameter ~ 10 nm and height varying between 2 nm and 8 nm.

performed in order to investigate the bonding of CO to the Pd islands. This was achieved by first recording the C KLL Auger transition yield as a function of photon energy between 280 eV and 320 eV at different incident angles from the Pd/TiO_2 surface before and after exposing the surface to 2000 L of CO. To detect the C KLL Auger transition yield, the kinetic energy window of the analyser was set at 265 eV with a width of ΔE=4.4 eV.

The raw signal obtained during a NEXAFS measurement is the result of the combination of factors, of which the signal from the species of interest may be only a small component. Unwanted signals include those arising from time-dependent incident X-ray intensity, the transmission function of the monochromator for the first and higher harmonic light, the detector response to the signal originating from the sample, and that from the substrate. In our study of the bonding geometry of CO on the Pd islands, the signal originating from the CO molecules was only a very small portion of the raw signal. In order to extract the signal arising from CO, one is required to eliminate the unwanted signal. This is achieved by normalisation and background corrections. In our case, normalisation of the NEXAFS spectra was achieved by dividing the spectra obtained from the CO-covered surface by

that from the $Pd/TiO_2(110)$ surface prior to CO exposure. Before division, the spectra were scaled to the same value before the pre-adsorption region of the carbon K-edge, that is, in the region before 286.5 eV. The resulting NEXAFS spectra recorded at different incident angles are displayed in figure 5.5.

Each spectrum consists of a sharp peak at ∼287.2 eV overlapping with a step-like feature. The sharp peak corresponds to the π^* resonance, in which the $1s$ electrons in C atoms are photo-excited to the unoccupied π^* orbitals of CO. The step-like feature centred at ∼286.5 eV is called the Fermi Level (FL) step, whose energy position corresponds to the binding energy of the C $1s$ electrons in CO with respect to the E_{F}. This feature arises from the strong interaction of the π^* orbitals with the densely spaced unoccupied states of the metal above the Fermi level when the adsorbates are strongly bonded to the metal surfaces, leading to electronic transitions of the C $1s$ electrons in CO to the unoccupied states in the metal. [33]

As we have already confirmed that the $TiO_2(110)$ surface is almost fully covered with Pd islands (∼95 % of the total surface area), we can assume that only CO molecules bonded to the Pd islands contribute to the C K-edge X-ray absorption signals. To determine the orientation of CO molecules on the Pd islands, taking the three-fold symmetry of the Pd islands into account, we numerically fit the calculated area of the π^* peak (at different angles) using the following equation [34]

$$I = B[PI_p^{\parallel} + (1-P)I_p^{\perp}] \tag{5.2a}$$

where

$$I_p^{\parallel} = \frac{2}{3}\Big[1 - \frac{1}{4}(3\cos^2\theta - 1)(3\cos^2\gamma - 1)\Big] \tag{5.2b}$$

and

$$I_p^{\perp} = \frac{1}{2}(1 + \cos^2\gamma) \tag{5.2c}$$

where B is an arbitrary constant, P is the polarisation factor of the synchrotron light, $\mathrm{I}_p^{\parallel}$ ($I_p^{\perp}$) is the resonant intensity arising from the parallel (perpendicular) component of the

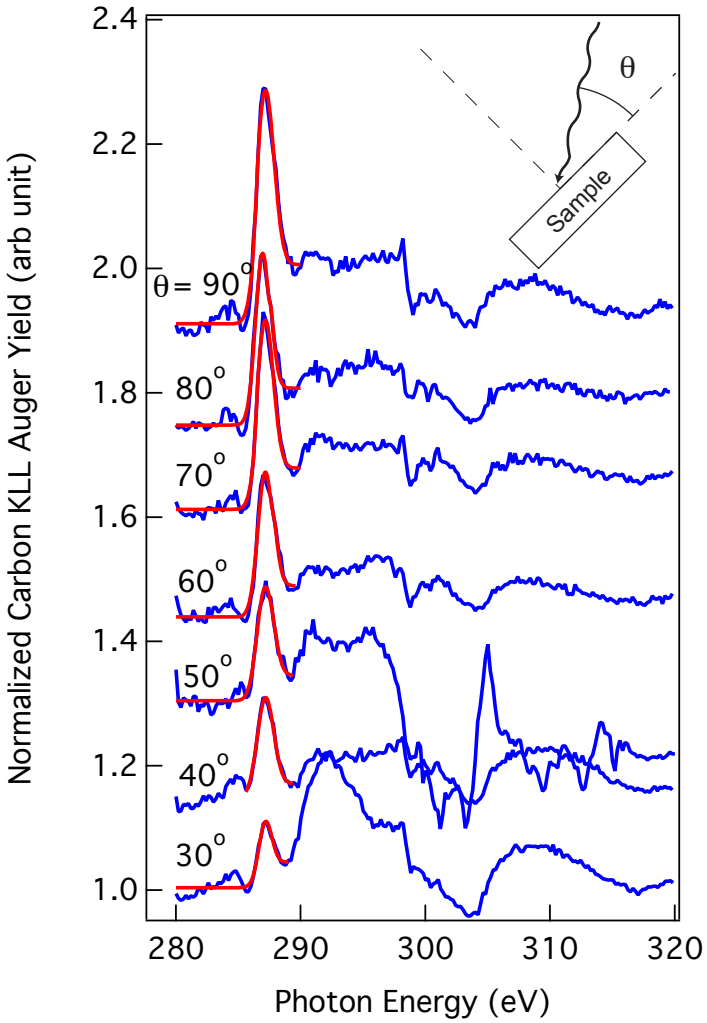

Figure 5.5: Normalized C KLL Auger yield as a function of photon energy measured at different incident angles on CO covered Pd(111) facets grown on TiO_2(110), recorded at room temperature. Blue dots are experimental data and red solid lines are numerical fits.

synchrotron light, and θ and γ are the incident angle and the angle between the surface normal and the normal of the π^* plane orbital (i.e. the C-O axis) respectively. The polarisation factor P was estimated to be 0.94. By using this value, the numerical fit to the experimental data, which is plotted as solid curves in figure 5.6, gives the best value of γ to be $10.6 \pm 13.1°$. Within the error bars, this means that CO molecules bond vertically on the Pd(111) facets on TiO_2(110).

As shown in Figure 5.5, contrary to other NEXAFS studies of CO on surfaces, we could not detect the σ^* resonant peak, which should locate at ~300 eV in the spectra. This might be explained as follow: when taking the carbon K-edge NEXAFS spectra of CO

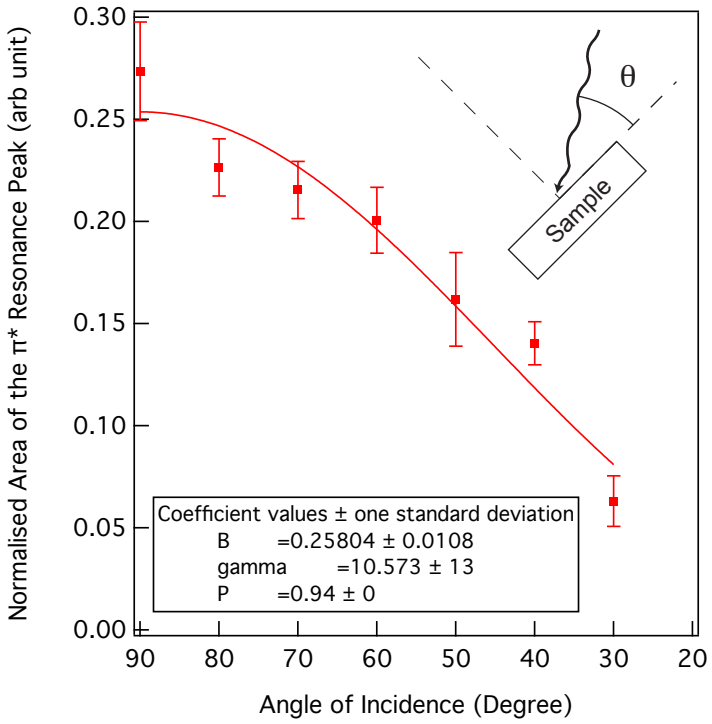

Figure 5.6: Normalised area of the CO π^* resonant peak as a function of incident angle. Dots are experimental data, and the solid line is numerical fit to the experimental data using equation 5.2. The best-fit values shown are the arbitrary constant B, Polarisation factor P, and the angle between the normal to the π^* orbital plane and the surface normal

by measuring the carbon KLL Auger yield, the energy analyser was operated at constant final state (CFS) mode with the kinetic energy window set at 265±2.2 eV. At this setting and while the photon energy is ramped between 280 eV and 320 eV, apart from the Auger electrons, the electrons with binding energies between 15 eV and 55 eV from the substrate are photo-excited and enter the analyser. This is in particular troublesome when TiO_2 is used as a substrate because the electrons at the Ti $3p$ (BE = 37.6 eV) and O $2s$ (BE = 41.6 eV) core levels will be photo-excited and enter the analyser, hence contributing to the raw NEXAFS signal. Note that photo-excitation of electrons from the Ti $3p$ core level results in an apparent absorption peak at ∼300 eV in the raw NEXAFS spectra, in which the σ^* resonant peak is buried. Furthermore, the population of the Ti $3p$ core levels might have altered following CO exposure. This makes the elimination of the substrate signal even harder and probably explains why no σ^* resonance of CO was observed in our experiment.

5.3.2 Results in London

5.3.2.1 Calibration of Pd Evaporator

The Pd evaporator used in London consisted of a Pd rod (1.0 mm, 99.95 %, Advent) wrapped with a tungsten filament. By passing a current through the filament, it heats up to a temperature threshold at which Pd atoms start to evaporate from the rod. As this evaporator did not have a flux monitor, it was necessary to determine the evaporation rate of Pd atoms at different evaporator settings before beginning the experiment.

The fact that Pd grows on TiO_2(110) in the Volmer-Weber mode makes calibrating the Pd evaporator using TiO_2 as a substrate impossible [35]. However, the calibration work can be achieved by employing Pt(111), on which Pd grows in a pseudomorphic Stranski-Krastinov growth mode [36]. To calibrate the Pd evaporator for our study, we deposited different amounts of Pd onto the Pt(111) surface and monitored the evolution of the Pd $3d$ and Pt $4d$ peaks in the XPS spectra. The Pd evaporator was calibrated at three different filament current settings (3.3, 3.4 and 3.5 A).

Figure 5.7 shows the XPS spectra recorded from the Pt(111) surface following Pd deposition for different durations at ∼300 K. In this case, the filament current of the Pd evaporator was set at 3.3 A. In the spectra, the peaks at binding energies of ∼340.1 eV and ∼334.7 eV are identified as the Pd $3d_{3/2}$ and $3d_{5/2}$ peaks, and the peaks at ∼330.8 eV and ∼314 eV correspond to the Pt $4d_{3/2}$ and $4d_{5/2}$ peaks.

The first step to determine the evaporation rate of the Pd doser is to separate the contributions from the Pd $3d$ and Pt $4d$ core levels to the photoemission spectra in the same energy region, as shown in Figure 5.7. This was achieved by first obtaining a Pt $4d$ line-shape for the clean Pt(111) surface by convoluting Doniach-Sunjic functions [31] and Gaussian functions due to instrumental broadening. Here, we set the Gaussian, the Lorentzian, and the asymmetry parameters free to improve the fit using a chi-square minimization procedure. After that, to de-convolute the Pd $3d$ spectra which overlap with the Pt $4d_{3/2}$ peak, the

Pt $4d$ line-shape was fixed for all its characteristic parameters except the peak height and the energy positions. The Pd $3d$ line-shape was then extracted by simply convoluting a pair of Gaussian and Doniach-Sunjic line-shape. The summation of the Pt $4d$ and Pd $3d$ line-shapes obtained from XPS fitting to the experiment data for different Pd deposition time are plotted as solid lines in 5.7.

The area of the Pd $3d$ photoemission peaks were then calculated from the line-shapes and the results are displayed in Figure 5.8. Note that the area of Pd $3d$ peak is indeed the total area of the Pd $3d$ doublet ($3d_{3/2}$ and $3d_{5/2}$). As shown in figure 5.8, the area of Pd $3d$ peak decreases monotonically upon Pd deposition, and there exists a breakpoint in the middle of the plot, indicative of the completion of the first monolayer coverage of Pd. As the breakpoint must satisfy the equations of both linear fits:

$$A = a_j + b_j t \tag{5.3}$$

where A denotes the area of the Pd $3d$ peaks, t corresponds to the Pd deposition time, and $j = 1$, 2, and a_1 (a_2) and b_1 (b_2) are the slope and y-intercept of the linear fit in red (blue) in Figure 5.8. By solving the above equations simultaneously, the deposition time for a monolayer coverage was determined to be 727.7 ± 278.2 s. This means that the deposition rate of the Pd doser at 3.3 A is $(1.37 \pm 0.53) \times 10^{-3}$ ML·s^{-1} or $(2.07 \pm 0.79) \times 10^{12}$ atoms·cm^{-2}·s^{-1}. Note that the line-shapes shown in green in Figure 5.7, which were obtained from the Pt(111) surface covered with more or less monolayer coverage of Pd as judged Figure 5.8, agree qualitatively with those obtained with the work of Han et al [37].

The Pd evaporator was also calibrated at doser settings of 3.4 A and 3.5 A. This was achieved by first plotting the area ratio of the Pd $3d$ and Pt $4d$ peak as a function of Pd deposition time for the three different doser settings. Note that the area of the Pt $4d$ peaks were also calculated from the line-shapes in figure 5.7. As the Pd deposition rate at 3.3 A has been determined (see figure 5.8), using the ratio between their slope values, the absolute Pd deposition rate at 3.4 A and 3.5 A can also be calculated.

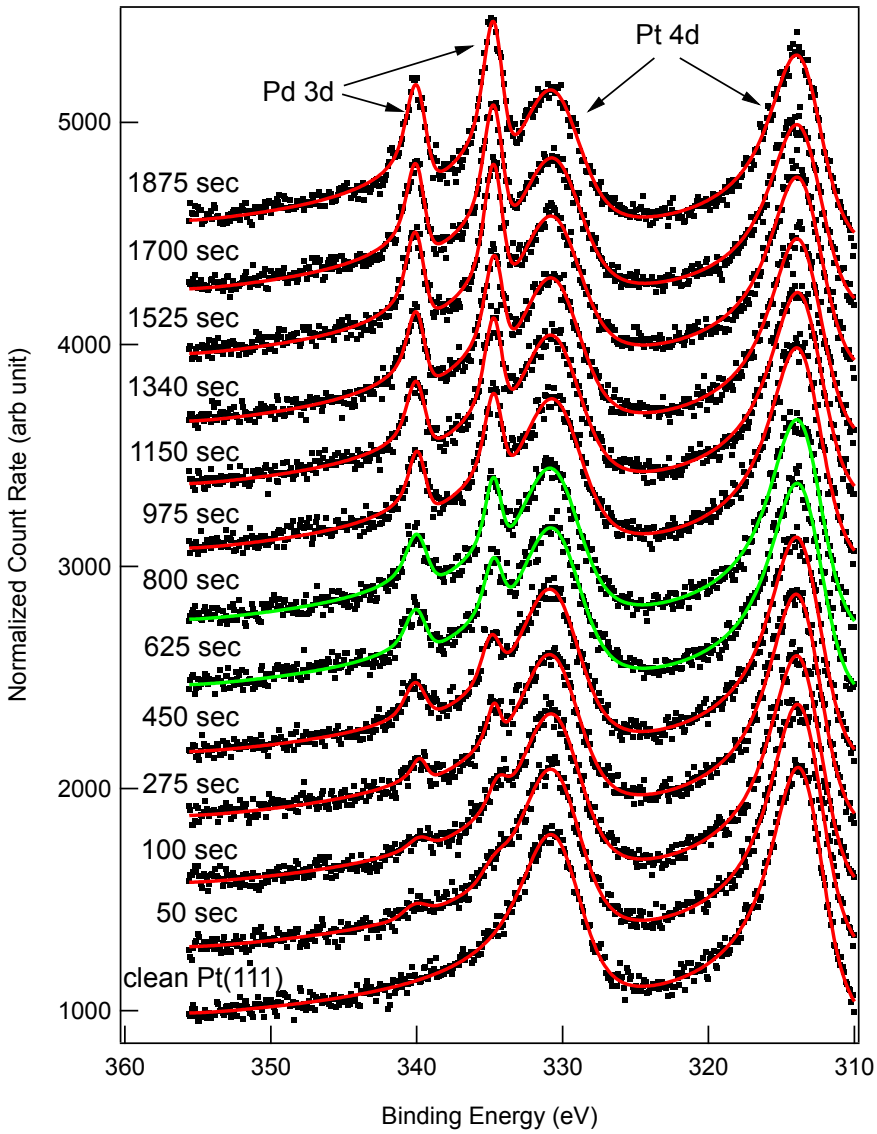

Figure 5.7: XPS spectra of Pt $4d$ and Pd $3d$ core levels recorded following Pd deposition on Pt(111) at ∼300 K for different durations. The X-ray source used was Al Kα ($h\nu$ = 1486.6 eV). The Pd evaporator was run at a filament current of 3.3 A, and warmed up for 120 s before dosing. Solid lines are numerical fits to the data. The XPS spectra recorded for different durations of Pd deposition are offset for clarity. The line-shapes shown in green, which were obtained from the Pt(111) surface covered with more or less monolayer coverage of Pd as judged in figure 5.8, agree qualitatively with those obtained with the work of Han *et al.* [37].

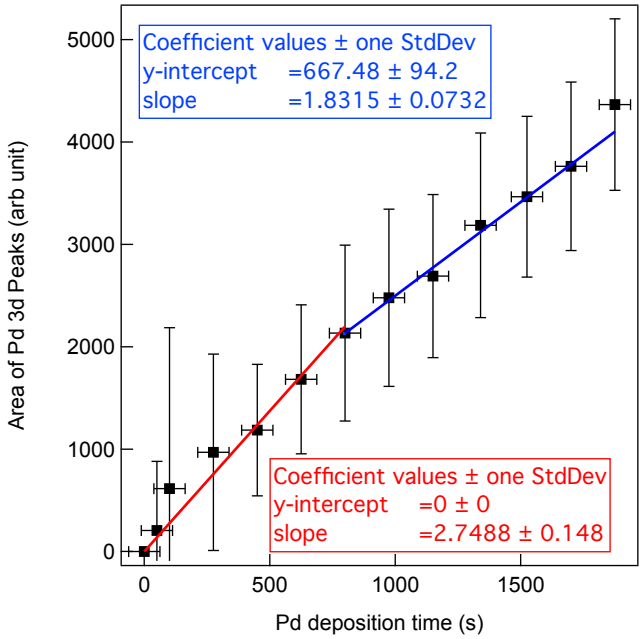

Figure 5.8: Area of the Pd $3d$ peaks as a function of Pd deposition time. A breakpoint, which is indicative of the completion of the monolayer coverage of Pd on Pt(111) and at which the linear fits intersect with each other, was found.

As shown in figure 5.9, the slope values determined from the area ratio of Pd $3d$ and Pt $4d$ peaks as a function of Pd deposition time at the evaporator settings of 3.3, 3.4 and 3.5 A are calculated to be $1.03 \times 10^{-4} \pm 1.43 \times 10^{-6}$, $1.46 \times 10^{-4} \pm 4.05 \times 10^{-6}$ and $1.45 \times 10^{-4} \pm 2.82 \times 10^{-6}$ respectively. By using these values and the absolute deposition rate at 3.3 A, $(1.37 \pm 0.53) \times 10^{-3}$ ML·s^{-1}, the deposition rate at 3.4 A and 3.5 A are calculated to be $(1.94 \pm 0.83) \times 10^{-3}$ ML·s^{-1} and $(1.93 \pm 0.80) \times 10^{-3}$ ML·s^{-1} or $(2.93 \pm 1.24) \times 10^{12}$ atoms·cm^{-2}·s^{-1} and $(2.91 \pm 1.21) \times 10^{12}$ atoms·cm^{-2}·s^{-1} respectively. These values will be used to estimate the total amount of Pd deposited onto the TiO_2(110) surface in the following section.

Note that the calibration work performed on the Pd/Pt(111) system was performed to give an approximate idea of the Pd deposition rates at particular doser settings. In further experiments, XPS was employed to determine the amount of Pd present on the TiO_2(110) surface. This was achieved based on the electron escape depth and by assuming that Pd forms a homogeneous film on the TiO_2(110) surface. Coverages determined in this way

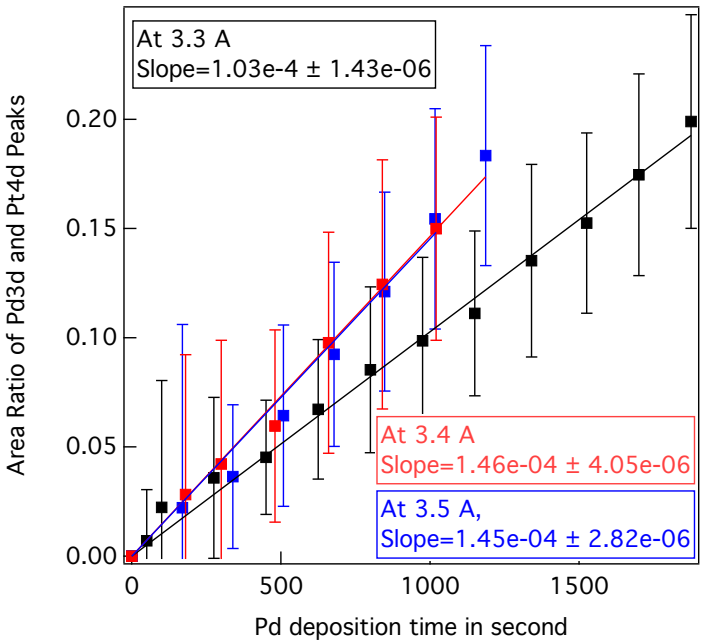

Figure 5.9: Area ratio of Pd $3d$ and Pt $4d$ peaks as function of Pd deposition time at three different Pd evaporator settings. The slope values for each doser setting are indicated. By using the slope values and the Pd deposition rate at 3.3 A, the Pd deposition rates at 3.4 and 3.5 A were also determined.

can only be considered nominal. As will be shown in STM later, by depositing Pd at elevated substrate temperature, Pd forms rather thick islands on the TiO_2(110) surface, in which case the attenuated intensity of the Ti 2p peak in XPS will be dominated by the area of the TiO_2 substrate covered with Pd islands.

5.3.2.2 STM Results

The first aim of the experiments performed in London was to prepare a Pd on TiO_2(110) surface which exhibited a similar LEED pattern to the surface studied in the synchrotron experiments in Max-Lab. This surface was then examined *in-situ* using X-ray photoemission spectroscopy and STM. To prepare a Pd/TiO_2 system similar to that in Max-Lab, palladium was evaporated onto the as-prepared TiO_2(110) surface at a sample temperature of ~773 K. During deposition, the setting of the Pd evaporator was kept at a filament current of 3.5 A for a duration 30 minutes. Pd deposition rate of the doser at 3.5 A was

determined to be $\sim 2.9 \times 10^{12}$ atoms·cm^{-2}·s^{-1} previously.

Following Pd deposition, a very faint Pd(111)-(1×1) pattern was observed in LEED. Careful inspection of the diffraction pattern in figure 5.10 reveals an interatomic spacing of the Pd(111) facets of ∼2.70 Å, ∼2 % smaller than the value of 2.75 Å calculated from the lattice constant of bulk Pd.

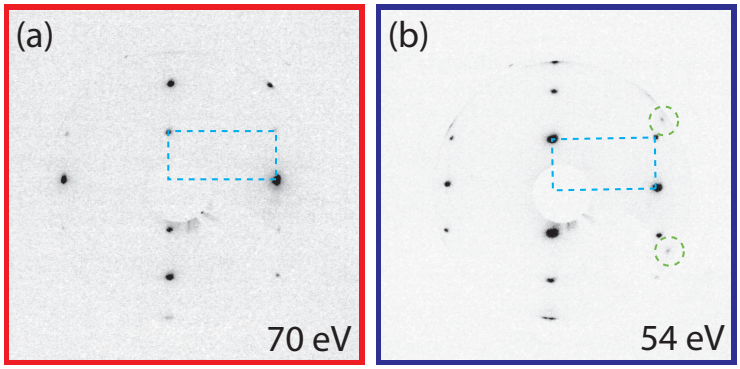

Figure 5.10: LEED patterns recorded from (a) the TiO_2(110) substrate and (b) the surface after Pd deposition at a sample temperature of 773 K. The blue dashed line and green circles indicate the TiO_2(110)-(1×1) and Pd(111)-(1×1) patterns respectively.

Ti 2p and Pd 3d XPS spectra were recorded to verify the similarity in chemical composition between this Pd/TiO_2 system and the one in Max-Lab. We first checked whether encapsulation of the Pd islands was taking place. The Ti 2p spectra in figure 5.11(a) illustrate that the concentration of Ti^{3+} species on the as-prepared TiO_2(110) surface was under the detection limit, and after Pd deposition, no noticeable change in its concentration is observed. This suggests that there was no encapsulation taking place on the Pd islands. In an attempt to calculate the Pd coverage on the TiO_2(110) substrate, we calculated the areas of the Ti $2p_{3/2}$ peaks by performing numerical fits to the experimental data using a Voigt profile and a Shirley background. The areas of the Ti $2p_{3/2}$ peaks before and after deposition are calculated to be 413 ± 32 (in arb unit) and 313 ± 31 respectively. The electron's inelastic mean free path $\lambda(E)$ at kinetic energy of 1028 eV is estimated to be 18.6 Å [32]. Using this value and by inserting the calculated areas of the Ti $2p_{3/2}$ peaks before and after Pd deposition, the effective thickness of the Pd overlayer was determined

to be 1.6 ± 1.0 Å. Using the inter-layer distance of the Pd(111) surface, $\sqrt{2/3} \times 2.75$ Å $= 2.245$ Å, the Pd coverage is calculated to be 0.71 ± 0.45 MLE (monolayer equivalent). This value lies between those calculated for the Pd/TiO_2 system after the first and second dose in Max-Lab.

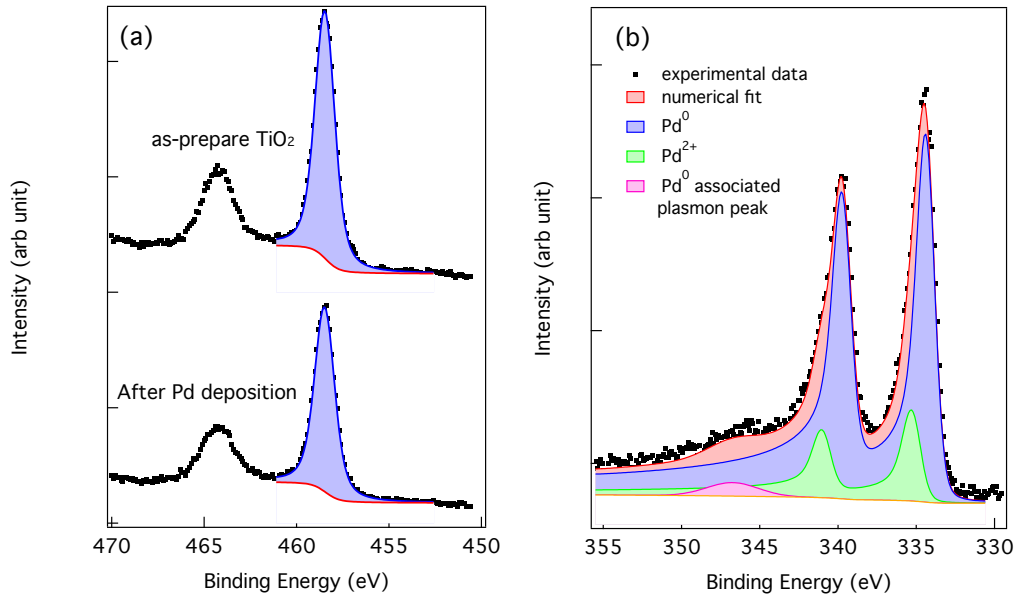

Figure 5.11: XPS spectra recorded from the clean $TiO_2(110)$ surface and the surface after Pd deposition. All spectra were recorded at normal emission and using Al Kα (1486.6 eV) as photon source, and normalised according to the analyser settings and acquisition time used. (a) Ti $2p$ spectra recorded before and after Pd deposition. Black dots are experiment data. Colour lines are numerical fits. (b) A Pd $3d$ spectrum recorded from the surface after Pd deposition. Black dots are experimental data. Solid lines are the numerical fits, among which the red line is the fit to the Pd^0 associated plasmon loss peak, and the blue and green lines correspond the fits to the Pd $3d$ doublets arising from Pd^0 and Pd^{2+} species, respectively.

Figure 5.11(b) displays the corresponding Pd $3d$ XPS spectrum recorded after Pd deposition. To determine the chemical composition of the Pd islands, we performed numerical fits to the experiment data. It was found that an acceptable chi-square value can be obtained only when two doublets (with Doniach-Sunjic line-shapes) were used in the fitting procedure, meaning that there are two different Pd species present. That with the $3d_{5/2}$ peak located at 334.4 eV, originates from Pd^0 species while the other with its $3d_{5/2}$ peak at 335.4 eV comes from Pd^{2+} species. The concentration ratio between Pd^0 and Pd^{2+} species is calculated to be $\sim$1:4.6. Based on the above observations, and bearing in mind that the XPS employed here is less surface-sensitive than that employing synchrotron ra-

diation, we suggest that the Pd^0 species come from the bulk or the top of the Pd islands. The Pd^{2+} species will originate from the $Pd/TiO_2(110)$ interface, where the Pd atoms have stronger interaction with the $TiO_2(110)$.

Apart from the chemical nature of the Pd nano-structures, their distribution and morphology over the $TiO_2(110)$ substrate also have influence on their chemical reactivity. We employed STM to study their appearance on the $TiO_2(110)$ substrate. As shown in figure 5.12, the Pd islands, which have a pseudo-hexagonal shape, distribute evenly on the $TiO_2(110)$ surface. These Pd islands have (111) top facets, as confirmed by LEED (figure 5.10), and have their $<1\bar{1}0>$ step-edges running parallel to the [001] direction of the $TiO_2(110)$ surface. The Pd islands are measured to have an average diameter of 32 ± 5.9 nm and height of 4.8 ± 1.5 nm. Using those statistics, the area density of the TiO_2 substrate covered with Pd islands is calculated to be 12%. By dividing the total volume of Pd islands by the scanned area in figure 5.12(a), and then by the inter-layer distance of the bulk Pd(111) surface (3.36 Å), we calculate that there are ∼1.7 ML of Pd atoms present on the surface. It should be noted that there are some exceptionally bright features also appearing on the surface. Those features, almost identical in shape, originate from a single $\sim$ 22 nm tall Pd island on the surface. Their repeated appearance in the STM image is due to convolution effect of the STM tip with that island.

We were also interested in the reactivity of those flat-top Pd(111) islands compared to single crystals. Here we used CO as a probe. The $Pd/TiO_2(110)$ surface was exposed to 2000 L of CO at 300 K, and then immediately transferred to the STM stage for imaging at 78 K. The reason for performing STM scanning at 78 K is that CO molecules are less mobile at low temperatures and thus more likely to form ordered structures on top of the Pd(111) islands.

To investigate how CO molecules adsorb on top of the Pd islands, we chose one of the Pd islands (highlighted with solid green lines in figure 5.12(a) and shown in figure 5.12(b)) and performed STM on the top of it. As shown in figure 5.12(c), we observe that while

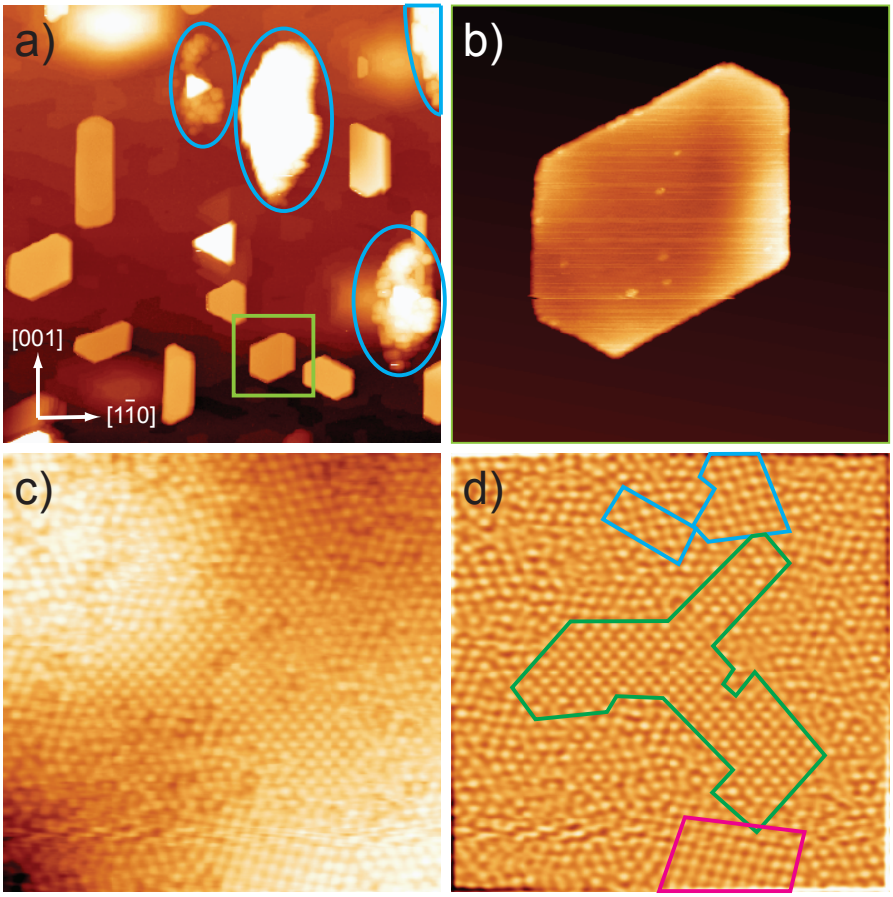

Figure 5.12: STM pictures recorded from the Pd/TiO_2(110) system following 2000 L of CO exposure at 300 K. All STM data were taken at 78 K. (a) A STM image (250×250 nm^2) showing pseudo-hexagonal Pd islands distributing over the substrate. The islands are calculated to have an average diameter of ∼30 nm and height of ∼5 nm. (b) A zoomed-in image (55×55 nm^2) of the Pd island highlighted with a green box in (a). (c) An atomically resolved image (size = 10×10 nm^2, V_s = 0.6 V, I_t = 0.1 nA) taken from the topface of the Pd island in (b), showing CO molecules form different ordered domains on top of the Pd(111) islands. (d), A band-filtered image of (c), in which different domains of CO are highlighted with different coloured boxes.

some CO molecules (bright dots) adsorb randomly, others form ordered structures on top of the Pd(111) island.

To resolve the CO ordered phases more clearly, we performed band-pass filtering to the STM image in Figure 5.12(c), with the exact procedures described as follow: firstly, we performed fast Fourier transform (FFT) to the raw STM image (Fig. 5.13(a)), leading to its corresponding FFT spectrum shown in Fig. 5.13(d). In the FFT spectrum, we concluded that the bright spots inside the shaded region are analogous to the diffraction spots of the CO ordered phases, and the spot at the centre and those outside the shaded

region correspond to the non-uniform background and other periodic noises present during data acquisition respectively. While keeping the information relevant to the CO ordered phases, all other features were removed, resulting in a modified FFT spectrum shown in Fig. 5.13(e). Then, by performing a reverse FFT operation on the modified FFT spectrum, a filtered STM image is obtained, and is shown in Fig. 5.13(b). For clarity, we also show the image which contains the information that has been removed during band-pass operation. This is shown in Fig. 5.13(c) and its corresponding FFT spectrum in 5.13(f).

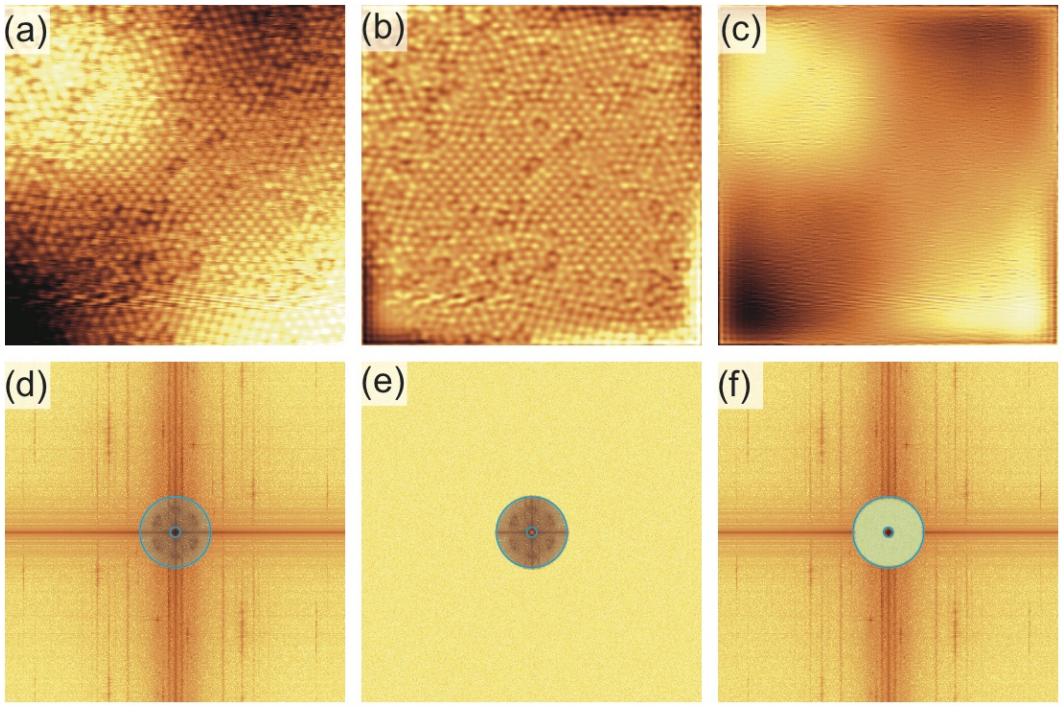

Figure 5.13: (a) The raw STM image shown in Fig. 5.12(c). (b) The resulting image and (c) the background information that has been removed following band-pass operation. (d-f) The corresponding FFT spectra, in which the band-pass region, which includes the spots explaining the periodicities of the CO ordered phases, are highlighted in blue.

In the filtered STM image displayed in Fig. 5.12(d), we can see very clearly that there are three different domains of CO ordering formed on the Pd islands. The analysis work on the CO domains is as follow: Figure 5.14(a)-(c) are the zoomed-in images of different domains of CO ordering formed on the Pd(111) island. By mapping the zoomed in images with a grid of Pd(111) unit cells, we determine that in each of the domains CO form c(4×2)-2CO ordered superstructure. As expected for c(4×2) ordering on Pd(111), the primitive cells of the c(4×2) structures displayed in figure 5.14(a), (b) and (c) measure

$570 \times 460 \pm 10$ pm, $530 \times 480 \pm 10$ pm and $570 \times 460 \pm 10$ pm respectively, very close to the previously reported value on the Pd(111) single crystal, $560 \times 480 \pm 10$ pm [38], and the primitive axes lie along the Pd(111) facet's $\{01\bar{1}\}$ and $\{\bar{2}11\}$ directions.

Closer inspection reveals that while CO molecules appear with the same brightness in figure 5.14(b) and (c), in figure 5.14(a), half of the CO appear brighter than the other. As all the c(4 × 2)-2CO structures occur within the same scan and do not alter between scans, we conclude that the contrast difference is not tip-related. On the Pd(111) single crystal, Rose *et al.* [38] reported two different c(4 × 2)-2CO structures, in one of which CO occupy bright sites (bridge-bridge c(4 × 2)-2CO) while in the other CO occupy fcc and hcp threefold hollow sites (hollow-hollow c(4 × 2)-2CO). By comparing ours to those reported by Rose *et al.* [38], we conclude that the c(4 × 2)-2CO orderings in figure 5.14(b) and (c) are of bridge-bridge type, and angled 60° from each other.

As for the case in figure 5.14(a), their height difference between CO is measured to be ∼8 pm, suggesting different site occupation. So far no such c(4 × 2)-2CO ordering has been reported on the Pd(111) surface. In order to find out the arrangement of CO in that c(4 × 2)-2CO ordering, we compared our results to those conducted on other fcc metal (111) surfaces, such as platinum. In the STM study of CO/Pt(111), Pedersen *et al.* [39] reported that CO form c(4 × 2)-2CO ordering in which CO occupy atop and bright sites, with the height difference between CO at different sites measured to be 16 pm. Also by considering that contrast in STM also depends upon the tunnelling conditions as well as the chemical nature of the STM tip, we suggest that in figure 5.14(a), the CO occupy both atop and bright sites, leading to a top-bright c(4 × 2)-2CO ordering, and illustrated schematically in figure 5.14(d). This top-bright c(4 × 2)-2CO configuration was not detected in Rose *et al.*'s measurements [38], and this might be explained by the difference in experimental procedures adopted. In their experiment, the CO coverage was increased stepwise at 120 K while any CO-induced overlayer formed on the Pd(111) surface was monitored *in-situ* in STM. At 120 K, CO moves rapidly on Pd(111). This, together with the slow dosing rate used, enabled an equilibrium configuration of CO on the Pd(111)

surface. Contrarily, in our case, the $Pd/TiO_2(110)$ surface was first saturated with 2000 L of CO (in 3×10^{-6} mbar) at 300 K and then quickly quenched to 78 K at the STM stage for imaging. This might result in the CO molecules, which are saturating CO molecules on the Pd(111) islands, not moving fast enough to reach their equilibrium configuration. In addition, a vibrational Sum Frequency Generation (SFG) spectroscopy study by Unterhalt *et al.* [40] suggests that attaining a top-bridge configuration on Pd(111) is possible at a CO coverage of ∼0.6 ML. These findings explain the co-existence of a disordered phase ($\theta_{CO} < 0.5$ ML) as well as a bridge-bridge ($\theta_{CO} = 0.5$ ML) and top-bridge c(4 × 2)-2CO ($\theta_{CO} \geq 0.5$ ML) ordered structures on the Pd(111) islands.

Based on the proposed top-bridge and bridge-bridge models in figure 5.14, two Pd(111) lattice grids can be generated and overlaid onto the STM image in figure 5.12(d). Crucially, this STM image contains domains of the proposed top-bridge and bridge-bridge c(4x2)-2CO models which lie on the same Pd(111) island. If the two models proposed are correct then the Pd(111) lattices generated from the two different domains must coincide. That this is indeed the case, as shown in figure 5.15, provides strong evidence to support the proposed models.

A transition between two of the c(4 × 2)-2CO phases was also observed and shown in figure 5.16(a)-(d). As shown in the area marked with blue dashed lines, the bridge-bridge c(4 × 2)-2CO phase remains for at least 13 minutes. Following varying the tunnelling current from 0.1 to 0.2 nA, the originally present bridge-bridge c(4 × 2)-2CO phase transforms into the top-bridge c(4 × 2)-2CO phase, which then transforms back to bright-bright c(4 × 2)-2CO phase. As we do not observe any similar transition in other regions in the same scanned area, we conclude that the transition is tip-driven, probably by interfering with the local distribution of CO. In addition, that the top-bridge c(4 × 2)-2CO phase transforms back to the original bridge-bridge c(4 × 2)-2CO phase suggests that the bridge-bridge configuration is relatively stable.

As stated by Xu *et al.* [41] and also experimentally observed by Schmidt *et al.* in the case

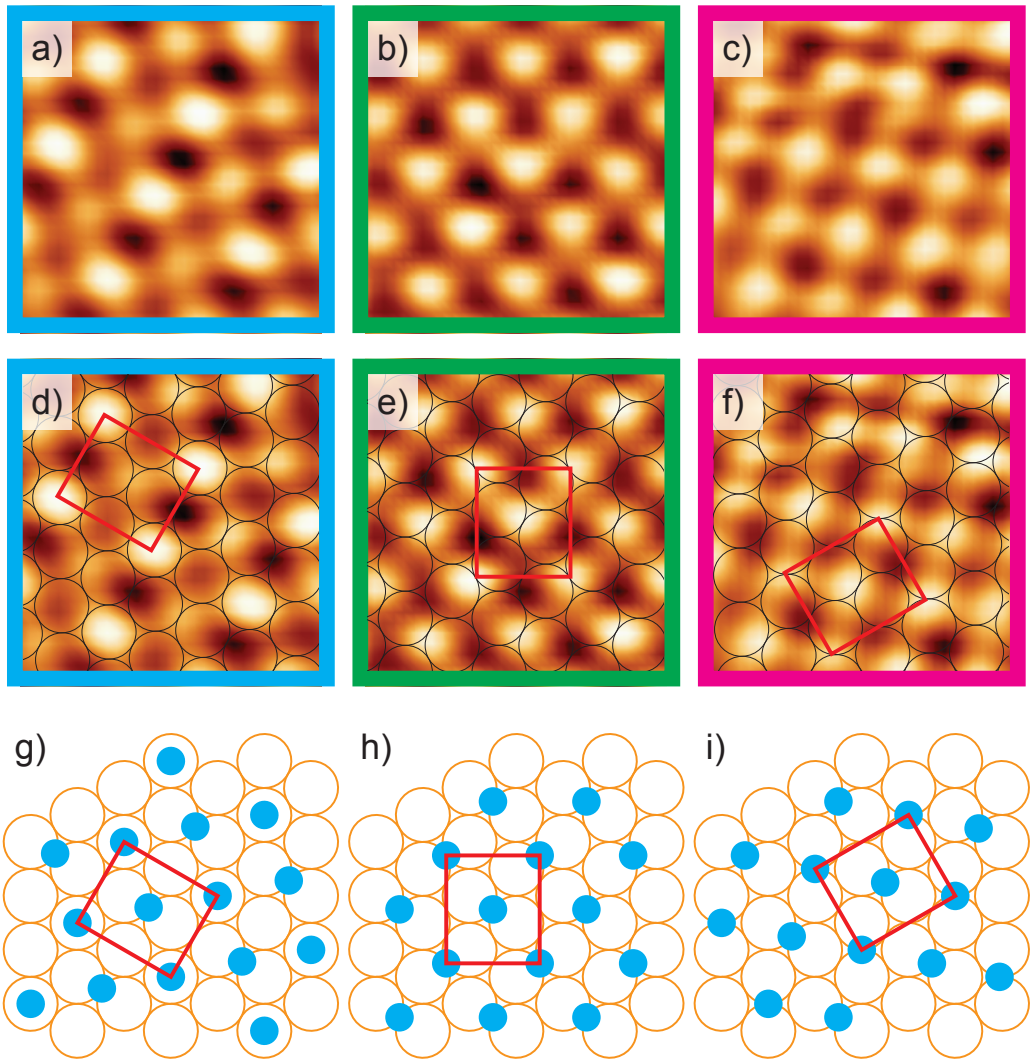

Figure 5.14: (a)-(c) Zoomed-in pictures (1.25×1.25 nm^2) of the CO domains highlighted with different coloured boxes in 5.14(d). In (a), CO form c(4 × 2)-2CO phase in which they occupy atop and bridge sites, while in (b) and (c) CO form two bridge-bridge c(4 × 2)-2CO orderings, which are angled 60° from each other. (d)-(f) The same pictures as (a)-(c), with the array of Pd atoms beneath the CO layer and the c(4 × 2)-2CO primitive unit cells marked with black and red lines respectively. (g-i) are the corresponding schematic illustrations, in which solid blue and hollow orange circles represent CO molecules and Pd atoms respectively. The c(4 × 2) primitive unit cells are marked with red lines.

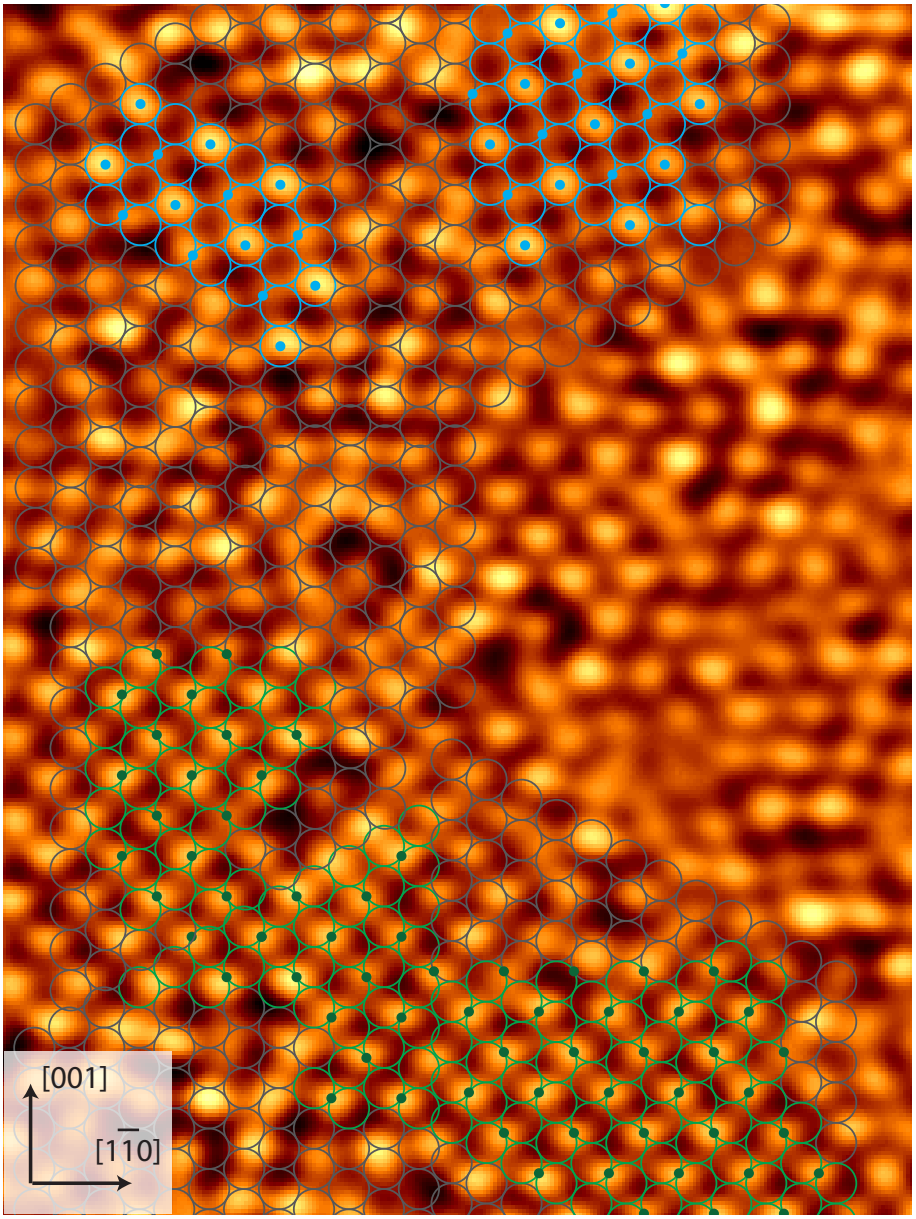

Figure 5.15: The STM image in figure 5.12(d) overlaid with a Pd(111) grid. Image size = 6.23×8.30 nm^2. In the image, the grid highlighted in blue denotes the region where CO molecules form top-bridge c(4×2)-2CO ordering, while that in green corresponds the region where CO forms bridge-bridge c(4×2)-2CO ordering. The arrows point to the crystallographic direction of the TiO_2(110) substrate.

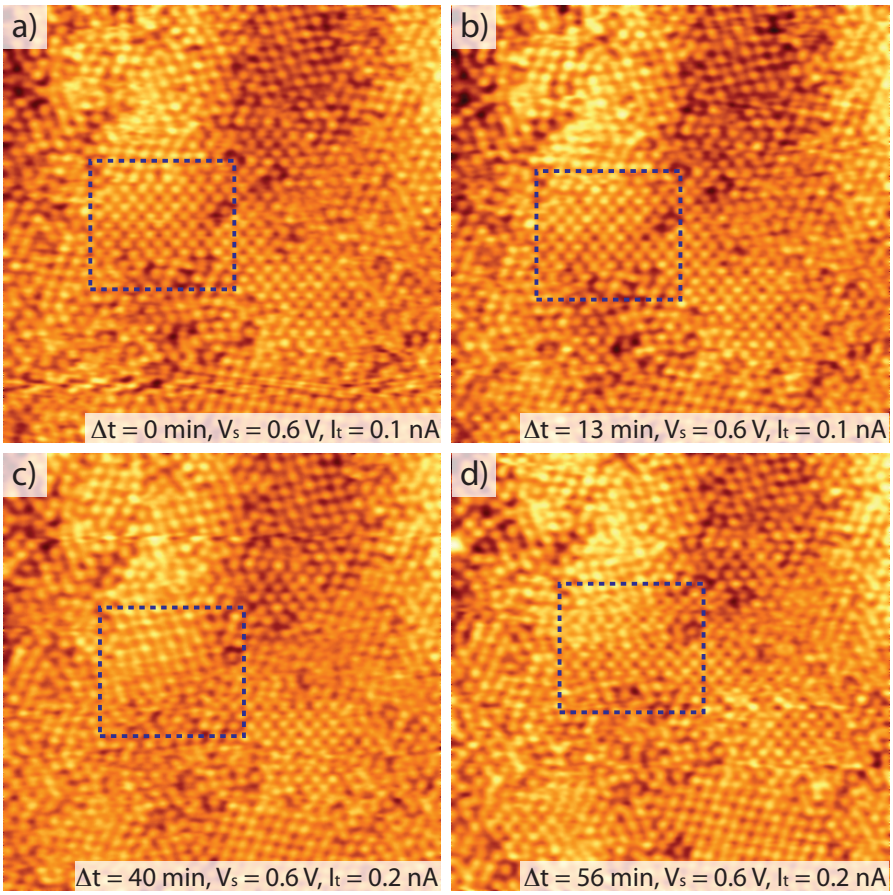

Figure 5.16: STM images (10×10 nm^2) showing a tip-induced transition between CO orderings on the Pd(111) islands. The region where the transition takes place is marked with blue-dashed lines. The time of image acquisition (with that of (a) set to 0 min) as well as the scanning parameters are indicated on the bottom-right corner of every image. (a)-(b) No transition takes place. (c) After changing the tunnelling current from 0.1 to 0.2 nA, the originally present bridge-bridge c(4×2)-2CO structure transforms into the top-bridge c(4×2)-2CO structure. (d) The top-bridge c(4×2)-2CO is transforming back into the original bridge-bridge c(4×2)-2CO.

of Pd growth on amorphoous Carbon [42], increasing metal flux results in higher island densities and smaller island sizes. To verify if this is also valid in the case of Pd on rutile TiO_2(110), we performed a similar experiment with a slower Pd deposition rate. This time, palladium was evaporated onto the as-prepared TiO_2(110) surface at the same temperature of ∼773 K. During deposition, the Pd evaporator was run at a filament current of 3.3 A for the same duration as before. The deposition rate at 3.3 A was determined to be $\sim 2.1 \times 10^{12}$ atoms·cm^{-2}·s^{-1}, 30 % slower than that at 3.5 A. The surface was then saturated with 2000 L of CO and transferred to the STM stage for imaging at 78 K.

As shown in figure 5.17(a), at a slower Pd deposition rate, there are much less but larger

Pd(111) islands formed on the TiO_2(110) surface. As in the picture there is only one Pd(111) island (other bright features are due to tip-surface convolution), we cannot accurately determine the number density of Pd(111) islands present on the TiO_2 substrate. The diameter and height of that island (highlighted with a green box) are 66 nm and 2.9 nm respectively. Figure 5.17(b) shows a magnified image of that island, on which the bright spots are believed to be adsorption of water molecules from the residual vacuum [43].

We also performed STM on top of the Pd island to check if there is any difference in chemical nature between this island and those grown at a faster Pd deposition rate. As shown in Figure 5.17(c), while some CO molecules adsorb randomly on the surface, others form different ordered domains on top of the Pd(111) island. Further analysis of the STM image (shown in figure 5.17(d)) illustrates that in each of the two domains (highlighted with light- and dark- blue solid lines in figure 5.17(c) CO form c(4×2)-2CO ordering, and the domains are angled 120° from each other. This indicates that while the Pd deposition rate affects the number density and size of Pd islands grown on the TiO_2(110) surface, it has no effect upon their chemical nature.

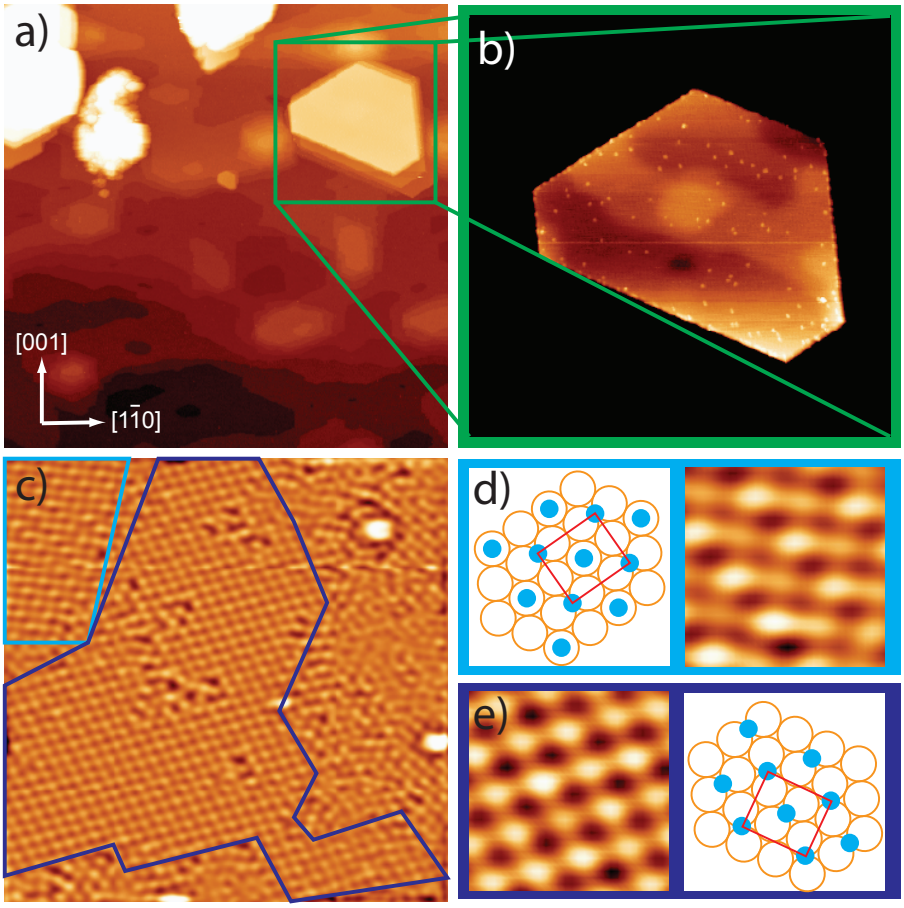

Figure 5.17: Another set of STM images taken from the $Pd/TiO_2(110)$ surface after 2000 L of CO exposure at 300 K. In this case, the Pd islands were grown at a doser setting of 3.3 A with the substrate held at 773 K. All pictures were recorded at 78 K. (a) A STM image (250×250 nm^2) showing only one or two Pd islands over the substrate. (b) A zoomed-in image (100×100 nm^2) of the Pd island highlighted in (a). The island has an average diameter of 66 nm and height of 2.9 nm, with the bright features on its top face are believed to be molecular water from residual vacuum. (c) A band-filtered STM image (10×10 nm^2) obtained from the topface of the Pd island, showing disordered and ordered CO phases formed on the Pd(111) island. (d-e) Zoomed-in images of the ordered phases highlighted with different coloured lines in (c) and their corresponding schematic illustrations. The regions highlighted with light blue and dark blue coloured lines correspond to the top-bridge and bridge-bridge c(4×2)-2CO ordered phases, respectively.

5.4 Conclusions and Future Work

The synchrotron photoemission spectroscopy (SXPS) measurements performed using Beamline I311 in Max-Lab II reveal that Pd nano-structures on TiO_2(110) grown at a sample temperature of 800 K are metallic and not encapsulated by Ti^{n+} ($n < 4$) species from the TiO_2(110) substrate. These Pd nano-structures have (111) topfaces, as confirmed by LEED. C K-edge NEXAFS measurements carried out on the Pd/TiO_2(110) surface before and after CO adsorption shows that CO molecules bond vertically on top of the Pd islands.

A similar experiment of the Pd/TiO_2(110) surface was also carried out in London. Using LEED as a gauge, Pd islands, which have (111) top faces, were grown on TiO_2(110). XPS results show that two kinds of Pd species, namely Pd^0 and Pd^{2+}, are present on the Pd/TiO_2(110) surface. The Pd^0 species, being the majority species, come from the bulk and the top face of the Pd islands, while the Pd^{2+} species, being the minority species, are those interacting with the TiO_2 substrate along the Pd/TiO_2(110) interface.

STM was also employed to study the distribution and morphology of those Pd islands on the TiO_2(110) substrate as well as the bonding of CO molecules on the top-face of the Pd(111) islands. STM results reveal that these Pd islands have a pseudo-hexagonal shape, with an average diameter of 30 nm and height of 5 nm. The number density and size of the Pd islands are dependent on the rate of Pd deposition during growth. High-resolution STM images recorded from the top face of the Pd(111) islands at 78 K following CO exposure at 300 K reveal that while some CO molecules adsorb randomly, others form domains of c(4×2)-2CO ordering on the Pd(111) islands in three orientations. In addition to the c(4×2)-2CO orderings, other coverage orderings such as $(\sqrt{3} \times \sqrt{3})$R30° and $(2 \times 2) - 3$CO reported by Rose *et al.* [38] on the Pd(111) single crystal studies were not present in our case, which we attribute to difference in experimental procedures adopted in both experiments.

Rather than saturating the Pd/TiO_2 surface with CO at 300 K, it would be interesting to expose the surface to CO at lower temperatures in the hope that dynamic change in

ordering of CO at different coverages can be observed on top of the Pd islands. Another potential experiment is to adsorb O_2 on the Pd islands and investigate how CO reacts with the O_2 molecules at elevated temperatures, which will be very useful for understanding the CO oxidation that takes place on Pd-containing catalysts.

Apart from gas adsorption, it would also be intriguing to study other properties of the Pd islands, in particular, encapsulation and at which condition(s) it will take place. For the Pd islands grown on TiO_2(110) surfaces at room temperature, previous work reports that encapsulation of Pd nano-islands starts to take place when the Pd/TiO_2 surface is annealed to a temperature above ∼800 K. Notably, by annealing the Pd islands-covered TiO_2(110) surface to 973 K, Bennett *et. al.* [44] observed in STM that those Pd islands are encapsulated by its underlying substrate, leading to the formation of pinwheel and zig-zag structures. Different from that reported previously, in our study the Pd islands were grown on the TiO_2(110) substrate with the sample held at ∼800 K, which probably explains why our Pd islands are not encapsulated.

References

[1] V. Zhdanov and B. Kasemo, *Surface Science*, 1998, **405**, 27–37.

[2] W. C. Conner and J. L. Falconer, *Chem Rev*, 1995, **95**, 759–788.

[3] S. J. Tauster, *Accounts Chem Res*, 1987, **20**, 389–394.

[4] W. L. Gao, J. X. Chen, X. X. Guan, R. C. Jin, F. X. Zhang and N. J. Guan, *Catal Today*, 2004, **93-5**, 333–339.

[5] W. Kim, J. Kang, I. Ahn and S. Moon, *J Catal*, 2004, **226**, 226–229.

[6] N. Macleod, R. Cropley and R. Lambert, *Catal Lett*, 2003, **86**, 69–75.

[7] K. D. A and D. P. Woodruff, *The chemical physics of solid surfaces and heterogeneous catalysis*, Elsevier Scientific Pub. Co., 1981.

[8] X. Lai, T. P. S. Clair, M. Valden and D. W. Goodman, *Prog Surf Sci*, 1998, **59**, 25–52.

[9] U. Diebold, J. M. Pan and T. E. Madey, *Phys Rev B*, 1993, **47**, 3868–3876.

[10] E. I. Ko and R. L. Garten, *J Catal*, 1981, **68**, 233–236.

[11] J. M. Herrmann, *Journal of Catalysis*, 1984, **89**, 404 – 412.

[12] R. T. K. Baker, E. B. Prestridge and G. B. McVicker, *Journal of Catalysis*, 1984, **89**, 422 – 432.

[13] Z. Chang and G. Thornton, *Surf Sci*, 2000, **459**, 303–309.

[14] M. Bowker, P. Stone, R. Bennett and N. Perkins, *Surf Sci*, 2002, **497**, 155–165.

[15] M. Bowker, P. Stone, P. Morrall, R. Smith, R. A. Bennett, N. Perkins, R. Kvon, C. L. Pang, E. Fourre and M. Hall, *Journal of Catalysis*, 2005, **234**, 172–181.

[16] O. Dulub, W. Hebenstreit and U. Diebold, *Phys Rev Lett*, 2000, **84**, 3646–3649.

[17] D. S. Humphrey, G. Cabailh, C. L. Pang, C. A. Muryn, S. A. Cavill, H. Marchetto, A. Potenza, S. S. Dhesi and G. Thornton, *Nano Lett*, 2009, **9**, 155–159.

[18] K. Hansen, T. Worren, S. Stempel, E. Laegsgaard, M. Baumer, H. Freund, F. Besenbacher and I. Stensgaard, *Phys Rev Lett*, 1999, **83**, 4120–4123.

[19] I. Yudanov, R. Sahnoun, K. Neyman, N. Rosch, J. Hoffmann, S. Schauermann, V. Johanek, H. Unterhalt, G. Rupprechter, J. Libuda and H. Freund, *J Phys Chem B*, 2003, **107**, 255–264.

[20] S. Schauermann, V. Johanek, M. Laurin, J. Libuda and H. Freund, *Phys Chem Chem Phys*, 2003, **5**, 5139–5148.

[21] K. Hansen, Z. Sljivancanin, E. Laegsgaard, F. Besenbacher and I. Stensgaard, *Surf Sci*, 2002, **505**, 25–38.

[22] J. Silvestre-Albero, G. Rupprechter and H. Freund, *Chem Commun*, 2006, 80–82.

[23] M. Morkel, G. Rupprechter and H. Freund, *Surf Sci*, 2005, **588**, L209–L219.

[24] V. Johanek, S. Schauermann, M. Laurin, C. Gopinath, J. Libuda and H. Freund, *J Phys Chem B*, 2004, **108**, 14244–14254.

[25] S. Schauermann, J. Hoffmann, V. Johanek, J. Hartmann, J. Libuda and H. Freund, *Angew Chem Int Edit*, 2002, **41**, 2532.

[26] W. Ludwig, A. Savara, S. Schauermann and H. J. Freund, *Chem. Eur. J. of Chem. Phys.*, 2010, **11**, 2319–2322.

[27] R. Nyholm, J. N. Andersen, U. Johansson, B. N. Jensen and I. Lindau, *Nucl Instrum Meth A*, 2001, **467**, 520–524.

[28] P. Stone, S. Poulston, R. Bennett and M. Bowker, *Chem Commun*, 1998, **13**, 1369–1370.

[29] Q. Fu, T. Wagner, S. Olliges and H. Carstanjen, *J Phys Chem B*, 2005, **109**, 944–951.

[30] M. Nolan, S. D. Elliott, J. S. Mulley, R. A. Bennett, M. Basham and P. Mulheran, *Phys Rev B*, 2008, **77**, 235424.

[31] *Practical Surface Analysis*, ed. D. Briggs and M. P. Seah, John Wiley and Sons Ltd, England, 2nd edn., 1990, vol. 1.

[32] C. J. Powell and A. Jablonski, *NIST Electron Inelastic-Mean-Free-Path Database - Version 1.2*, National Institute of Standards and Technology, Gaithersburg, MD, The USA, 2010.

[33] J. Stohr, *NEXAFS Spectroscopy*, Springer-Verlag, Heidelberg, 1992, vol. 25.

[34] J. Stohr and D. Outka, *Phys Rev B*, 1987, **36**, 7891–7905.

[35] P. Stone, R. Bennett, S. Poulston and M. Bowker, *Surf Sci*, 1999, **433**, 501–505.

[36] M. Ball, C. Lucas, N. Markovic, V. Stamenkovic and P. Ross, *Surf Sci*, 2002, **518**, 201–209.

[37] M. Han, P. Mrozek and A. Wieckowski, *Phys Rev B*, 1993, **48**, 8329–8335.

[38] M. Rose, T. Mitsui, J. Dunphy, A. Borg, D. Ogletree, M. Salmeron and P. Sautet, *Surf Sci*, 2002, **512**, 48–60.

[39] M. Ø. Pedersen, M. L. Bocquet, P. Sautet, E. LÊgsgaard, I. Stensgaard and F. Besenbacher, *Chemical Physics Letters*, 1999, **299**, 403 – 409.

[40] H. Unterhalt, G. Rupprechter and H. Freund, *J Phys Chem B*, 2002, **106**, 356–367.

[41] C. Xu, X. Lai, G. Zajac and D. Goodman, *Phys Rev B*, 1997, **56**, 13464–13482.

[42] A. A. Schmidt, H. Eggers, K. Herwig and R. Anton, *Surface Science*, 1996, **349**, 301–316.

[43] T. Mitsui, M. Rose, E. Fomin, D. Ogletree and M. Salmeron, *Science*, 2002, **297**, 1850–1852.

[44] R. A. Bennett, C. L. Pang, N. Perkins, R. Smith, P. Morrall, R. Kvon and M. Bowker, *J Phys Chem B*, 2002, **106**, 4688–4696.

Chapter 6

Probing the Oxygen Reactivity and Electronic Structure of the Cross-linked TiO_2(110)-(1×2) Surface

Abstract

The adsorption of O_2 on the cross-link reconstructed TiO_2(110)-(1×2) surface was investigated with XPS, UPS and STM. Spectroscopically, the adsorption of a small amount of O_2 results in a drastic quench of the Ti^{3+} species at the topmost layer of the (1×2) surface, a huge reduction in the density of the Ti^{3+} derived defect state in the band gap, and a noticeable rise in the surface workfunction (Φ). This also leads to a saturation of the (1×2) strands on the surface by O_2 molecules and their related features, which predominantly adsorb on the centre of the strands.

CITS was also performed on the cross-link reconstructed TiO_2(110)-(1×2) surface at 78 K. The result shows that the densities of the two occupied states, one at -0.7 V and another at -1.3 V, vary between the atomic rows on the strands, the region near the rows on the strands, and the dark region between strands. This also illustrates that although there are a lower densities of the occupied states than the strands and the dark region in between,

the cross-links possess an empty state peak at 1.2 V which cannot be detected anywhere else on the surface. The occupation of the centre of the cross-links by adsorbates (possibly H_2O) lead to reduction in the density of the occupied state at -0.7 V together with an emergence of an empty state at 1 V, serving as the signature of that adsorbate.

6.1 Motivation

Metal oxides have been widely studied due to their importance in numerous technological applications such as photocatalysis, heterogeneous catalysis, light harvesting, and gas sensing. Among these metal oxides, rutile titania and in particular its most stable (110) face, serves as a model substrate to explore the surface physics and chemistry of metal oxides in general [1, 2].

The geometric structure of the TiO_2(110)-(1×1) surface is well understood. It consists of alternating rows of fivefold coordinated Ti^{4+} ions and two-fold coordinated bridging O^{2-} ions. Rutile TiO_2 is a wide band-gap insulator which can be made into a semi-conductor upon reduction by ion sputtering and vacuum annealing. This sample preparation results in the creation of oxygen vacancies, including bridging O vacancies (O_b vac) at the surface and Ti interstitials in the near-surface region [1, 3, 4].

However, the precise nature of the (1×2) reconstruction, which is a reduced phase of the TiO_2(110) surface, remains unresolved. Previous studies of highly reduced TiO_2(110) reveal characteristic strands in the [001] direction with a minimum spacing of 1.3 nm [5–7]. These strands are formed upon reduction by high temperature annealing (∼1000 K) [7], while their formation upon oxidation of the (1×1) surface at moderate temperature has also been reported [6]. In their STM work on the TiO_2(110)-(1×2) surface, Bennett *et al.* observed that there were two types of (1×2) strands: the dark strands (DS) and bright strands (BS) present on the surface [7]. As shown in Figure 6.1, the dark strands (DS) were measured to have a corrugation of ∼1.3 Å while the bright strands were measured to have a corrugation of ∼2.8 Å. Based on the difference in corrugation, Bennett *et al.* classified the (1×2) reconstruction into two types: the p-(1×2) reconstruction, which corresponds to the dark strands (DS) in STM (Figure 6.1), and the c-(1×2) reconstruction, corresponding to the bright strand (BS) features. The p-(1×2) reconstruction usually appears as individual double-row strands on the terraces of TiO_2(110), while the c-(1×2) reconstruction is normally present as a patch of strands inter-connected by single and cross-links [7, 8]. In addition to the expected (1×2) ordering, the arrangement of the

cross-links on the c-(1×2) reconstructed surface results in an additional (12×2) ordering as detected in LEED and STM [7].

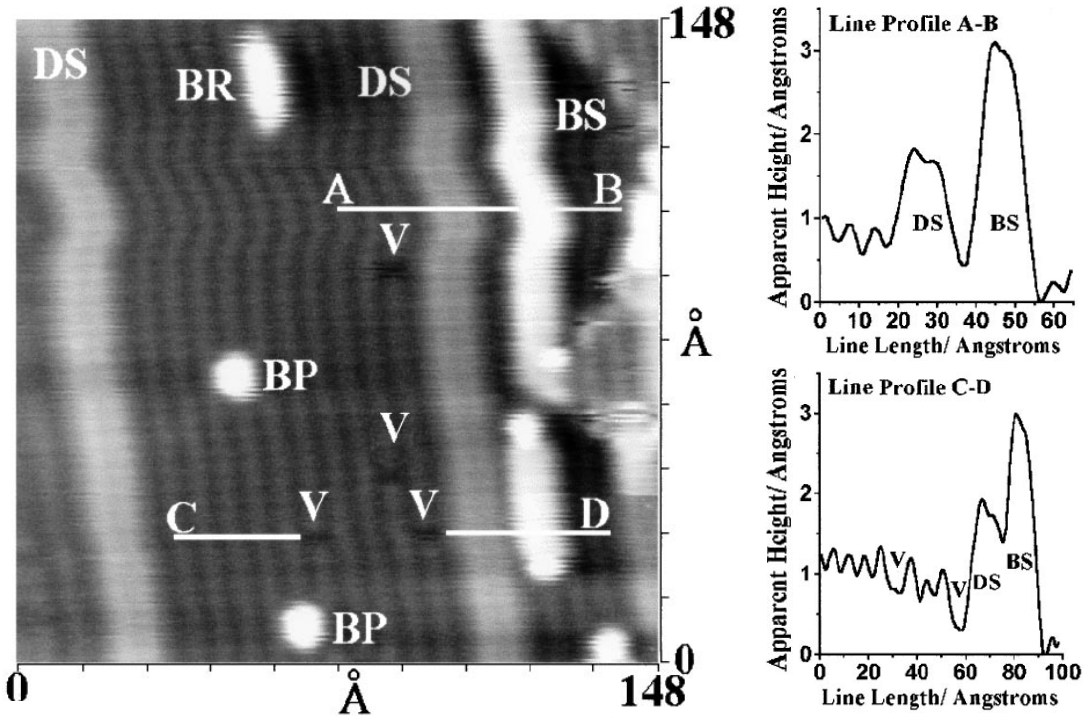

Figure 6.1: STM image of the non-stoichiometric TiO_2(110) surface in the middle of the reaction with O_2 at 833 K [7]. The features marked are dark strands (DS), bright strands (BS), bright points (BP), bright rows (BR) and bridging oxygen vacancies (V). Line profiles AB and CD, which are plotted on the right, show that the dark strands (DS) and bright strands (BS) are measured to have heights of 1.3 Å and 2.8 Å respectively. Based on the measured corrugations of both features, it was proposed that the dark strands (DS) correspond to the added Ti_2O_3 row model [5] while the bright strands (BS) correspond to the added Ti_3O_6 row model [7]. Both the Ti_2O_3 and Ti_3O_6 models are illustrated in Figures 6.2(b) and (c), respectively. Figure reproduced with permission from [7]

Based on the observations in LEED and STM, several models have been proposed to explain the atomic structure of the (1×2) reconstructions. The most widely accepted model is the added row model with Ti_2O_3 stoichiometry, proposed by Onishi *et al.* [5]. In this model, oxygen atoms are in the same positions as in the TiO_2 substrate but the Ti atoms in the (1×2) strands are only four-fold coordinated and form a distorted tetrahedral arrangement. This model was favoured in explaining the (1×2) strands in STM measurements [5–7], and also compatible with the LEED-IV calculations [9]. In addition, total energy calculations show that this configuration is stable [10, 11]. Another notable model is the added row Ti_3O_6 model proposed by Bennett *et al.* [7], which is a modified version

of the added row Ti_3O_5 model proposed by Pang *et al.* [12]. In this model, added rows of stoichiometric Ti_3O_6 motifs are centred on alternating five-fold coordinated Ti rows. The added row Ti_3O_6 model is predicted to have a higher surface energy than the added row Ti_2O_3 model, and hence, is not expected to form on stoichiometric TiO_2. However, on the reduced surface the situation is uncertain. Furthermore, it is conceivable that the preparation conditions may influence the structure and composition of the (1×2) strands. Although the added row Ti_3O_6 model has been shown to be inappropriate for explaining the p-(1×2) reconstruction [9], one still cannot rule out the possibility that this model is good at explaining the c-(1×2) reconstruction. In fact, based on the corrugations of the bright strands (BS) and dark strands (DS) measured in STM (Figure 6.1), Bennett *et al.* assigned the p-(1×2) reconstruction to Ti_2O_3 added rows and the c-(1×2) reconstruction to Ti_3O_6 added rows [7]. Lately, an NC-AFM study by Pieper *et al.* [13] suggested that the Ti_3O_6 added row model is best at explaining the image contrast on the cross-linked TiO_2-(1×2) surface.

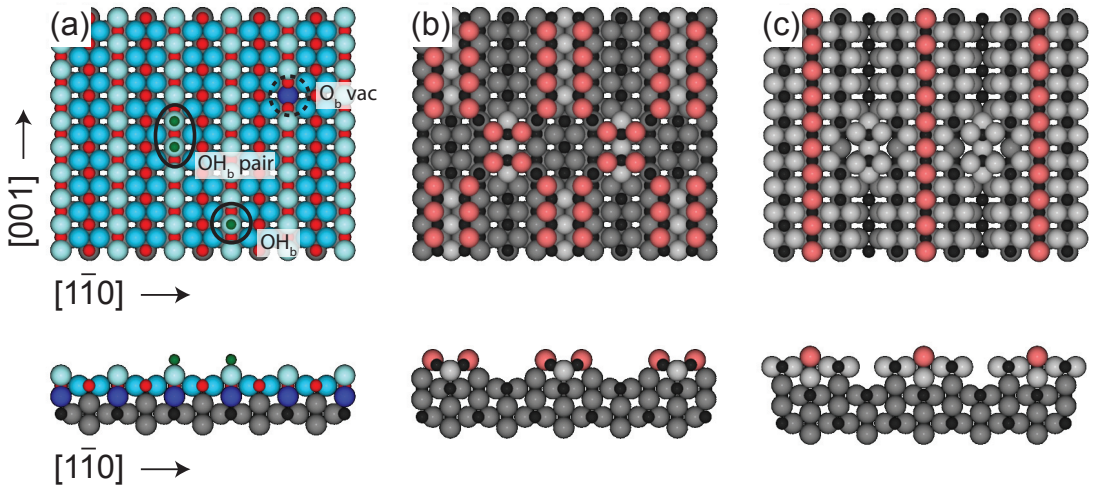

Figure 6.2: (a) Model of the TiO_2(110)-(1×1) surface, on which a bridging oxygen vacancy, $O_b vac$, a bridging hydroxyl, OH_b, and a pair of OH_b are marked. (b) and (c) are added row models for the cross-linked (1×2) reconstructed TiO_2(110)-(1×2) surface based on (b) Ti_2O_3 and (c) Ti_3O_6 units. Small circles denote titanium atoms, while large circles denote oxygen atoms. The different degree of shading indicates the association of an atom to a specific surface layer.

Apart from LEED-IV, scanning tunnelling spectroscopy (STS) has also been used to probe

the local electronic structure of the cross-linked TiO_2(110)-(1×2) surface in order to determine its geometric structure. By performing STS on the (1×2) surface, Murray *et al.* [8] discovered that the dark rows between the (1×2) strands have higher filled defect states than the (1×2) strands, which then have higher filled defect states than the cross-links. Additionally, as pointed out by Klusek *et al.* in their STS work [14], those filled defect states correspond to two separate Ti^{3+} $3d$ derived states, namely d state and D state, located at 0.7 eV and 1.5 eV below E_F and varying in size with different locations on the surface. Based on the above findings, and also by considering that the atomic configuration on the surface has a decisive impact on the spatial distribution of the surface states, it is possible that by using CITS to probe the LDOS at every point on the surface and comparing the results with the calculations, one can determine which (Ti_2O_3 or Ti_3O_6) is the best model for explaining the cross-link (1×2) reconstruction on the TiO_2(110) surface.

Besides investigating its geometric structure, there were a number of studies which employed the TiO_2(110)-(1×2) surface as a platform to study the properties of thin films (such as silica) or metal particles (such as Au, Ag, Rh, Ir) grown on it [15–19]. On the other hand, research which focuses on the chemical reactivity of the TiO_2(110)-(1×2) surface are still lacking. Until now there were only a few groups studying the adsorption of simple molecules on the (1×2) surface [20–24]. This is in stark contrast to the case of the un-reconstructed TiO_2(110) surface, on which the adsorptions of simple molecules such as H_2O and O_2 are well understood [2]. In order to fill up this knowledge gap, more work on the adsorption behaviour of different molecules on the TiO_2(110)-(1×2) surface are necessary.

This chapter is divided into two parts. Firstly, we have studied the adsorption of O_2 on the (1×2)-reconstructed TiO_2(110) surface at 300 K with UPS, XPS and STM. In the second part, by performing current imaging tunnelling spectroscopy (CITS) measurements at 78 K, we have resolved the local density of states (LDOS) of different features on the cross-linked (1×2) TiO_2(110) surface.

6.2 Experimental

The experiments were carried out using an *Omicron GmbH* Low Temperature STM housed in a UHV system at a base pressure of 2×10^{-11} mbar. The adjoining preparation chamber was equipped with a sputter gun and heater for sample preparation, and facilities for LEED and XPS/UPS measurement.

The TiO_2(110)-(1×2) surface was prepared by cycles of argon ion sputtering (1 kV) and annealing to 1100 K in UHV until a well-ordered TiO_2(110)-(1×2) diffraction pattern was observed in LEED and no impurities such as Ca or C were detected in XPS. For the O_2 adsorption experiment, research grade O_2 (99.996 %, *Laborgase*) was dosed into the UHV chamber by backfilling through a leak-valve.

XPS spectra were taken at normal emission with Al Kα ($h\nu$ = 1486.6 eV) as a photon source. All Ti 2p spectra were recorded at a pass energy of 10 eV. UPS He I ($h\nu$ = 21.2 eV) spectra were taken at normal emission and a pass energy of 9 eV. The surface work function Φ was measured by means of photon-induced secondary electron emission from surfaces, which were negatively biased (-V) [25]:

$$\Phi = E_0^{kin} + \Phi_{SP} - eV \tag{6.1}$$

where Φ_{SP} is the work function of the spectrometer and E_0^{kin} the onset energy of the secondary electron emission spectra.

The STM images were taken at constant current mode at 300 K (for O_2 adsorption experiment) and 78 K (during CITS) with electrochemically etched tungsten tips, which were conditioned by UHV annealing to 400 K and by tip pulses during scanning. Current imaging tunnelling spectroscopy (CITS) data was recorded at 78 K. Each CITS dataset contained 100×100 $I-V$ curves, which were recorded at each pixel by ramping the sample voltage from +1.6 V to -2.4 V at intervals of 0.1 V while monitoring the current. When recording an $I-V$ curve, both the delay and acquisition time for each datapoint were set

at 640 μs. During CITS, a topography image was obtained at the sample bias of +0.9 V and current of 0.15 nA. This image served as a guide to correlate the $I-V$ spectra with their corresponding features on the surface. dI/dV spectra were obtained by numerically differentiating the $I-V$ spectra after acquisition.

6.3 Results and Discussions

6.3.1 Effect of H_2O on the Cross-linked TiO_2(110)-(1×2) Surface

The effect of H_2O adsorption on the cross-linked TiO_2(110)-(1×2) surface was examined using UPS and STM. This was achieved by performing UPS He I measurement on the as-prepared cross-linked TiO_2(110)-(1×2) surface and the surface after being left in the UHV system at a base pressure of $\sim 3 \times 10^{-11}$ mbar for 48 hours. Using a quadrupole mass-spectrometer, the partial pressure of H_2O was measured to be $\sim 2 \times 10^{-11}$ mbar, meaning that there were in total ~2.6 langmuirs (1 langmuir = 1.33×10^{-6} mbar·s) of H_2O molecules impinging on the surface. The surface was also imaged in STM following H_2O adsorption.

As shown in Figure 6.3(a), the valence band spectrum of the as-prepared cross-linked TiO_2(110)-(1×2) surface (curve i) consists of a secondary electron tail on the higher binding energy (BE) side, O $2p$ derived states at ~5.5 and ~7 eV, and a Ti^{3+} $3d$ derived state located at ~1 eV below the Fermi level (E_F). By comparing the lineshape and the energy position of the O *2p* band, it is concluded that there is almost no change in the valence band structure before and after H_2O adsorption. The inset of 6.3(a) displays the spectra taken in the band-gap state region. By numerically fitting each spectrum using a 3rd-order polynomial and a Gaussian lineshape, which account for the background and the band-gap state peak respectively, the area of the band-gap state peak of the as-prepared surface was calculated to be 104.4 ± 20.5 (in arbitrary units), which slightly decreases to 78.9 ± 16.6 after H_2O adsorption. Within error, it is concluded that the adsorption of H_2O only has a *minor* effect on the band-gap state of the cross-linked TiO_2(110)-(1×2) surface.

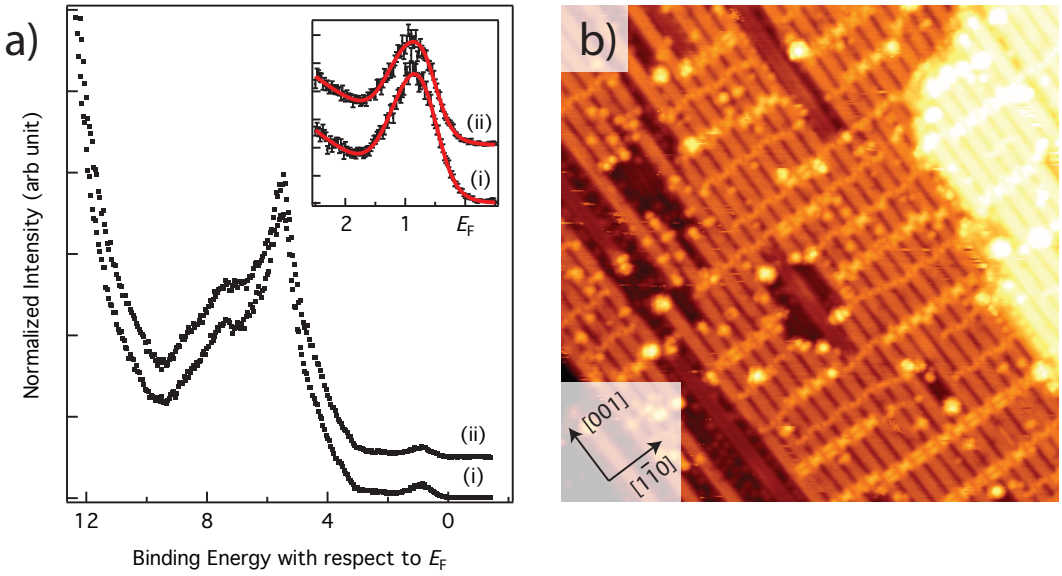

Figure 6.3: (a) Photoemission He I ($h\nu = 21.2$ eV) spectra taken from (i) the as-prepared cross-linked TiO_2(110)-(1×2) surface and (ii) the same surface after being left in the UHV chamber (base pressure of $\sim 3 \times 10^{-11}$ mbar) for 48 hours. The inset: the spectra recorded in the region of the band-gap, where black dots are the experimental data and red lines the corresponding numerical data. The area of the band-gap state peak of the surface following H_2O adsorption is calculated to be 78.9 ± 16.6, slightly smaller than that of the as-prepared surface, 104 ± 20.5. (b) A STM picture taken from the surface corresponding to Curve (ii) in (a). (50×50 nm^2, 1.5 V, 0.05 nA).

The STM image of the surface following H_2O adsorption is shown in Figure 6.3(b), together with the corresponding analysis displayed in Figure 6.4. This reveals a number of bright spots located at different sites on the cross-linked TiO_2(110)-(1×2) surface. They are the bright spots at the centre of the (1×2)-strands (marked by squares, hereon referred to as feature A), the bright spots at the side of the strands (marked by circles, hereon referred to as feature B), and the extra-bright spots at the terminations of the strands (marked by triangles, hereon referred to as feature C). Features A, B and C are measured to have heights of 1.3 ± 0.3 Å, 0.6 ± 0.2 Å and 2.9 ± 0.6 Å respectively. As for feature C, even on the clean TiO_2(110)-(1×2) surface, the terminations of the strands often appear much brighter than other sites on the surface [26], and this is due to under-coordination of the Ti species on the terminations. As for the bright features on the strands, Features A always appear brighter than Features B. This variation in brightness might arise from the difference in physical size, electronic state population, or a combination of both. Here we postulate that Features A originate from bigger-sized molecules and Features B from

smaller-sized molecules. However, to determine the actual sizes and composition of those features, theoretical calculations are required.

In order to figure out the origins of Features A and B, we refer to the case of the TiO_2(110)-(1×1) surface on which water is known to fill the O_b vac at a temperature above 187 K resulting in a pair of bridging hydroxyls (OH_b) [27, 28]. The O_b vac, OH_b, and OH_b pairs on the hydroxylated TiO_2(110) surface were measured to have heights of 0.5 Å, 0.8 Å and 1.2 Å respectively [27–29]. Although the reaction mechanism of water on the cross-linked TiO_2(110)-(1×2) surface is not fully understood, by comparing the measured heights with those reported on the TiO_2(110)-(1×1) surface, it is suggested that features A correspond to OH_b pairs and features B to single OH_b.

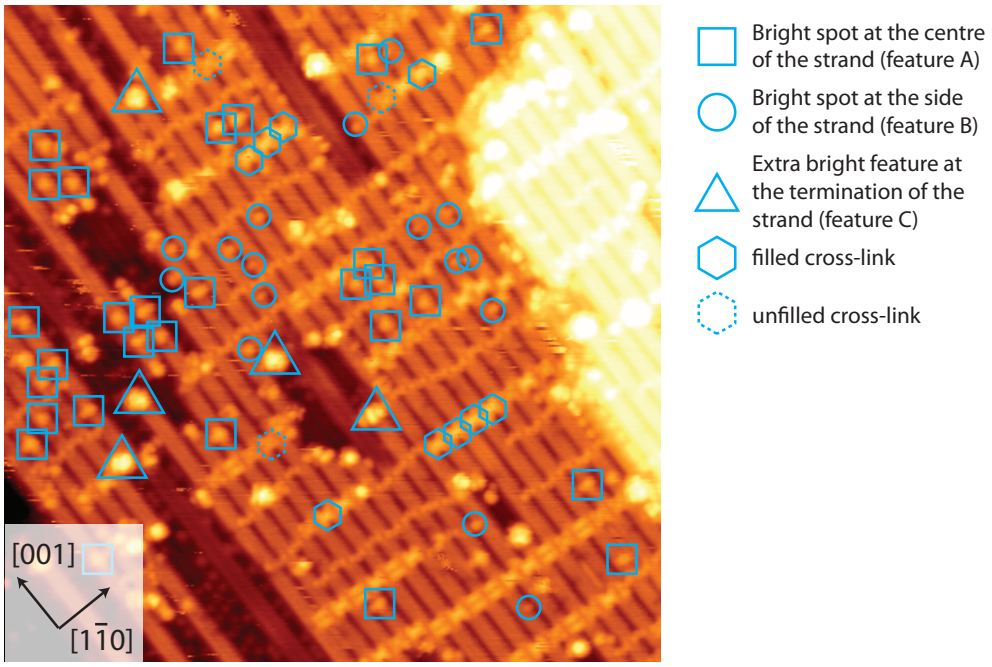

Figure 6.4: The same STM picture as in Figure 6.3(b) with all H_2O and its related features marked by different symbols. They are the bright spots at the centre of the (1×2) strands (squares, referred to as Features A), the bright spots at the side of the strands (circles, referred to as Features B), and the extra bright spots at the termination of the strands (triangles, referred to as Features C). The "filled" and "empty" cross-links are marked by solid and dashed hexagons respectively.

The effect of H_2O on the cross-links was also examined. Based on their brightness in STM, the cross-links can be classified into two types: brighter and less-bright cross-links (marked by solid and dashed hexagons respectively in Figure 6.4). The former, whose

number increased with time, are assigned to those filled by gas molecules (probably H_2O) from the residual vacuum, and the latter correspond to the empty cross-links. The filled cross-links are measured to have height of 1.6 ± 0.1 Å while the empty have height of 1.0 ± 0.1 Å. Note the height of all features are measured from the centre of the bare (1×2)-strands. In addition to this, closer look into the filled cross-links reveals that while some are brighter at their centres, other appear brighter around the circumferences. A deeper investigation is required in order to understand their difference in appearance.

The adsorption of H_2O on the TiO_2(110)-(1×2) surface results in bright features of various sizes resting on different sites on the surface in STM, but only causes a slight reduction in the density of the band-gap state as detected in UPS. These findings will be useful for the study of O_2 adsorption on the (1×2) surface, which will be discussed in the next section.

6.3.2 O_2 Adsorption on the TiO_2(110)-(1×2) Surface

The adsorption of O_2 on the cross-linked TiO_2(110)-(1×2) surface was studied spectroscopically and microscopically. In the spectroscopic measurement, the as-prepared cross-linked TiO_2(110)-(1×2) surface was exposed to various amounts of O_2 at 300 K, and examined with XPS and UPS. As indicated in the XPS Ti $2p_{3/2}$ spectra in Figure 6.5, the primary peaks are at the binding energy (BE) of 459.1 eV and have a shoulder peak at 457.3 eV, corresponding to Ti^{4+} and Ti^{3+} states respectively. The separation of the Ti^{4+} and Ti^{3+} peaks reported here (1.8 eV) is compatible with the value of 1.9 eV reported by Nolan *et al.* [30]. When conventional XPS is employed, the shoulder peak is visible on the (1×2) surface, but is hardly observed on the (1×1) surface [31]. However, when synchrotron radiation XPS is used, due to its enhanced surface sensitivity, one can observe a small shoulder peak on the (1×1) surface and a much larger peak on the (1×2) surface. These Ti^{3+} species result from the (1×2) reconstruction at the topmost surface layer. Upon oxidation, the shoulder peak declines quickly and reaches its saturation level at an O_2 exposure of ∼1 L, suggesting that all the Ti^{3+} species on the topmost layer react with O_2 and convert to Ti^{4+}. After that, there is no noticeable change in the spectral lineshape

up to an oxygen exposure of 100 L

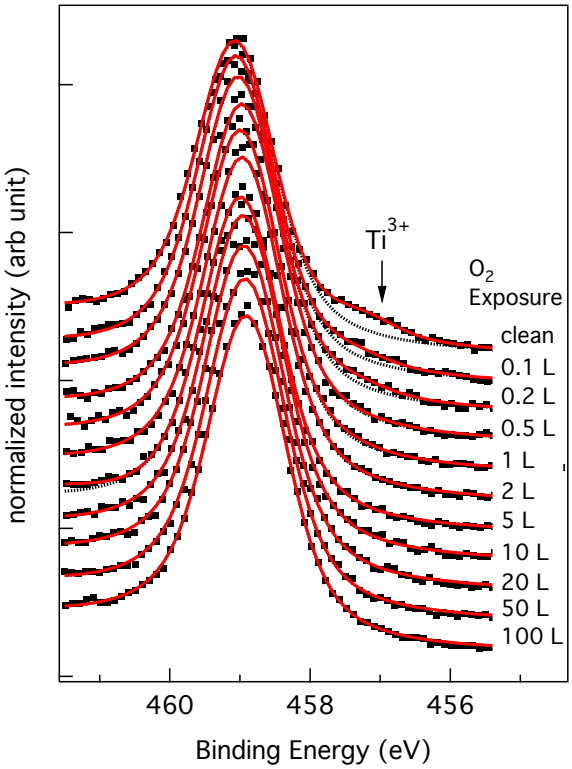

Figure 6.5: XPS Ti $2p$ spectra (Al $K\alpha$, $h\nu = 1486.6$ eV) taken from the cross-linked TiO_2(110)-(1×2) surface at different O_2 exposure at 300 K. Spectra were recorded at normal emission, with pass energy of 10 eV. Only the region of the $2p_{3/2}$ peak is shown. This shows that the population of the Ti^{3+} state declines quickly upon oxidation and reaches its saturation value at an O_2 exposure of $\sim$1 L.

The corresponding UPS He I results are displayed in Figure 6.6. As previously discussed, the valence band spectrum of the as-prepared (1×2) surface consists of a secondary electron tail on the higher BE side, O $2p$ derived peaks at $\sim$5.5 and $\sim$7.0 eV, and a Ti^{3+} $3d$ derived defect state located at $\sim$1 eV below E_F in the band gap. At an O_2 exposure of $\sim$ 1 L, the defect state declines rather quickly, together with a shift of the O $2p$ band towards E_F, as a result of band-bending. Additional O_2 exposure leads to further decrease in the defect state and the corresponding shift of the O $2p$ band towards E_F.

To quantify the effect of O_2 on the (1×2) surface, we recorded UPS spectra near the band-gap state peak at various O_2 exposure, and the results are shown in Figure 6.7(a). The data are numerically fitted and from the fittings the area of the band-gap state peak

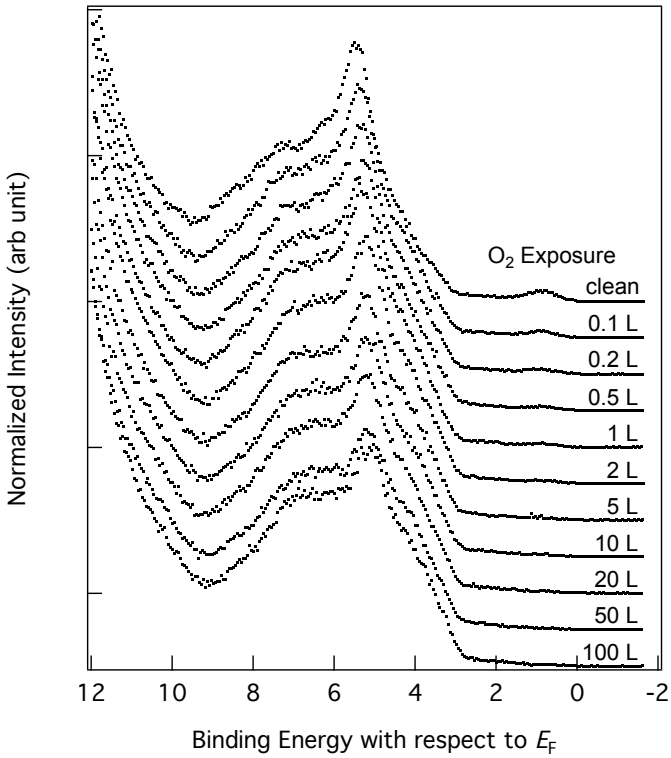

Figure 6.6: Photoemission He I ($h\nu = 21.2$ eV) spectra recorded from the cross-linked TiO_2(110)-(1×2) surface as a function of O_2 exposure at 300 K. Spectra are vertically offset for clarity.

at various O_2 exposures are calculated. As shown in Figure 6.7(b), the band-gap state peak decreases in intensity with O_2 exposure: at 0.1 L it is 55 % of that on the as-prepared surface and by 0.5 L it is down to 25 %. After that, the band-gap state peak decreases in intensity at a much slower rate, and is almost completely quenched for exposures $\geq$ 50 L.

The change in the surface workfunction upon O_2 exposures was also monitored. As shown in the inset of Figure 6.7(b), the as-prepared (1×2) surface has a surface workfunction of 4.67 ± 0.05 eV, which then rises to 4.97 ± 0.05 eV at an O_2 exposure of 0.5 L. After that, the workfunction increases further at a lower rate with O_2 exposures until it saturates to a value of 5.03 ± 0.05 eV at 100 L.

To gain better understanding on how O_2 reacts with the (1×2) surface, we compare our results to those collected from the oxidation experiments performed on the as-prepared TiO_2(110)-(1×1) surface. This surface consists of alternating fivefold-coordinated Ti and twofold-coordinated O rows running along the [001] direction, and bridging O vacancies

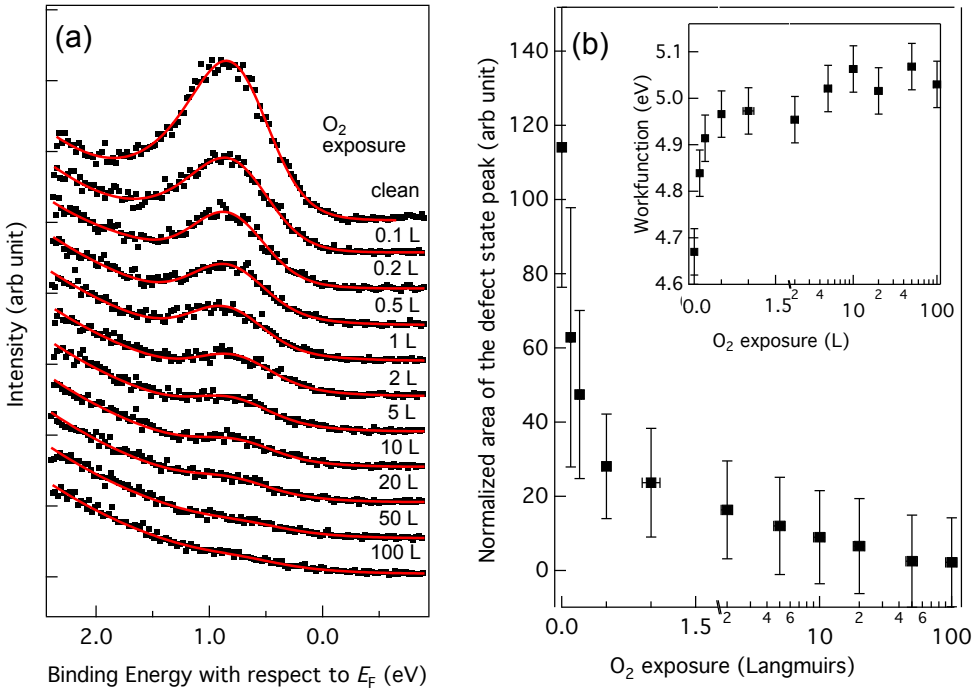

Figure 6.7: (a) UPS He I ($h\nu = 21.2$ eV) spectra recorded in the region of the band-gap from the cross-linked TiO_2(110)-(1 × 2) surface at various O_2 exposures. Black dots are the experimental data and red lines the numerical fits, from which the areas of the defect state peak are calculated. The spectra are offset for clarity. (b) A corresponding plot of area of the defect state peak as a function of O_2 exposure. Inset shows the work function of the surface as a function of O_2 exposures.

(O_b vac), which are known to be the active sites for chemical reactions [27, 28, 32], and were shown to have major contribution to the defect state [33]. Employing synchrotron UPS, Kurtz *et al.* [34] reported that on the as-prepared TiO_2(110)-(1×1) surface, the intensity of the defect state declined by half at an O_2 exposure of 1 L. In a more recent experiment, Wendt *et al.* [35] reported a decline in the band-gap state intensity by only ∼20 % at O_2 exposure of ∼2 L. Although the population of the defect states on the (1×1) surface is much less than that on the (1×2) surface [36], the above findings do suggest that O_2 reacts differently on the (1×1) and (1×2) surfaces.

STM was also used to study the adsorption of O_2 on the TiO_2(110)-(1×2) surface. In attempt to identify the adsorption sites of O_2 and its related molecules on the (1×2) surface, only a very small amount of O_2 was introduced onto the surface. Figures 6.8(a) and (b) display the STM pictures taken from the (1×2) surface before and after 0.01 L of O_2 exposure, showing that there are a number of features of varying brightness sitting

at different sites on the surface following an O_2 exposure of 0.01 L. These include bright features at the centre of the (1×2)-strands (marked by squares) and having a height of 1.2 ± 0.1 Å, as well as bright and less-bright features at the side of the strands (marked by solid and dashed circles, respectively) and having heights of 1.5 ± 0.3 Å and 0.3 ± 0.2 Å, as well as the bright features each of which rests nearby the corners of two cross-links (marked by triangles) and has a height of 1.0 ± 0.1 Å. In addition, there are a number of cross-links appearing much brighter than before O_2 dosing, and they are measured to have a height of 1.8 ± 0.1 Å. Note that the height of all features were measured from the centre of the bare (1×2)-strands.

In an STM study of the O_2 reaction on the hydroxylated TiO_2(110)-(1×1) surface, Du *et al.* [37] reported that the oxygen adatoms (O_a), HO_2 and terminal hydroxyls (OH_t) species, all of which adsorb at top of the Ti_{5c} ions, are measured to have heights of 0.3 Å, 0.5 Å, 0.9 Å respectively. In our experiment, the bright spots sitting at the (1×2) strands have heights of at least 1.2 Å. This implies that those bright spots might originate from bigger molecules such as molecular O_2, while the less bright spots, which are at the side of the strands and having a height of 0.3 ± 0.2 Å, might correspond to the O-adatoms or HO_2 species. Also, due to the similar appearance of the bright spots on both the oxidised surface and the surface following H_2O adsorption, it is still uncertain that whether the bright spots originate from O_2 and H_2O. In order to distinguish the features resulting from O_2 adsorption, an increasing amount of O_2 was introduced and the STM results are shown in Figure 6.9.

Due to a sudden change of the tip, we were unable to continue the STM measurement on the same area as in Figure 6.8. As a result of this, we restarted the measurement at the other area, and this is shown in Figure 6.9(a). However, due to a less-sharp tip, the STM pictures acquired in this case were not as good in quality as those in Figure 6.8. Even so, from those pictures it is still possible to identify where on the (1×2)-strands the O_2-related features are bound.

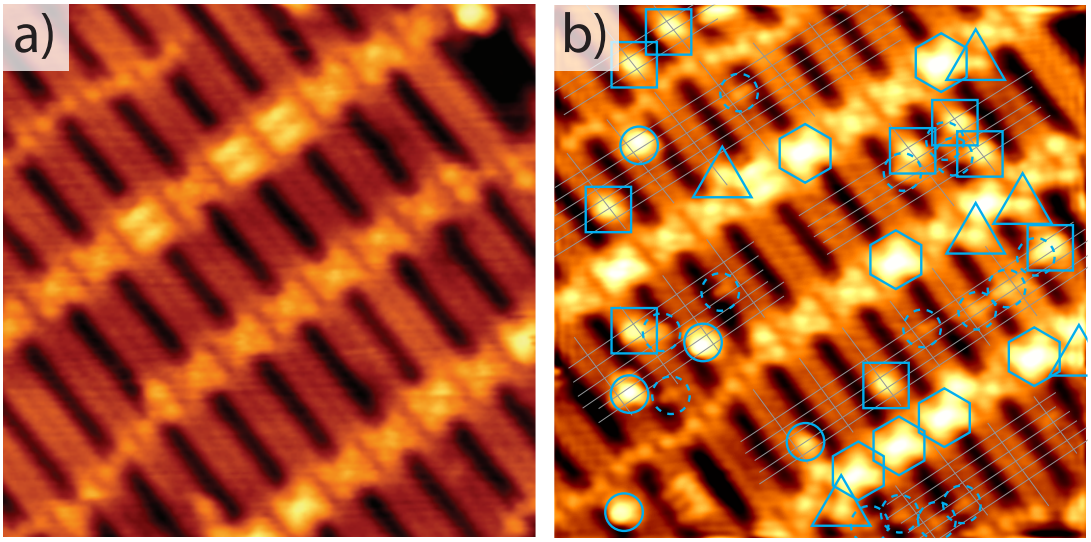

Figure 6.8: STM images recorded from the as-prepared TiO_2(110)-(1×2) surface before (a) and (b) after 0.01 L of O_2 exposure (15×15 nm^2, 1.2 V, 0.02 nA). Features present following O_2 exposure are marked differently in (b). They are the bright features at the centre of the strands (squares), the bright and less bright features sitting on the side of the strands (solid and dashed circles, respectively), the bright features nearby the corners of two cross-links (triangles), and the cross-links which appear much brighter than before O_2 exposure (hexagons).

Similar to that in Figure 6.8(b), the area shown in Figure 6.9(a) is also decorated with approximately the same amount of bright features. There are the bright and less-bright features at the centre of the (1×2)-strands (marked by solid and dashed squares respectively) and having heights of 1.4 ± 0.3 Å and 0.9 ± 0.5 Å respectively, as well as the bright and less-bright features at the side of the strands (marked by solid and dashed circles respectively) and having heights of 2.1 ± 0.1 Å and 0.6 ± 0.3 Å respectively. This indicates that the bright spots at the strands and having heights of at least 1.4 Å are probably molecular O_2, and the less bright spots having heights of $\sim$ 0.9 Å and $\sim$ 0.6 Å might correspond to the OH_t or HO_2 species as observed on the TiO_2(110)-(1×1) surface [37]. The surface was then exposed to increasing amounts of O_2. As shown in Figures 6.9(b) and (e), at 0.05 L, the surface is partially covered by the bright features located at the centre as well as at the side of the (1×2) strands. These bright features are measured to have the same heights as those observed at an O_2 exposure of 0.01 L (Figures 6.9(a) and (d)). On the other hand, the cross-links do not appear differently at 0.01 and 0.05 L of O_2 exposure. As shown in Figures 6.9(c) and (f), increasing the O_2 exposure to 0.1 L leads to all of the (1×2) strands on the surface completely saturated with the O_2 and its related

species, which preferably adsorb at the centre of the strands.

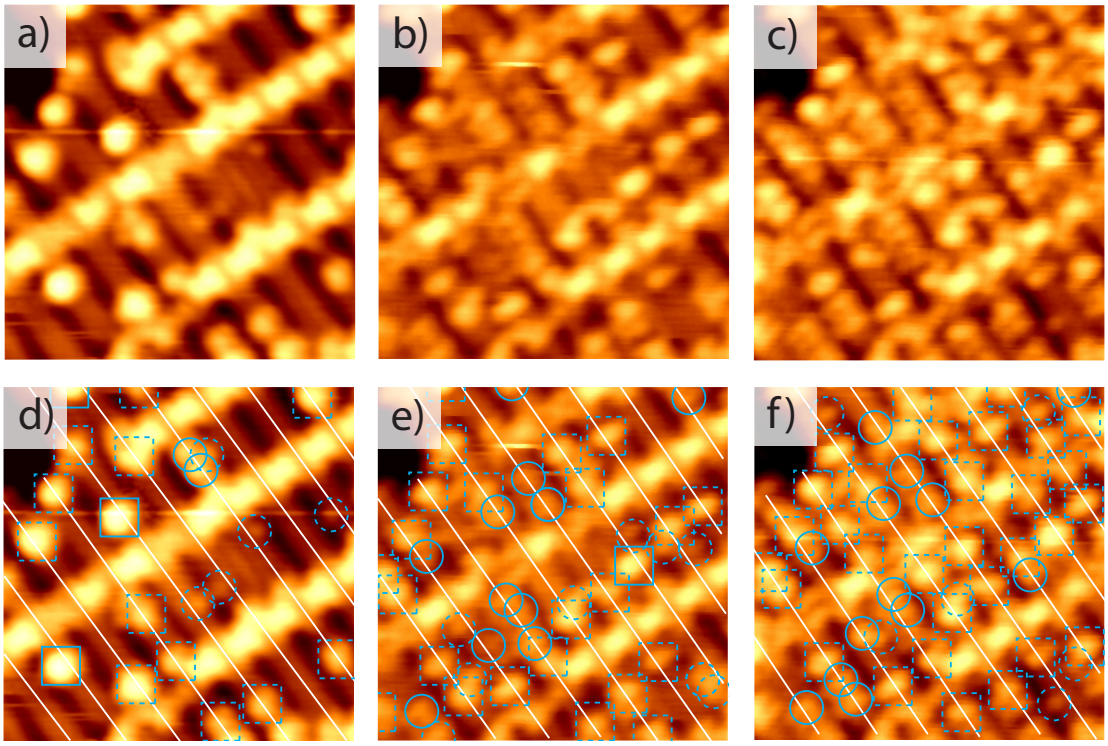

Figure 6.9: STM images (15×15 nm^2) recorded from the same area on the (1×2) surface following different O_2 exposures: (a) 0.01 L, (b) 0.05 L and (c) 0.1 L. (d), (e) and (f) are the same pictures where different features on the surface are marked. They are bright and less bright features at the centre of the (1×2)-strands (marked by solid and dashed squares respectively), and also the bright and less bright features at the side of the strands (marked by solid and dashed circles).

So far there have only been few studies devoted to the adsorption of simple molecules on the (1×2)-reconstructed TiO_2(110) surface [20–22]. Among those, Park *et al.* studied [20] the effect of O_2 on the individual (1×2)-strands present on the TiO_2(110) surface, and found that the adsorption of molecular O_2 leads to the creation of bright spots which agglomerate on or next to the individual (1×2) strands. Unlike round-protrusions of uniform shape which is usually observed for O atoms, many of the bright features had irregular shapes with some elongated along the [001] direction. In our case, at 0.01 L of O_2 exposure , we observe that the bright features at the centre of the (1×2) strands have a rather regular shape and height similar to that reported by Park *et al.* [20]. However, by comparing the STM pictures which were obtained following H_2O and O_2 adsorption respectively (Figures 6.4 and 6.8(b)), we found that the bright features arising from H_2O and O_2 appear quite

similar to each other. This means that in order to distinguish between H_2O, O_2 and their related products on the (1×2) surface, one needs to perform STM measurements in a more rigorous manner, and compare the results to those from the first principle calculations (if any). However, by increasing the amount of O_2, we did observe in STM that the (1×2) strands on the surface are covered with more and more bright features which preferably adsorb at the centre of the strands. This, together with the results in XPS and UPS, suggests that O_2 molecules adsorb at the centre of the (1×2)-strands, on which the Ti^{3+} species react with O_2 and convert to Ti^{4+}, resulting in a almost complete quench of the amount of the Ti^{3+} species, as deduced from the Ti 2p spectra, as well as a huge reduction in the density of the defect state in the band-gap. A swift increase in the surface work function upon small amounts of O_2 exposure also reflects the high reactivity between the O_2 molecules on the (1×2) strands as observed in STM.

6.3.3 Current Imaging Tunnelling Spectroscopy Measurements on the Cross-linked TiO_2(110)-(1×2) Surface

We performed current-imaging tunnelling spectroscopy (CITS) on the cross-linked TiO_2(110)-(1×2) surface in attempt to elucidate its geometric structure by comparison with calculations in the Shluger group. Following sample preparation the sample was checked to show sharp (1×2) diffraction spots in LEED and no contaminants in XPS, the as-prepared (1×2) surface was shipped to the STM stage for imaging and subsequent CITS measurement at 78 K. A STM picture taken from the as-prepared surface is shown in Figure 6.10(a). This reveals that the surface consists of terraces, on top of which the (1×2) strands are inter-connected by the single- and cross- features. In the figure, the region where CITS measurement was performed is marked by a blue square, and the corresponding atomically resolved image is shown in Figure 6.10(b). In the figure, it can be seen that each strand consists of three rows of bright spots running along the [001] direction. On each row, the bright spots are 3 Å apart from each other. On the central row, each bright spot is located at the centre surrounded by four bright spots, two on each of the side rows, leading to a rhombus configuration. As for the cross-link, it consists of bright spots at its four corners

and two spots of different brightness at the upper and lower side of its centre. Even on the freshly prepared surface, a smaller number of the cross-links appear brighter than other cross-links, probably resulting from adsorption of gas molecules (such as molecular water) from the residual vacuum.

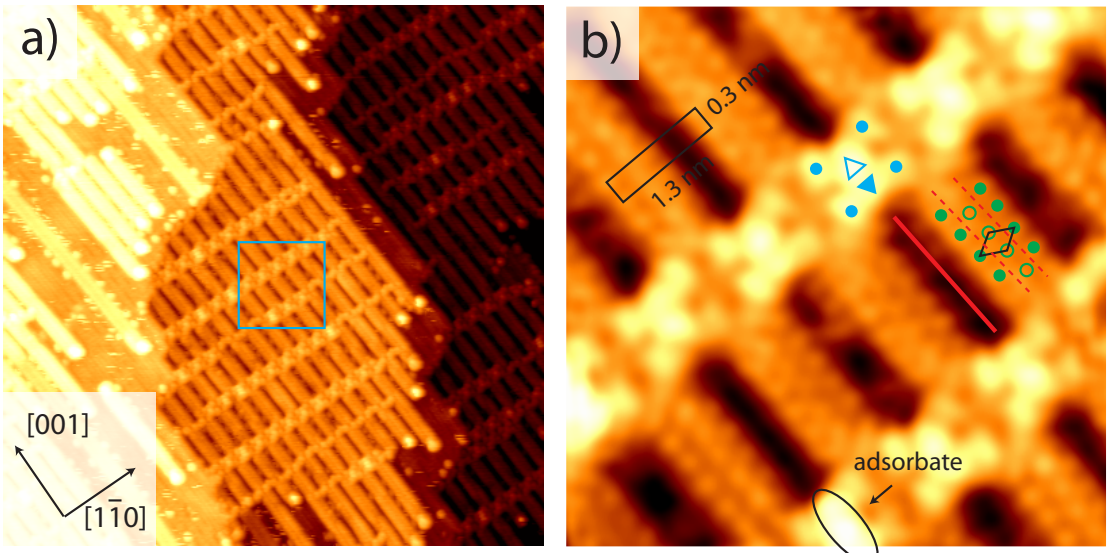

Figure 6.10: (a) A STM picture (39×39 nm^2) taken from the TiO_2(110)-(1×2) surface. (b) A zoomed-in picture (6×6 nm^2, 0.9 V, 0.1 nA) taken from the region marked by a blue square in (a), in which the atoms located at the central and side rows of a (1×2) strand are marked by green hollow and filled circles respectively. For the cross-links, the bright and less-bright features at their centres are marked by blue hollow and filled triangles respectively, and their corners marked by filled blue circles. The dark region between (1×2) strands and the region near the atomic rows on the strands are marked by red solid and dashed red lines, respectively. The cross-link covered with an adsorbate is indicated by a black circle.

Stability is the key factor for successful CITS. Therefore, prior to measurement, the STM was left scanning for hours until it scanned on exactly the same area for a long period of time (normally more than three hours) without experiencing any drift whilst the STM tip gave atomic resolution without any tip-changes. Rather than 400×400 (pixels)^2, which was used for imaging, CITS was performed with an image size of 100×100 (pixels)^2 so as to minimise the duration of each scan (a typical collection time for each CITS data was ∼2 hours). Performing CITS in this manner leads to a topographical picture together with 100×100 $I-V$ spectra, which altogether provide information on the local density of states (LDOS) at various locations on the surface.

The CITS data, which were recorded from the as-prepared TiO_2(110)-(1×2) surface, consists of a series of current maps recorded at different bias voltages, shown in Figure 6.11, and a topographical image, displayed in Figure 6.12(a). By also referring to the atomically-resolved STM image in Figure 6.10(b), it becomes plausible to locate all the features on the topographical as well as current maps. This is demonstrated in 6.12(b), showing that the current map, which was recorded at -0.7 V, is overlaid with the feature-markers used in the corresponding topographical picture.

To analyse the CITS data, we firstly selected approximately 50 tunnelling spectra recorded on the same feature and took the average. From the averaged $I-V$ curve, one can simply divide it by voltage to get the static conductivity curve ($\frac{I}{V}$) or differentiate it numerically to obtain the differential conductivity curve ($\frac{dI}{dV}$). By dividing the differential conductivity curve by its corresponding static conductivity curve, one gets the normalised conductivity curve ($\bar{\sigma}(V)$), which is representative of the local density of states [38]. Note that by definition, $\bar{\sigma}(V)$ equals unity at $V = 0$ [39].

Figure 6.13 illustrates the normalised conductivity curves of various features on the cross-linked TiO_2(110)-(1×2) surface. Firstly, the normalised conductivity curves of the central and side rows on the (1×2) strands (marked by green hollow and filled circles in Figure 6.12), the region nearby the rows of the strands (marked by red dashed lines), and the dark region between the strands (marked by red solid lines) are compared. As shown in Figure 6.13(a), all four curves share a few common characteristics. These include the two occupied states in the band gap, one at ~ -0.7 V and the other at ~ -1.5 eV and the plateau starting at 0.7 eV in the empty state region. In their room temperature STS work on the TiO_2(110) surface, Klusek *et al.* [40] assigned the occupied state at ~ -1.5 V to the d state, whose origin can be attributed to the presence of high density of Ti^{3+} ions which start to interact with each other and give rise to the formation of the Ti^{3+} pair. In addition to this, the authors assigned the occupied state at ~ -0.7 V to the D state, which starts to appear when the density of the Ti^{3+} pairs increases, and small areas of Ti_2O_3

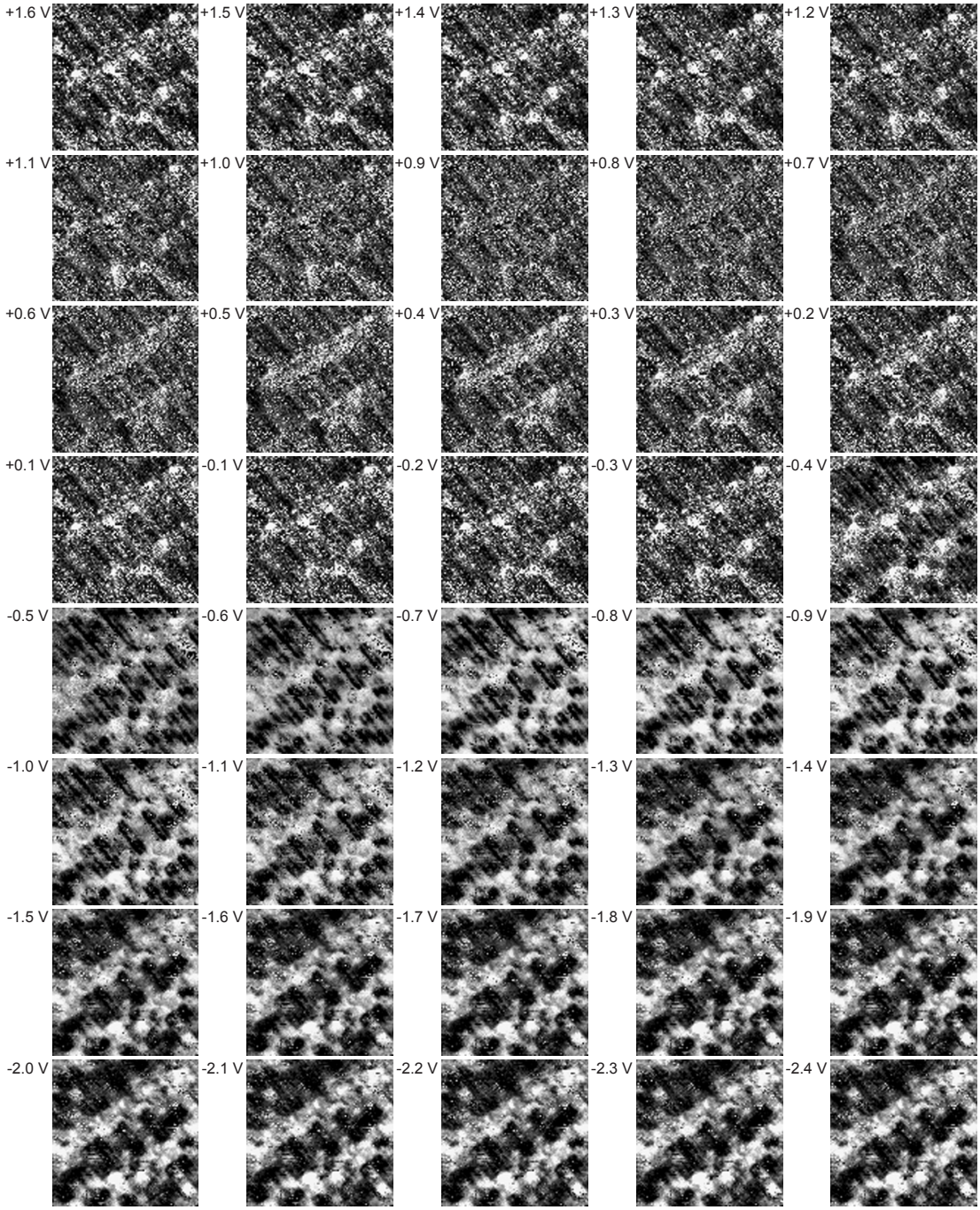

Figure 6.11: Current maps at sample bias ranging from +1.6 to -2.4 V, recorded simultaneously with the topographical image displayed in 6.12(a). The set point of the CITS measurement was at 0.9 V and 0.15 nA, at which the topographical image was taken. The absolute value of the current is plotted in grayscale with higher current corresponding to brighter areas.

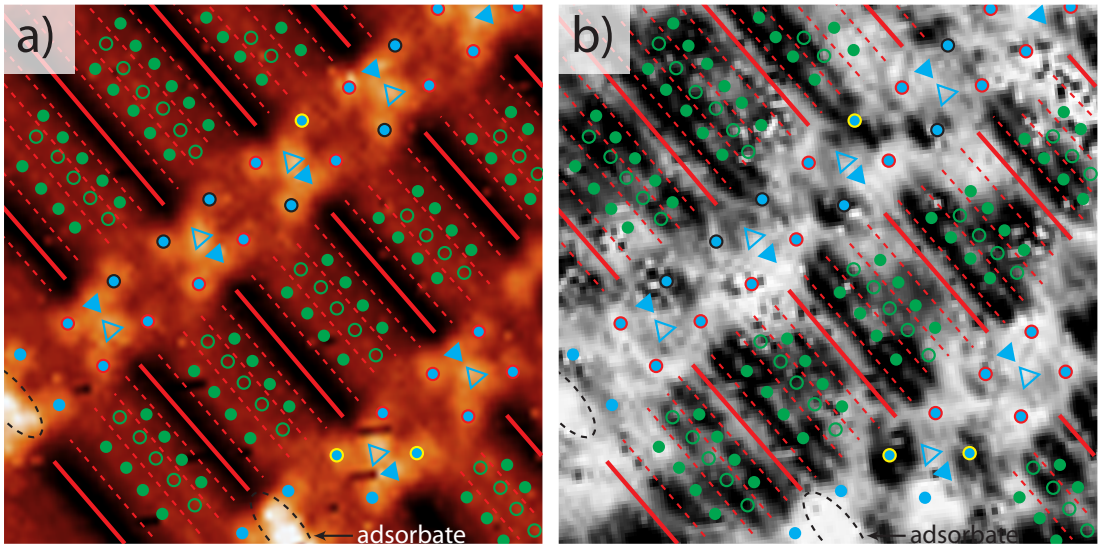

Figure 6.12: (a) A topographical picture recorded simultaneously with the current maps displayed in Figure 6.11 in CITS. In the figure, the bright spots on the central and side rows on the (1×2) strands are marked by green hollow and filled circles respectively. As for the cross-links, the bright and less bright features located at the centres are marked by blue hollow and filled triangles, and their corners marked by filled blue circles (some of them are marked by blue circles with peripheries of different colours, and these will be used in the part of CITS analysis). The dark region between the (1×2) strands and the region near the atomic rows of the strands are marked by red solid and dashed lines respectively. The cross-link which is covered with an adsorbate is indicated by a black circle. (b) The current image taken at -0.7 V, on top of which is overlaid with the feature-markers used in (a).

on the surface are formed. Going back to the $\bar{\sigma}(V)$ curves, it is found that the curves of the atomic rows at the centre and side of the (1×2) strands are quite close to each other in a way that the densities of the occupied states in both curves are almost the same. While having a similar D state, the $\bar{\sigma}(V)$ curve of the dark region between the strands shows a more-populated d state. On the other hand, the $\bar{\sigma}(V)$ curve of the region nearby the atomic rows of the strands exhibits a denser D state but a less dense d state. This contrast can also be observed in the current map at -0.7 V, in which the region nearby the atomic rows of the strands appear much darker, indicating a larger tunnelling current at those sites. Also note that the positions of the occupied states vary slightly (± 0.1 V) in response to their populations.

Secondly, the $\bar{\sigma}(V)$ curves of the bright and less-bright spots at the centre of the cross-links are compared. As shown in Figure 6.13(b), while both curves have an equally-populated d state, the curve of the bright spots exhibit a denser D state than that of the less bright

spots. In addition, both curves have an empty state at 1.1 V, which is not present in Figure 6.13(a). This state explains why the cross-links appear bright than the (1×2) strands in the empty-state topographical images.

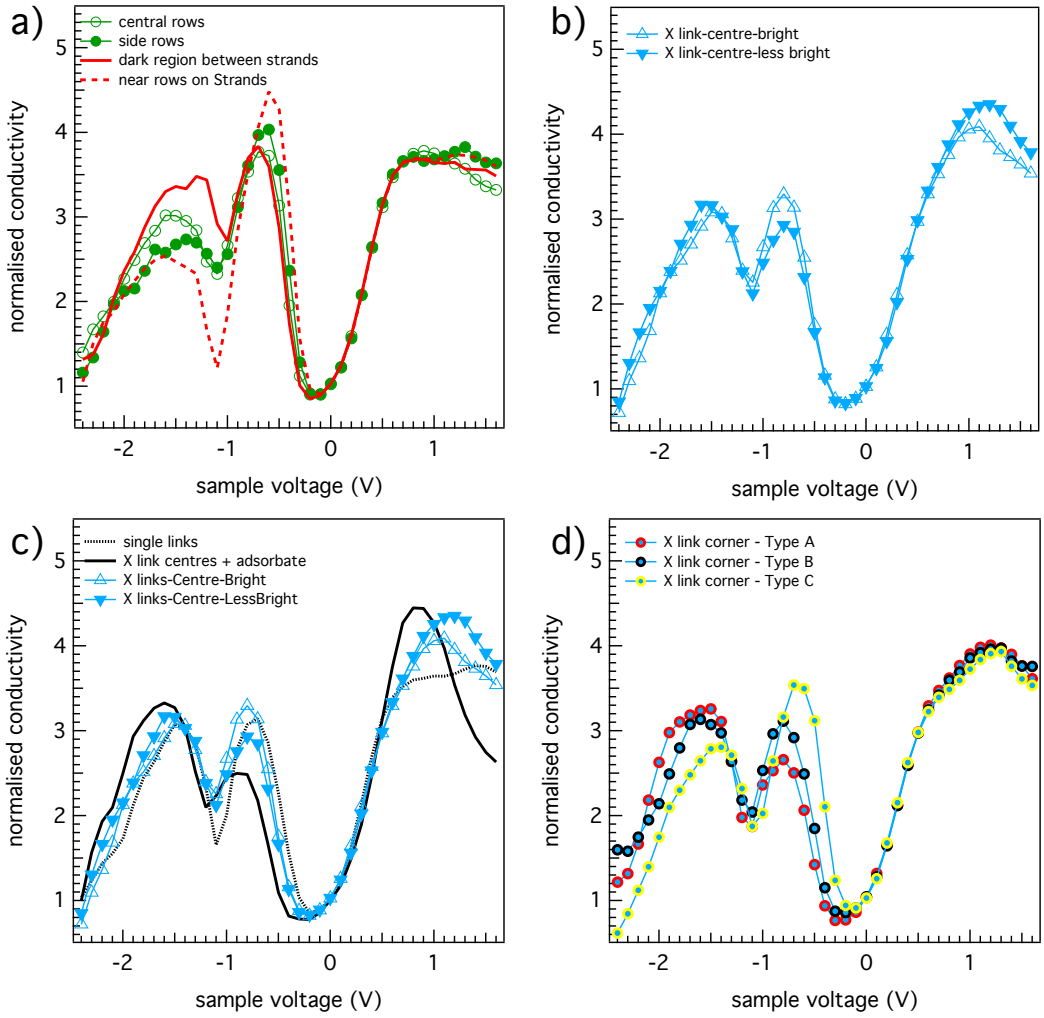

Figure 6.13: Comparison of normalised conductivity curves obtained from different features on the cross-linked TiO_2(110)-(1×2) surface. (a) Central and side bright rows on the (1×2) strands (green hollow and filled circles), dark region between strands (red solid line) and the region nearby the atomic rows on the strands (red dashed lines). (b) The bright (blue hollow triangles) and less-bright spots (blue solid triangles) at the centres of the cross-links. (c) Same as (b) together with the single-links (black dotted line) and the adsorbates on the cross-links (black solid line). (d) The corners of the cross-links, which can be grouped into three types according to their difference in normalised conductivity.

The $\bar{\sigma}(V)$ curves of the centre of the cross-links, the single links as well as the cross-links which is covered with adsorbates (probably molecular H_2O from the residual vacuum) are compared and displayed in Figure 6.13(c). The $\bar{\sigma}(V)$ curve of the single-links has the d and

D states which are equally populated. However, the empty state at 1.1 V, which is present in the $\bar{\sigma}(V)$ curve of the centre of the cross-links, is not present here. As for the cross-links which are covered by adsorbates, the corresponding $\bar{\sigma}(V)$ curve exhibits a denser d state and a less dense D state, as well as an empty state at 0.8 V. Compared to those in the $\bar{\sigma}(V)$ curve of the adsorbate-free cross-links, the positions of the D and d states here are shifted by 0.1 V away from E_{F}. This, and also the reduction in the density of the D state, could be explained by charge transfer from the cross-links to the molecule in the adsorption process.

As displayed in Figure 6.13(d), the $\bar{\sigma}(V)$ curves of various corners of the cross-links can be quite different from each other. Based on the relative densities of the d and D states, the corners of the cross-links can be divided into three groups: group A, which has the d state denser than the D state; group B, which has the d and D states equally populated; and group C, which has the d state less dense than the D state. The corners of the cross-links of different normalised conductivity are indicated in Figure 6.12, in which the same colour code as in Figure 6.12 is employed.

Several groups have studied the electronic structure reduced $TiO_2(110)$ at the atomic level. By performing STS on the mildly reduced $TiO_2(110)$ surface, Batzill *et al.* [26] investigated the LDOS at various features (such as the (1×1) terraces, step-edges, the single (1×2) strands and their terminations) on the (1×1) surface, and reported that the individual (1×2) strands have higher densities of occupied states than the (1×1) terrace. Using point-mode STS at 300 K, Murray *et al.* [8] looked into the local electronic structure of the cross-link reconstructed $TiO_2(110)(1\times2)$ surface, and found that the dark region between (1×2) strands has higher densities of occupied states than the (1×2) strands, which has higher densities of occupied states than the cross-links. Our results are compatible with those reported by Murray *et al.* [8]. In addition to this, we also discovered that the regions near the bright rows of the strands have a denser D state (at −0.7 V) but a less dense d state (at −1.5 V), as compared to the bright rows of the strands and the dark regions between the strands. As for the cross-links, apart from the small variation in the densities of the occupied states at both the D and d states, the normalised conductivity

curves at the centres and corners of the cross-links are qualitatively very close to each other. Moreover, the cross-links have an empty state at 1.1 V which cannot be observed anywhere else on the surface. This explains the brighter appearance of the cross-links than the (1×2) strands as well as the single links on the surface. As for the $\bar{\sigma}(V)$ curve of the adsorbate-covered cross-links, it has a smaller D state and an empty state at 0.8 V. The reduction in the size of the D state could be explained by charge transfer from the cross-link to the adsorbate. The state at 0.8 V probably corresponds to the $\pi^\star$ state of the adsorbate.

6.4 Conclusion and Future Work

The adsorption of O_2 onto the cross-link reconstructed TiO_2(110)-(1×2) surface at 300 K has been investigated with XPS, UPS and STM. Spectroscopic measurements show that the Ti^{3+} species on the topmost layer of the (1×2) surface as well as the defect states located at ∼1 eV below E_F are mostly quenched following smaller exposures of O_2 (0.5 L). The adsorption behaviour of O_2 on the (1×2) surface has also been monitored with STM, in which it was observed that O_2 and its related products preferably adsorb at the centre of the (1×2) strands, and the strands on the surface are completely covered with those O_2 related molecules following 0.1 L of O_2 exposure.

In addition, CITS was carried out on the cross-link reconstructed TiO_2(110)-(1×2) surface at 78 K. Compatible with the work by Murray *et al.* [8], we found that the population of the occupied states (at -0.7 and -1.3 V) at the dark regions between the (1×2) strands is higher than that at the bright rows of the strands, at which is higher than that at both the centres and corners of the cross-links. It was also discovered that the region near the bright rows of the strands (marked with red dotted lines in Figure 6.12) exhibit a denser D state (at −0.7 V) but a less dense d state (at −1.5 V), compared to the bright rows on the strands and the dark region between the strands. We also observed a change in the normalised conductivity of the cross-links induced by molecular adsorption. The above findings would help determine the geometrical structure of the cross-link (1×2) recon-

struction on the TiO_2(110) surface.

Employing CITS to investigate the local electronic structure of surfaces and interfaces is by no means trivial. It is believed that the material and shape of the tip, as well as the set-point, which controls the separation between the sample and the tip, would affect the results. For future work, CITS on the cross-linked TiO_2(110)-(1×2) surface will be carried out first at 78 K with tips of different materials (W or PtIr) and at various set-points to examine any of their effects, especially the tip-induced band-bending (TIBB) effect, which has been observed in several STM works on semi-conductor surfaces [41]. In addition to this, performing CITS at 5 K is known to provide more fruitful information on the local electronic structure in that the surface charges will be more localised around their origins. This has been illustrated by Papageorgiou *et al.* [42], who discovered that hopping of polarons around an O_b vac, which was observed at 78 K [43], does not take place at 5 K.

References

[1] U. Diebold, *Surf Sci Rep*, 2003, **48**, 53–229.

[2] C. L. Pang, R. Lindsay and G. Thornton, *Chem Soc Rev*, 2008, **37**, 2328–2353.

[3] M. A. Henderson, *Langmuir*, 1996, **12**, 5093–5098.

[4] M. A. Henderson, *Surf Sci*, 1999, **419**, 174–187.

[5] H. Onishi and Y. Iwasawa, *Surf Sci*, 1994, **313**, L783–L789.

[6] M. Li, W. Hebenstreit and U. Diebold, *Phys Rev B*, 2000, **61**, 4926–4933.

[7] R. A. Bennett, P. Stone, N. Price and M. Bowker, *Phys Rev Lett*, 1999, **82**, 3831–3834.

[8] P. Murray, N. Condon and G. Thornton, *Phys Rev B*, 1995, **51**, 10989–10997.

[9] M. Blanco-Rey, J. Abad, C. Rogero, J. Mendez, M. Lopez, J. A. Martin-Gago and P. L. de Andres, *Phys Rev Lett*, 2006, **96**, 055502.

[10] K. Ng and D. Vanderbilt, *Phys Rev B*, 1997, **56**, 10544–10548.

[11] U. Diebold, J. Anderson, K. Ng and D. Vanderbilt, *Phys Rev Lett*, 1996, **77**, 1322–1325.

[12] C. L. Pang, S. Haycock, H. Raza, P. Murray, G. Thornton, O. Gulseren, R. James and D. Bullett, *Phys Rev B*, 1998, **58**, 1586–1589.

[13] H. H. Pieper, K. Venkataramani, S. Torbruegge, S. Bahr, J. V. Lauritsen, F. Besenbacher, A. Kuehnle and M. Reichling, *Phys Chem Chem Phys*, 2010, **12**, 12436–12441.

[14] Z. Klusek, S. Pierzgalski and S. Datta, *Appl Surf Sci*, 2004, **221**, 120–128.

[15] A. Berko and F. Solymosi, *Surface Science*, 1998, **411**, L900–L903.

[16] J. Abad, C. Rogero, J. Mendez, M. F. Lopez, J. A. Martin-Gago and E. Roman, *Surf Sci*, 2006, **600**, 2696–2704.

[17] A. Berko, G. Menesi and F. Solymosi, *Surf Sci*, 1997, **372**, 202–210.

[18] K. Luo, T. S. Clair, X. Lai and D. Goodman, *J Phys Chem B*, 2000, **104**, 3050–3057.

[19] Y. Maeda, T. Fujitani, S. Tsubota and M. Haruta, *Surf Sci*, 2004, **562**, 1–6.

[20] K. T. Park, M. Pan, V. Meunier and E. W. Plummer, *Phys Rev B*, 2007, **75**, 245415.

[21] Q. Guo, I. Cocks and E. M. Williams, *Surface Science*, 1997, **393**, 1–11.

[22] I. D. Cocks, Q. Guo, R. Patel, E. M. Williams, E. Roman and J. deSegovia, *Surface Science*, 1997, **377**, 135–139.

[23] R. Bennett, P. Stone, R. Smith and M. Bowker, *Surface Science*, 2000, **454**, 390–395.

[24] K.-I. Fukui and M. Sakai, *J Phys Chem B*, 2006, **110**, 21118–21123.

[25] T. Okazawa, M. Fujiwara, T. Nishimura, T. Akita, M. Kohyama and Y. Kido, *Surf Sci*, 2006, **600**, 1331–1338.

[26] M. Batzill, K. Katsiev, D. Gaspar and U. Diebold, *Phys Rev B*, 2002, **66**, 235401.

[27] S. Wendt, R. Schaub, J. Matthiesen, E. K. Vestergaard, E. Wahlstrom, M. D. Rasmussen, P. Thostrup, L. M. Molina, E. Laegsgaard, I. Stensgaard, B. Hammer and F. Besenbacher, *Surf Sci*, 2005, **598**, 226–245.

[28] Z. Zhang, O. Bondarchuk, B. D. Kay, J. M. White and Z. Dohnalek, *J Phys Chem B*, 2006, **110**, 21840–21845.

[29] G. Teobaldi, W. A. Hofer, O. Bikondoa, C. L. Pang, G. Cabailh and G. Thornton, *Chem Phys Lett*, 2007, **437**, 73–78.

[30] M. Nolan, J. S. Mulley and R. A. Bennett, *Phys Chem Chem Phys*, 2009, **11**, 2156–2160.

[31] Q. Guo, S. Lee and D. W. Goodman, *Surface Science*, 1999, **437**, 38–48.

[32] O. Bikondoa, C. L. Pang, R. Ithnin, C. A. Muryn, H. Onishi and G. Thornton, *Nat Mater*, 2006, **5**, 189–192.

[33] C. M. Yim, C. L. Pang and G. Thornton, *Phys Rev Lett*, 2010, **104**, 036806.

[34] R. L. Kurtz, R. Stockbauer, T. E. Madey, E. Roman and J. L. deSegovia, *Surf Sci*, 1989, **218**, 178–200.

[35] S. Wendt, P. T. Sprunger, E. Lira, G. K. H. Madsen, Z. Li, J. O. Hansen, J. Matthiesen, A. Blekinge-Rasmussen, E. Laegsgaard, B. Hammer and F. Besenbacher, *Science*, 2008, **320**, 1755–1759.

[36] R. Patel, Q. Guo, I. Cocks, E. Williams, E. Roman and J. deSegovia, *J Vac Sci Technol A*, 1997, **15**, 2553–2556.

[37] Y. Du, N. A. Deskins, Z. Zhang, Z. Dohnalek, M. Dupuis and I. Lyubinetsky, *J Phys Chem C*, 2009, **113**, 666–671.

[38] *Scanning Tunneling Microscopy and Spectroscopy: Thoery, Techniques, and Applications*, ed. D. A. Bonnell, VCH Publishers, Inc., New York, 1993.

[39] R. M. Feenstra, J. A. Stroscio and A. P. Fein, *Surface Science*, 1987, **181**, 295–306.

[40] Z. Klusek, S. Pierzgalski and S. Datta, *Appl Surf Sci*, 2004, **221**, 120–128.

[41] M. Mcellistrem, G. Haase, D. Chen and R. Hamers, *Phys Rev Lett*, 1993, **70**, 2471–2474.

[42] A. C. Papageorgiou, N. S. Beglitis, C. L. Pang, G. Teobaldi, G. Cabailh, Q. Chen, A. J. Fisher, W. A. Hofer and G. Thornton, *P Natl Acad Sci Usa*, 2010, **107**, 2391–2396.

[43] T. Minato, Y. Sainoo, Y. Kim, H. S. Kato, K.-I. Aika, M. Kawai, J. Zhao, H. Petek, T. Huang, W. He, B. Wang, Z. Wang, Y. Zhao, J. Yang and J. G. Hou, *J Chem Phys*, 2009, **130**, 124502.

Chapter 7

Summary and Future Work

This thesis has described surface science studies of rutile TiO_2(110) employing scanning tunnelling microscopy and spectroscopic techniques.

Firstly, we have used STM in combination with UPS to determine the origin of the band-gap state in TiO_2(110). By using electron bombardment to vary the O_b vac density whilst monitoring the band-gap state in UPS, we have demonstrated that O_b vacs have a *major* contribution to the band-gap state peak and that its magnitude is directly proportional to the O_b vac density.

CO adsorption on the Pd/TiO_2(110) surface has been studied. The Pd islands, which were grown by physical vapour deposition (PVD) on the TiO_2(110)-(1×1) surface held at ∼800 K, were found to have a pseudo-hexagonal shape, and were not encapsulated with the Ti^{n+} (n<4). Those Pd islands were measured to have an average diameter of 30 nm and height of 5 nm, though their number density of the surface and size also depend on the Pd deposition rate. Following CO exposure of 2000 L, it was found that CO molecules bond vertically and form ordered overlayers on the Pd(111) islands at 78 K. These include two different c(4×2)-2CO ordered phases, in one of which all CO molecules occupy bridge sites, while in another CO molecules occupy both atop and bridge sites. The findings here suggest that the Pd islands have similar physical properties to the Pd(111) single crystals.

O_2 adsorption on the cross-linked TiO_2(110)-(1×2) surface was studied with UPS, XPS and STM. Introduction of a small amount of O_2 results in a drastic decrease in the amount of Ti^{3+} species at the topmost surface layer and the population of the band-gap state peak, as well as a noticeable increase in the surface workfunction. In STM, it was found that O_2 and its related molecules preferably adsorb at the centre of the (1×2) strands. At an O_2 exposure of 0.1 L, all the strands on the surface are completely covered with O_2 and its related features.

Current imaging tunnelling spectroscopy (CITS) was also carried out on the cross-linked TiO_2(110)-(1×2) surface in order to determine its geometrical structure by comparison with the calculations in the Shluger group. The experiment was first performed at 78 K. It was found that the densities of the two occupied states, one at -0.7 V and another at -1.3 V, vary between different features on the surface. The features include the atomic rows on the (1×2) strands, the region near the rows on the strands, the dark region between the strands, and the cross-links. Although there are less-populated occupied states, the cross-links exhibit an empty state at 1.2 V which cannot be observed anywhere else on the surface. Moreover, the occupation of the cross-links by adsorbates (probably H_2O) leads to a reduction in the density of the occupied state at -0.7 V, and the emergence of an empty state at 1.0 V.

Future Work

Instead of saturating the Pd/TiO_2 surface with CO at 300 K, it would be interesting to expose the surface to CO at low temperatures in the hope that dynamic change in ordering of CO with increasing coverages can be observed on top of the Pd(111) islands. Another potential experiment is to adsorb O_2 on the Pd(111) islands and investigate how CO reacts with the oxygen atoms/molecules at elevated temperatures, which will be very useful for understanding the CO oxidation that takes place on Pd-containing catalysts.

CITS measurements were carried out successfully on the TiO_2(110)-(1×2) surface at 78 K. However, prior to comparing our results with the calculations, several things still need to be examined. First of all, to examine any tip-effect, several tips, including PtIr tips, will be used to perform the same experiment at 78 K. In addition, different set-points will also used in the CITS measurement to check the tip-induced band-bending (TIBB) effect, which is commonly observed in STM experiments on semi-conducting surfaces. Moreover, again with different tips and set-points, CITS will also be carried out at 5 K, at which the surface charges are spatially more localised around their origins. By doing this more useful information about the local electronic structure of the cross-linked TiO_2(110)-(1×2) surface can be obtained.